JCTC Journal of Chemical Theory and Computation

pubs.acs.org/JCTC

Perspective

TURBOMOLE: Today and Tomorrow

Yannick J. Franzke,[‡] Christof Holzer,[‡] Josefine H. Andersen, Tomislav Begušić, Florian Bruder, Sonia Coriani, Fabio Della Sala, Eduardo Fabiano, Daniil A. Fedotov, Susanne Fürst, Sebastian Gillhuber, Robin Grotjahn, Martin Kaupp, Max Kehry, Marjan Krstić, Fabian Mack, Sourav Majumdar, Brian D. Nguyen, Shane M. Parker, Fabian Pauly, Ansgar Pausch, Eva Perlt, Gabriel S. Phun, Ahmadreza Rajabi, Dmitrij Rappoport, Bibek Samal, Tim Schrader, Manas Sharma, Enrico Tapavicza, Robert S. Treß, Vamsee Voora, Artur Wodyński, Jason M. Yu, Benedikt Zerulla, Filipp Furche,* Christof Hättig,* Marek Sierka,* David P. Tew,* and Florian Weigend*

Cite This: *J. Chem. Theory Comput.* 2023, 19, 6859−6890

ABSTRACT: TURBOMOLE is a highly optimized software suite for large-scale quantum-chemical and materials science simulations of molecules, clusters, extended systems, and periodic solids. TURBOMOLE uses Gaussian basis sets and has been designed with robust and fast quantum-chemical applications in mind, ranging from homogeneous and heterogeneous catalysis to inorganic and organic chemistry and various types of spectroscopy, light−matter interactions, and biochemistry. This Perspective briefly surveys TURBOMOLE's functionality and highlights recent developments that have taken place between 2020 and 2023, comprising new electronic structure methods for molecules and solids, previously unavailable molecular properties, embedding, and molecular dynamics approaches. Select features under development are reviewed to illustrate the continuous growth of the program suite, including nuclear electronic orbital methods, Hartree−Fock-based adiabatic connection models, simplified time-dependent density functional theory, relativistic effects and magnetic properties, and multiscale modeling of optical properties.

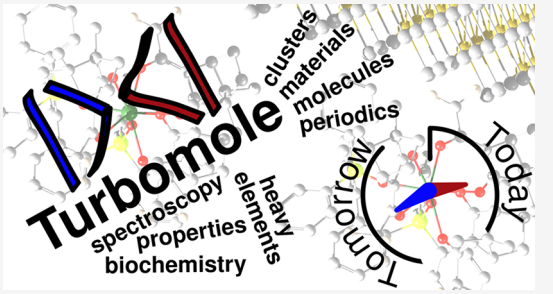

1. INTRODUCTION

TURBOMOLE is a collaborative, multinational software development project aiming to provide highly efficient and stable computational tools for quantum-chemical simulations of molecules, clusters, periodic systems, and solutions. The software suite is optimized for widely available, inexpensive, and resource-efficient hardware, such as multicore workstations and medium-size compute clusters. TURBOMOLE specializes in electronic structure methods with an outstanding accuracy−cost ratio, such as density functional theory including the random phase approximation (RPA), *GW*-Bethe−Salpeter equation (BSE) methods, second-order Møller−Plesset (MP2) theory, and coupled-cluster (CC) methods. The code is based on Gaussian basis sets and has been pivotal for the development of many fast and low-scaling algorithms in the past three decades, such as integral-direct methods, the resolution-of-the-identity (RI) approximation, fast multipole methods, imaginary frequency integration, Laplace transform, and pair natural orbital methods.

The development of TURBOMOLE was started in the late 1980s by Reinhart Ahlrichs and his group. Integral-direct algorithms and non-Abelian point group symmetry were among the first distinctive capabilities of TURBOMOLE, which initially focused on Hartree−Fock (HF) methods, with subsequent extensions for second-order MP2 perturbation theory[1−7] and time-dependent HF (TDHF) response properties.[8] A major milestone was the relatively early adoption of density functional theory (DFT) using newly designed quadrature algorithms[9] and that of time-dependent DFT (TDDFT) shortly afterward.[10] With extensions to meta-GGA,[11] RPA, and other fifth-rung methods,[12−16] as well as current density[17] and local hybrid functionals,[18,19] critical performance improvements,[20−24] and a plethora of available analytical derivatives of ground- and excited-state energies,[25−39] TURBOMOLE has become one of the leading all-purpose molecular (TD)DFT codes. The development and implementation of the RI approximation for Coulomb (RI-J[40,41]) and exchange contributions, (RI-K[42,43]), as well as its

Special Issue: Electronic Structure Theory Packages of Today and Tomorrow

Received: March 27, 2023
Published: June 29, 2023

Table 1. Available Parallelizations of Various Modules Shown in Version 7.7[a]

module	functionality	Fork-SMP	OpenMP	MPI	OpenMP/MPI	GPU
dscf	HF/DFT energy	√	√	√	√	√
grad	HF/DFT gradient	√	√	√	√	√
ridft	RI-HF/RI-DFT energy	√	√	√	X	√
rdgrad	RI-HF/RI-DFT gradient	√	√	√	X	√
aoforce	HF/DFT Hessian	√	√	√	√	√
escf	HF/DFT/*GW*-BSE excitation energies	√	√	√	√	√
egrad	HF/DFT excited-state gradient	√	√	X	X	√
mpshift	NMR/EPR parameters (HF/DFT/MP2)	X	√	X	X	√
evib	electron transport (HF/DFT)	√	√	√	√	X
odft	orbital-dependent DFT energies	X	√	X	X	X
mpgrad	MP2 energy, gradient	√	X	√	X	X
ricc2	RI-MP2, ADC(2), CC2 energies, gradients, spectra	X	√	√	√	X
pnoccsd	PNO-MPPT and PNO−CC energies with F12	X	√	√	√	X
ccsdf12	CCSD, CCSD(T) energies with F12	X	√	X	X	X
rirpa	RPA energy, gradient	X	√	X	X	X
riper	periodic HF/DFT energy, gradient	X	√	X	X	X

[a]Fork-SMP[94] and the OpenMP version[46,62,95−97] are restricted to calculations on a single node. MPI[5,98−101] and OpenMP/MPI hybrid[102] implementations allow for the use of multiple nodes. The availability of first- and second-order derivatives as well as excitation energies is also indicated.

generalization to post-HF theories such as MP2 and CC2[44−46] and its multipole-accelerated version for extended systems (MARI-*J*), were other critical innovations.[47] The RI methods are still cornerstones in many modern implementations and outstanding features of the program suite.[23,31,48−68] More recent additions include explicitly correlated wave function methods up to CCSD(T) and BCCD(T),[68,69] efficient pair natural orbital (PNO) approaches,[70−73] solvation models and embedding,[74−83] two-component relativistic methods,[84−86] GW-BSE type methods[52,87,88] real-time (RT) TDDFT,[89] and nonadiabatic molecular dynamics.[90]

To ensure continuity and coordinate the development, maintenance, and distribution independent of individual developers or groups, TURBOMOLE GmbH, a limited liability company located in Karlsruhe, Germany, was founded in 2007. TURBOMOLE GmbH has adopted an irrevocable bylaw preventing the distribution of dividends to ensure that all profits are reinvested into the project. TURBOMOLE GmbH distributes fee-based end-user licenses itself and through partners, as well as free developer licenses and access to the source code based on project proposals.[91]

Here we focus on recent developments and provide illustrative applications to chemistry and materials science. For an overview of existing features, as well as development, licensing, and distribution, the reader is referred to refs 92 and 93 and the TURBOMOLE Web site.[91]

2. BRIEF FEATURE OVERVIEW

The program suite consists of a series of modules with a broad range of methods from universal force field to fast semi-empirical methods, state-of-the-art DFT and MP2, and coupled-cluster and post-HF methods for ground and excited states. For convenience, the use of modules is facilitated by various tools such as the scripts `woelfling`, `raman`, `vcd`, and `genetic.py` for reaction path optimization,[103] vibrational Raman spectra,[29] vibrational circular dichroism spectra (VCD),[104] and genetic algorithms, respectively.[105] Moreover, the graphical user interface TmoleX is of great help for running calculations and visualizing results.[106]

Almost all time-consuming parts are parallelized for multicore systems or clusters using OpenMP[107] for shared-memory parallelization (SMP)[46,62,95−97] and the message-passing interface[108] (MPI) for parallelization across multiple nodes,[98−102] as outlined in Table 1. The older Fork-SMP[94] is available as a fallback for some modules. Starting with the latest release (V7.7), support for graphics processing units (GPUs) has become available.[109]

The list of parallelized HF/DFT modules includes those for molecular self-consistent field (SCF) energy (`dscf` and `ridft`) and gradient calculations (`grad` and `rdgrad`), response properties such as vibrational frequencies (`aoforce`), NMR/EPR spectra (`mpshift`), excited-state properties (`escf`, `egrad`), and electron transport properties (`evib`). For these modules, the OpenMP version is recommended for most calculations due to its cost−benefit ratio in terms of computer hardware. Accordingly, post-Kohn−Sham methods (`rirpa`) and calculations with periodic boundary conditions at the HF/DFT level (`riper`), as well as the CCSD and CCSD(T) program `ccsdf12`, are only parallelized with OpenMP. In contrast, the implementation of approximate CC methods in `ricc2` and `pnoccsd` widely supports the OpenMP and MPI standard and combinations thereof for large-scale calculations on multiple nodes.

3. RECENT DEVELOPMENTS

3.1. Local Hybrid Functionals for Strong Correlation and Range-Separated Local Hybrid Functionals. Local hybrid functionals (LHs)[110,111] with a position-dependent exact-exchange (EXX) admixture governed by a local mixing function (LMF) have been part of TURBOMOLE since release V7.2 and have since been extended in various ways over the past years. Using seminumerical integration techniques, such LHs have been implemented in an efficient way in the code,[18] with functionalities that exceed by far those available in any other quantum-chemistry package that contains LHs. Beyond ground-state SCF[112] and nuclear gradients,[33] this now includes linear-response TDDFT energies[19,113] and excited-state gradients,[35] frequency-dependent and frequency-independent polarizabilities,[113,114] NMR chemical shifts[115] and

https://doi.org/10.1021/acs.jctc.3c00347
J. Chem. Theory Comput. 2023, 19, 6859−6890

spin−spin coupling constants,[60,86] EPR hyperfine couplings and g-tensors,[116,117] the related NMR shieldings of paramagnetic systems,[118] magnetizabilities,[119] and quasiparticle states based on *GW*.[119] From the variety of possible applications and evaluations, many of which have been touched upon in the 2020 overview of TURBOMOLE[92] and in a 2019 comprehensive review of local hybrids,[110] we highlight in particular the outstanding performance of LHs for mixed-valence systems[120−122] and for phosphorescence spectra.[123−125] We also point to further recent LH publications and to reviews by other authors.[111,117,119,126−128]

Here, we focus on two recent extensions. Essentially, the aims of these works have been to conserve the established advantages of LHs and improve other aspects. We start with the fundamental goal to escape the often invoked "zero-sum game"[129,130] between reduced self-interaction errors and delocalization errors or "fractional-charge errors" (FCEs) on one side and minimizing static-correlation errors or "fractional-spin errors" (FSEs) on the other side.[131] The enhanced EXX admixture usually helps minimize FCEs, and LHs have been shown to achieve this goal while retaining some of the important left−right correlation in bonding regions.[110] On the other hand, larger EXX admixtures usually are detrimental in cases with large FSEs, such as dissociating or stretched bonds or many transition-metal systems with appreciable static correlation. Standard LHs so far have not been a way out of this dilemma, at least not to a larger extent. Relevant real-space approaches to reduced FSEs are Becke's B13 functional[132] and a modified approach by Kong and Proynov (KP16/B13),[133] which have both been implemented self-consistently into a local developer's version of TURBOMOLE.[134]

Circumventing the numerical difficulties and poor SCF convergence in many cases of the B13 and KP16/B13 functionals, the idea of a local strong-correlation factor has recently been transferred to the LH framework. Initial attempts were still based on relatively simple first-generation LHs but did already show that FSEs can be reduced when multiplying the LH term for nondynamical correlation (NDC) by a somewhat modified KP16/B13-type q_{AC} factor.[134] Most recently, the more advanced scLH22t functional has been constructed.[135] It is based on the more recent and overall more accurate LH20t functional.[120] Using a damping factor for smaller NDC contributions, an almost complete decoupling between the underlying LH20t and the added q_{AC} factor could be obtained. That is, the optimized parameters of LH20t, as well as its excellent performance for weakly correlated situations (e.g., for GMTKN55 main-group energetics), are retained, but FSEs and the related spin-restricted dissociation curves of covalent bonds are dramatically improved.[135] Notably, the q_{AC} factor forms part of a new LMF (Figure 1).

The second extension of LHs has been the implementation and construction of range-separated local hybrids (RSLHs), combining the ideas of local hybridization in real space and range-separated hybrids in interelectronic distance space.[136,137] That is, instead of full-range semilocal exchange, short-range exchange is mixed in. This corresponds to the use of a long-range EXX admixture governed by a suitable range-separation parameter ω. Based on earlier work for locally range-separated hybrids,[138] RSLHs have been implemented for ground-state SCF (modules `dscf/ridft`) and gradients (modules `grad/rdgrad`), as well as for linear-response TDDFT (module `escf`).[139] Using this implementation, the ωLH22t RSLH has been constructed and optimized. It retains most of

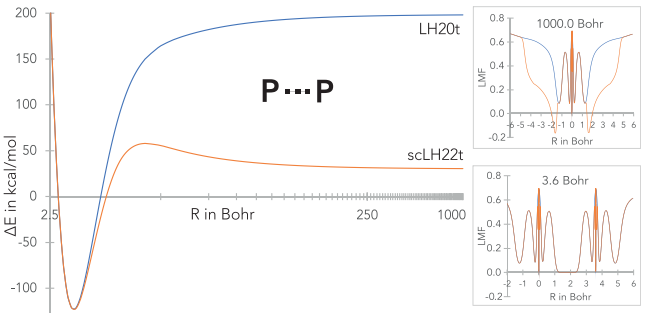

Figure 1. Spin-restricted dissociation curve of P_2 with the original (LH20t) and sc-corrected t-LMF (scLH22t) along the bond axis for different distances on the dissociation curve (right). See ref 135 for related graphics for other molecules.

the good performance of LH20t for main-group and transition-metal energetics, as well as for core, Rydberg, and triplet valence excitations. At the same time, however, it decisively corrects errors for excitations with appreciable charge-transfer character and improves on the potential-energy curves of three-electron cations known to be affected strongly by self-interaction errors.[139] Most recently, ωLH22t has been demonstrated to provide unprecedented accuracy in quasiparticle energies for applications in molecular electronics and organic photovoltaics, without the usual system-dependent tuning of range-separated hybrids.[140]

3.2. Inclusion of the Current Density in DFT. The kinetic energy density $\tau(\mathbf{r})$ is a commonly used ingredient in many functionals to detect iso-orbital regions or describe the inhomogeneity of the electron density $\rho(\mathbf{r})$. For its extension $\tau(\mathbf{r},t)$, used in the time-dependent Kohn−Sham formalism (TDKS), it has been shown[17] that this quantity is not invariant under a gauge transformation in the external potential. Substitution of τ by its generalization[141−143] $\hat{\tau}(\mathbf{r}, t) = \tau(\mathbf{r}, t) - \frac{|\mathbf{j}_P(\mathbf{r}, t)|^2}{2\rho(\mathbf{r}, t)}$, where $\mathbf{j}_P$ is the paramagnetic current density, restores gauge invariance. This leads to additional terms in the magnetic orbital rotation Hessian in linear-response TDDFT calculations, accounting for the response of $\mathbf{j}_P$. While the original implementation of these terms in TURBOMOLE dates back to 2012 (release V6.4), we highlight four recent important updates.

First, an incorrect prefactor 2 has been removed from the original implementation with V7.6.[119,144] TDDFT calculations employing τ-dependent functionals performed with previous versions erroneously overcorrected for the effects of the current density response and should be reassessed, although average changes are on the order of 0.03 eV.[144]

Second, a recent investigation[145] reveals that the effect restoring gauge invariance has on the final excitation energies can be significantly larger than previously assumed depending on the functional and type of excitation. In one particular investigation of d−d excitations in nickel(II) complexes, restoring gauge invariance shifts the excitation energies with the M06-2X functional by more than 0.4 eV closer to the experimental reference values, as shown in Figure 2.[145]

A broader analysis reveals that the importance of imposing gauge invariance can be linked to the derivative of the exchange energy integrand with respect to τ.[145] Moreover, $n \rightarrow \pi^*$ excitations are significantly more affected by restoring gauge invariance than most $\pi \rightarrow \pi^*$ excitations with the exception of $\pi \rightarrow \pi^*_\parallel$ excitations, where the dominantly contributing

https://doi.org/10.1021/acs.jctc.3c00347
J. Chem. Theory Comput. 2023, 19, 6859−6890

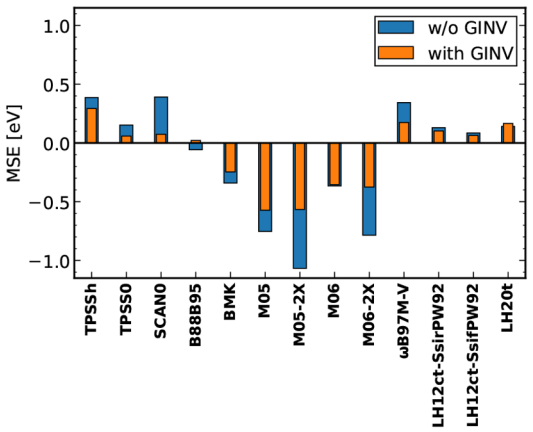

Figure 2. Effect of restoring gauge invariance (GINV) for various τ-dependent functionals on the average deviation of vertical TDDFT excitation energies from the experimental absorption maxima for five Ni(II) complexes.[146] Reprinted from ref 145 with permission. Copyright 2022 AIP Publishing.

molecular orbitals (MOs) are perpendicular ($\perp$) to each other.[145] These findings suggest that a reassessment of previously reported TDDFT results obtained with τ-dependent functionals is warranted, particularly for cases that are potentially more sensitive due to the choice of the functional, the type of excitation, or both. Gauge invariance is restored by default with τ-dependent functionals at moderate (nonhybrid functionals) or negligible (hybrid functionals) additional computational cost.[17] Recently, excited-state gradients and quadratic response properties for $\hat{\tau}$-dependent meta-generalized gradient approximations (mGGAs) have been implemented, enabling gauge invariant computations of excited-state equilibrium structures, relaxed dipole moments, (dynamic) hyperpolarizabilities, and two-photon absorption cross sections.[147] These developments will be available in a future TURBOMOLE release.

Third, the inclusion of $\mathbf{j}_P$ is required for gauge invariance of magnetic properties and implemented for magnetizabilities,[119] NMR coupling constants,[119] and NMR shifts of closed-shell[119,148] and open-shell systems,[118] as well as EPR hyperfine coupling constants[149] and g-tensors.[118] Recent findings indeed hint at the inclusion of the current density response also being crucial for NMR and EPR properties.[118,119,148] Especially for open-shell systems, neglecting the current density leads to large deviations,[118] as shown in Figure 3.

Finally, it was shown that the inclusion of the paramagnetic current is also crucial in relativistic two-component calculations.[151] Contrary to all previous cases, the modifications outlined above must already be taken into account for the ground state in the presence of spin−orbit coupling (SOC). SOC gives rise to an internal magnetic field, inducing a paramagnetic current that already has a nonvanishing contribution at the energy-level.[151] Accordingly, if properties such as light−matter interactions are targeted in the presence of SOC, the interplay of the ground- and excited-state paramagnetic currents must be taken into account. This gives rise to highly nonlinear $\mathbf{j}_P$-dependent terms, which have a profound impact on many properties.[151,152] Current density functional theory (CDFT) for τ-based functionals is available for ground-state energies (module `ridft`) and gradients (module `rdgrad`) and linear response properties (modules `escf` and `mpshift`).[151] Given the profound impact of $\mathbf{j}_P$, we therefore strongly recommend the exclusive use of the current-dependent forms.

3.3. Methods for Finite Magnetic Fields. Quantum-chemical calculations are routinely carried out for various types of molecular properties in magnetic fields, including NMR, EPR, and magnetic circular dichroism (MCD) spectroscopy (see also sections 3.4, 3.5, 3.6, and 3.9.2 of this Review).[153−155] For these applications, the magnetic field is usually treated perturbatively, as it is orders of magnitude smaller than the electronic interactions responsible for the formation of a chemical bond.

Other applications necessitate the use of a more general approach, particularly if the magnetic field becomes strong enough to compete with the electronic interactions within a molecule (>1000 T).[156−163] Such conditions may be found in the vicinity of interstellar objects like magnetic white dwarfs and cannot be reproduced in a laboratory.[164−167] Consequently, spectra obtained from such interstellar objects can only be interpreted using quantum-chemical calcula-

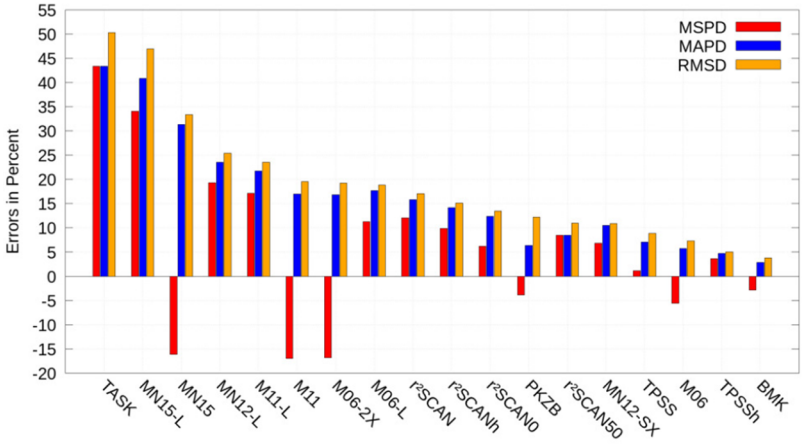

Figure 3. Impact of the current-dependent generalization of τ for various density functional approximations on the isotropic Δg-shift of $[MoNCl_4]^{2-}$, $[MoOF_4]^-$, $[MoOCl_4]^-$, $[MoOF_5]^{2-}$, $[MoOBr_5]^{2-}$, $[TcNF_4]^-$, $[TcNCl_4]^-$, and $[TcNBr_4]^-$. Results with the well-known field-dependent generalization serve as reference.[150] We list the mean signed percentwise deviation (MSPD), the mean absolute percentwise deviation (MAPD), and the root-mean-square deviation (RMSD). Reprinted from ref 118 under a CC BY license. Copyright 2022 the Authors.

https://doi.org/10.1021/acs.jctc.3c00347
J. Chem. Theory Comput. 2023, 19, 6859−6890

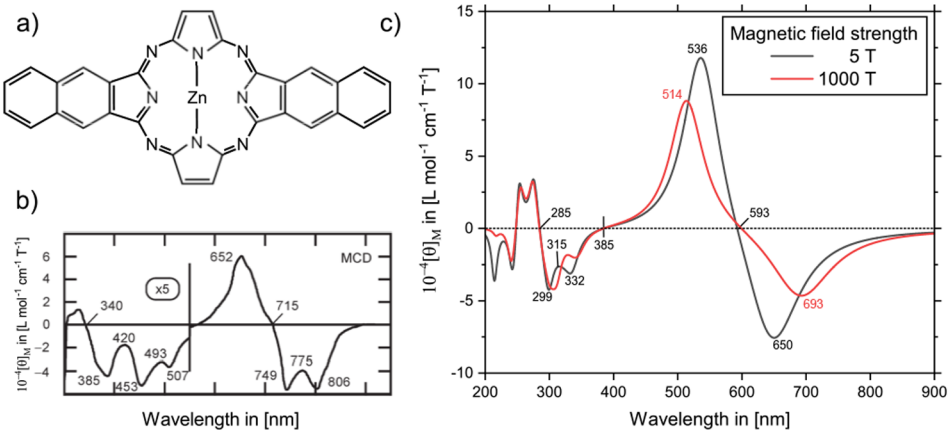

Figure 4. MCD spectrum of ZnDiNTAP. (a) Molecular structure. (b) Experimental spectrum. Reprinted with permission from ref 180. Copyright 2007 RSC Publishing. (c) Spectra as calculated in finite magnetic fields of 5 and 1000 T. Adapted with permission from ref 176. Copyright 2022 the Authors.

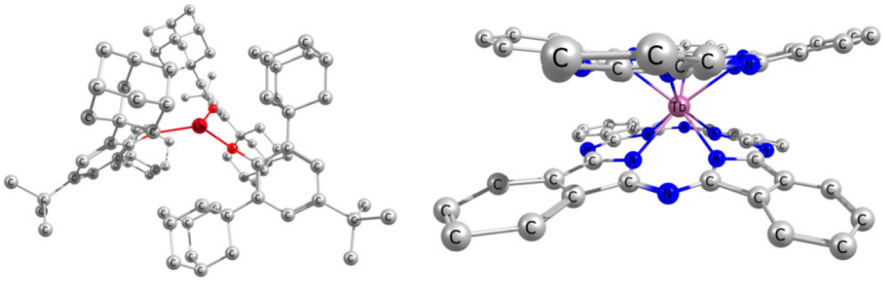

Figure 5. Molecular structure of single-molecule magnets $[Lu(OAr^*)_3]^-$ and $[TbPc_2]^-$. Reprinted with permission from ref 151 under a CC BY license. Copyright 2022 the Authors.

tions[168−172] In such extreme conditions, entirely new types of chemical bonding, spin-phase transitions, and other exotic phenomena have been shown to occur.[162,173,174] The effects of arbitrarily weak or strong magnetic fields on atoms or molecules may be computed using the finite magnetic field approach, which is implemented for Hartree−Fock,[175] CDFT,[152,176] *GW*/BSE,[177,178] RPA,[179] and CC2.[178] Through the calculation of electronic ground states, molecular gradients, and electronic excitations, a wide variety of applications for molecular spectroscopy in magnetic fields are now accessible.

Due to the efficiency of our implementation, systems containing dozens of atoms can be routinely computed in explicit magnetic fields.[152,175,176,178] To highlight the capabilities of our approach, we calculated the MCD spectrum of ZnDiNTAP,[176,180] a zinc tetraazaporphyrin with two fused naphthalene units, Figure 4a, using CAM-B3LYP and a mixed def2-TZVP (Zn)/def2-SVP (all other atoms) basis set. Similarly to the experiment,[180] Figure 4b, a magnetic field of 5 T was applied. The resulting spectrum is shown in Figure 4c. Minor differences can all be attributed to solvation effects and vibronic coupling, which were neglected in our calculation.[176] Furthermore, the MCD spectrum of ZnDiNTAP in an explicit magnetic field of 1000 T is shown in Figure 4c. While some of the bands, particularly in the fingerprint region, are not affected by nonlinear effects induced via such a strong field, the two Q bands are significantly shifted (650 → 693 nm and 536 → 514 nm).

Other applications of the finite magnetic field ansatz include higher-order properties such as magnetizabilites and hypermagnetizabilities through the use of numerical derivatives. Moreover, molecules that are naturally prone to exhibiting "magnetic" effects, such as aromatic compounds (see also section 3.7), may show a nonlinear response even to weak magnetic fields.[152] This is not captured by a perturbative approach but can be routinely investigated using our implementation.

3.4. EPR Properties and Single-Molecule Magnets.

Over the past decade, TURBOMOLE has pioneered the *in silico* study of f-element chemistry. To provide accurate descriptions of compounds containing these heavy elements, robust DFT routines are leveraged to deliver a balanced treatment of dynamic correlation, static correlation, solvation, and relativistic effects. More recently, these developments have enabled the discovery of new species with novel chemistry, subsequently necessitating new and improved computational methods capable of describing them.

For example, a series of recently discovered Ln-based single-molecule magnets (SMMs), $[La(OAr^*)_3]^-$, $[Lu(NR_2)_3]^-$, and $[Lu(OAr^*)_3]^-$ (OAr^* = 2,6-Ad_2-4-*t*-Bu-C_6H_2O, Ad = adamantyl, *t*-Bu= *tert*-butyl, R = $SiMe_3$ with Me = methyl), were found to exhibit exotic EPR properties, with $[Lu(OAr^*)_3]^-$ producing hyperfine coupling (HFC) constants of unforeseen magnitude and furthermore demonstrating extended magnetic coherence facilitated by a hyperfine clock transition. A primary investigation of these species with nonrelativistic HFC operators attributed the large hyperfine coupling constants to a sizable Fermi contact contribution from the highest occupied MO (HOMO) of each system. However, the predictions of hyperfine coupling constants and g-tensor values themselves produced errors of roughly one

https://doi.org/10.1021/acs.jctc.3c00347
J. Chem. Theory Comput. 2023, 19, 6859−6890

order of magnitude, strongly suggesting the need for more rigorous methods.[181]

Such improved predictions of EPR spectra are possible with relativistic exact two-component (X2C) theory,[38,39] including spin−orbit effects up to the noncollinear two-component (2c) DFT framework.[38,39,117] For meta-generalized gradient approximations and local hybrid functionals, this also includes the paramagnetic current density in the ground state (cf. section 3.2).[151] This rigorous formulation can be truncated to the scalar-relativistic limit[63] or a perturbative ansatz[149] to study the individual contributions of each term to the EPR parameters. Gauge origin invariance of the *g*-tensor calculations is ensured by the gauge including atomic orbitals,[36,39,149] which are crucial for systems with a spatially distributed spin density. These methods were implemented, and their performance is shown here for the aforementioned SMM $[Lu(OAr^*)_3]^-$ shown in Figure 5. The all-electron relativistic methods lead to good agreement with the experiment, as shown in Table 2. The HFC constant of

Table 2. Principal Components for the HFC *A* of $[Lu(OAr^*)_3]^-$ and Isotropic HFC *A* of $[TbPc_2]^-$ at Various Levels of theory[38,39,117,149] and Comparison with Experimental Results (expt.)[181,182a]

		$[Lu(OAr^*)_3]^-$			$[TbPc_2]^-$
method		A_{xx}	A_{yy}	A_{zz}	A
TPSS	SR	3192	3192	3148	190
cTPSS	SO	3190	3190	3153	375
ωB97X-D	SR	3489	3489	3456	136
ωB97X-D	SO	3464	3464	3448	488
TMHF	SR	3225	3225	3171	293
cTMHF	SO	3208	3208	3161	526
Expt.		3500	3500	3400	519

[a]HFC is given in MHz. SR and SO denote scalar and spin−orbit relativistic results (x2c-TZVPall-2c/x2c-SVPall-2c basis), respectively.

$[Lu(OAr^*)_3]^-$ is dominated by the scalar-relativistic contribution due to the localization of the spin-density in the 6s/d HOMO producing a large Fermi contact interaction. The importance of the paramagnetic spin−orbit contribution increases with the number of unpaired electrons and the scalar formulation, as well as the spin−orbit perturbation theory (SOPT) break down for systems such as $[TbPc_2]^-$ with six unpaired electrons, Pc = bis(phthalocyaninato).[38,39,117,151] The self-consistent 2c methods are thus pivotal.

With the next release version, the EPR Euler transformations for the HFC, *g*-tensor, and electric-field gradient as well as the nuclear quadrupole interaction tensor will further become available for users.[39]

3.5. NMR Coupling Constants Across the Periodic Table of Elements. NMR spectroscopy is key to the analysis and structure determination not only for organic compounds but also for inorganic systems consisting of heavy elements. The NMR spin−spin coupling constant describes the splitting of the signals or peaks in the NMR spectra and is a characteristic property driven by the chemical environment. Formally, the coupling tensor is obtained as the mixed derivative of the energy with respect to the corresponding nuclear magnetic moments, which are introduced via the principle of minimal coupling. NMR couplings are available within a nonrelativistic[60] scalar X2C[183] and the spin−orbit X2C framework.[86] All functional classes up to local hybrids are supported and include the current density for gauge invariance.[61,119,151]

For systems made up of light elements, the nonrelativistic treatment is sufficient. Here, the coupling constant is generally partitioned into the Fermi-contact (FC), spin−dipole (SD), paramagnetic spin−orbit (PSO), and diamagnetic spin−orbit (DSO) contributions. The FC, SD, and PSO terms necessitate the solution of the response equations, whereas the DSO term is computed with the ground-state density. Typically, the FC contribution is the leading term, and accurate coupling constants require large basis sets. Thus, a nuclear selection scheme and locally dense basis sets are often applied to large-scale calculations.

Systems containing heavy elements such as Sn, Pb, Pd, and Pt require the inclusion of relativistic effects,[61,86,183,185−187] *i.e.*, methods based on the Dirac equation are introduced. For such methods, the FC, SD, and PSO terms are coupled due to spin−orbit interaction, and they come with drastically increased computational demands. Nevertheless, when using a local X2C ansatz,[84−86] large-scale calculations are possible, as illustrated in Figure 6 for the Karplus relationship of $Me_3Sn-CH_2-CHR-SnMe_3$, where R is different substituents (Me = CH_3). The relativistic DFT approach reproduces the experimental findings with fairly good agreement. Improvements are possible with the correlation kernel augmented BSE (cBSE) based on the Green's function *GW* ansatz. Here, the DFT response equations are replaced with their BSE counter parts.[61,113]

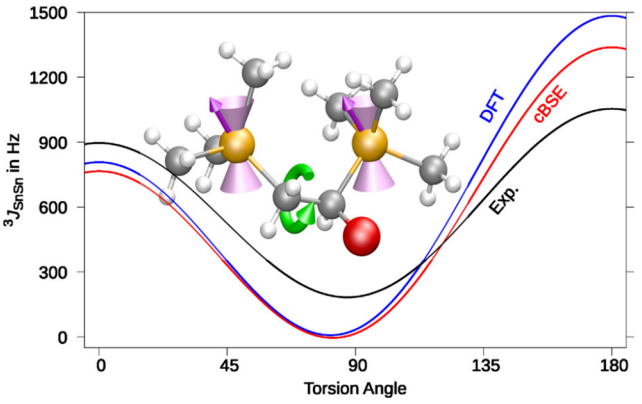

Figure 6. Fitted Karplus equation for Sn compounds: $^3J = A\cos(2\phi) + B\cos(\phi) + C$. For each Sn−Sn torsion angle ϕ, the average of the $^3J_{SnSn}$ coupling constant over 13 compounds is computed. Blue, BH&HLYP/x2c-TZVPall-2c; red, *GW*-cBSE@BH&HLYP; and Exp., experimental findings.[184] Adapted with permission from ref 61. Copyright 2022 the Authors.

To demonstrate the efficiency, the calculation of the Sn−P coupling constants of $[(\{SIDipp\}P)_2Sn]$ (SIDipp = 1,3-bis(2,6-di-isopropylphenyl)-imidazolidin-2-ylidene) with 137 atoms[187] takes about 44 min (PBE) and 55 h (PBE0) using 12 OpenMP threads of an Intel Xeon Gold 6212U CPU (2.40 GHz).[86] Notably, using a single NVIDIA A100 GPU, the PBE0 timing can be reduced to 3.5 h.

3.6. Paramagnetic NMR Shieldings and Shifts. NMR spectroscopy is also an important technique for the characterization of open-shell chemical compounds. NMR shielding tensors and chemical shifts describe the positions of the peaks in NMR spectra. In the closed-shell case, only the temperature-independent orbital contribution is relevant to the calculation

https://doi.org/10.1021/acs.jctc.3c00347
J. Chem. Theory Comput. 2023, 19, 6859−6890

of the shielding tensor. Both a nonrelativistic treatment[3,62,188] and a scalar-relativistic treatment[36,104] are available for the orbital contribution, including the response of the current density.[118,119,148] The paramagnetic NMR (pNMR) shielding tensor $\boldsymbol{\sigma}_I^{\mathrm{tot}}$ for a nucleus I reads

$$\boldsymbol{\sigma}_I^{\mathrm{tot}} = \boldsymbol{\sigma}_I^{\mathrm{orb}} - \frac{\mu_e S\cdot(S+1)}{3\gamma_I k_B T}\boldsymbol{A}_I \boldsymbol{g}^{\mathrm{T}} \quad (1)$$

with S denoting the spin, μ_e denoting the Bohr magneton, γ_I denoting the gyromagnetic ratio of nucleus I, k_B denoting the Boltzmann constant, and T denoting the temperature. Here, the orbital contribution $\boldsymbol{\sigma}^{\mathrm{orb}}$ is the straightforward open-shell generalization of the closed-shell limit.[63,118] Additionally, a temperature-dependent contribution arises, which includes the HFC tensor A_I of nucleus I and the g-tensor g already discussed in section 3.4. Both the HFC and the g-tensor depend on spin−orbit coupling. For the calculation of ^{1}H/^{13}C pNMR spectra of large molecules, a perturbative treatment of spin−orbit coupling is preferred over the 2c ansätze due to lower computational costs.[149] The viability of the pertubative ansatz in the X2C framework is demonstrated for two negatively charged Ru(III) complexes in Figure 7, which depicts the good agreement between calculated results and the experimentally measured[189] pNMR ^{1}H and ^{13}C shifts of the two compounds.

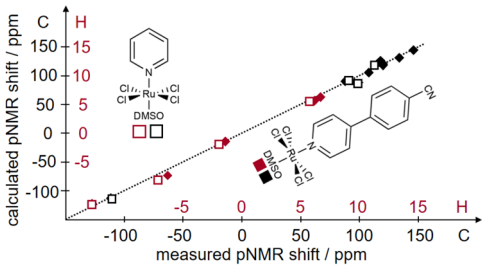

Figure 7. Computational results (ωB97X-D/x2c-TZVPall-s) and experimental findings for two negatively charged Ru(III) compounds. Adapted with permission from ref 149. Copyright 2022 the Authors.

The calculation of properties depending on the density in the vicinity of the nuclei requires additional tight basis functions. Thus, the pcJ,[190] pcS,[191] and pcH[192] basis sets are recommended for nonrelativistic calculations. For relativistic calculations, the x2c-s basis sets were developed.[193,194]

The efficiency of the pNMR implementation is similar to that of the closed-shell case, as shown in Figure 8. Coulomb integrals can be calculated with the RI-J/MARI-J approximations for the Coulomb contribution[62,63] and the semi-numerical scheme for exchange integrals.[18,109]

3.7. Ring Currents of Heavy-Metal Clusters. Aromatic compounds, such as benzene, show characteristic signals at 7 ppm in the ^{1}H NMR spectra. This shift is a consequence of the cyclic electron delocalization associated with the π-orbitals, which deshield the nuclei due to an induced ring current.[195] This magnetically induced current density may be calculated indirectly with the nucleus-independent chemical shift[196] (NICS) or directly using TURBOMOLE's interface to the GIMIC program, which was reworked for release V7.7 and now supports open-shell calculations.[197−200] The latter approach is more flexible and also applicable to complicated multicyclic systems.[201−204]

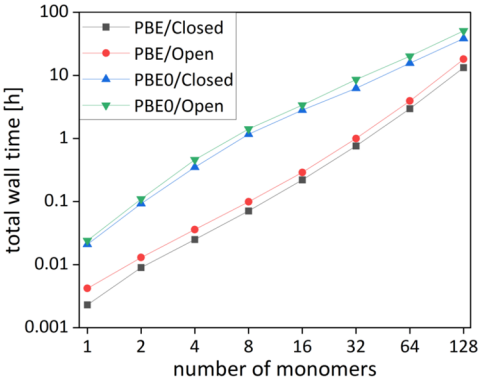

Figure 8. Total wall times for SCF and NMR calculations with respect to the number of glucose units (6-31G* basis). Wall times were measured on a single thread of an Intel Xeon Gold 6212U CPU (2.40 GHz). Reprinted with permission from ref 63. Copyright 2021 the Authors.

The occurrence of ring currents and the concept of aromaticity are not restricted to cyclic conjugated hydrocarbons and related organic compounds. All-metal systems may also sustain a ring current, and these systems are therefore classified as all-metal aromatic compounds. For instance, the endohedral $[Th@Bi_{12}]^{4-}$ cluster features a nonlocalizable π-orbital around the $\{Bi_{12}\}$ torus, which leads to a ring current.[205] Figure 9 shows a streamlined representation of this ring current, whose strength amounts to about 25 nA/T.[119,205]

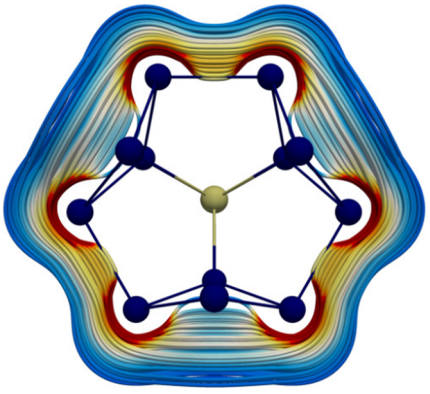

Figure 9. Aromatic ring current of $[Th@Bi_{12}]^{4-}$. The color scheme (red to blue) indicates strong to weak currents. Data from ref 205

Despite featuring only two delocalized π-electrons, almost the same ring current strength as that in porphine is induced. Here, the thorium atom in the torus center is only needed for stability and the synthesis, but it does not take part in the ring current. Furthermore, the open-shell variant $[U@Bi_{12}]^{3-}$ shows a strong ring current,[63] as the same π-orbital is occupied by two electrons.[205,206] Moreover, prismatic $\{Bi_6\}$-based clusters such as $[(CpRu)_3Bi_6]^-$ show ring currents of more than 25 nA/T.[207] Therefore, all-metal clusters help to push the frontiers of aromaticity.

3.8. Characterization of Novel Electronic Configurations in f-Block Elements by DFT and RPA Methods. Electronic structure calculations of large f-element complexes contain a great deal of complexity due to the competition between metal oxidation states, d- and f-shell occupations, spin

https://doi.org/10.1021/acs.jctc.3c00347
J. Chem. Theory Comput. 2023, 19, 6859−6890

coupling, and relativistic effects.[208] Computational studies in these compounds have to scan a range of formal electronic occupations and apply a range of techniques to ensure convergence to the desired electronic configuration, including Fermi smearing with suitable parameters,[209,210] and a combination of damping, level shifting,[211] and direct inversion in the iterative subspace (DIIS) extrapolation.[212] Moreover, the stability of the ground-state reference is a concern in calculations of molecular properties, for example, electronic absorption spectra.[213]

DFT results helped characterize the structures and properties of nontraditional Ln^{2+} complexes possessing the $4f^n5d^1$ configuration in the $[Ln(C_5H_4SiMe_3)_3]^-$ (Ln = Ce−Nd, Gd−Er),[214−217] $[Ln\{N(SiMe_3)_2\}_3]^-$ (Ln = La, Gd),[218,219] and $[Ln(Cp^{iPr_5})_2]$ (Ln = Tb, Dy) series.[220] The preference for the $4f^n5d^1$ configuration relative to the traditional $4f^{n+1}$ occupation of Ln^{2+} results from the stabilization of the Ln $5d_{z^2}$ orbital by the trigonal ligand environment or extremely bulky ligands. Nontraditional Ln^{2+} complexes show a characteristic intense absorption band in the visible range due to excitations from the occupied Ln 5d orbital. The prediction of UV−vis spectra of low-valent lanthanide complexes, in particular those with a nontraditional configuration, is improved by including diffuse augmentation in lanthanide basis sets.[221] DFT and RPA methods were employed to examine the strong ferromagnetic coupling between the Ln^{3+} centers in $[(C_5Me_5)_2Ln(\mu\text{-}S)_2Mo(\mu\text{-}S)_2Ln(C_5Me_5)_2]^-$ (Ln = Y, Gd, Tb, Dy) and the Mo→Ln electronic excitations in the near-infrared spectral region.[222] Excited-state studies of $[Ln(C_5Me_5)_2(C_5Me_4H)]$ and $[Ln(C_5Me_5)_2(\eta^3\text{-}C_3H_4)]$ complexes (Ln = Y, Dy, Lu) using TDDFT elucidated their unexpected photochemical activation, which was used to reduce dinitrogen and sulfur and to polymerize isoprene.[223,224]

Computational studies of neutral actinide complexes $[An(Cp^{iPr_5})_2]$ (An = Th, U, Pu, Am, Bk, No, Lr) (pentaisopropylcyclopentadienyl = Cp^{iPr_5}) using DFT predicted ground states with a linear ligand arrangement of S_{10} symmetry and significant An 6d orbital occupation for An = Th, U, Lr.[225] The calculations were carried out with the TPSS exchange−correlation functional,[226] Stuttgart−Cologne scalar-relativistic small-core effective core potentials (ECPs),[227] and the corresponding basis sets.[228,229] Mixed 5f/6d occupation was predicted in the corresponding Pu complex, while the An = Am, Bk, No complexes were found to have $5f^{n+1}$ configurations. The Pu and Am complexes showed a slight deviation from the perfectly symmetric structure, with Cp−M−Cp bending angles of 11° and 12°, respectively. The simulated absorption spectra showed intense peaks in the UV−vis range due to the metal−ligand charge transfer excitations from the An 6d orbital shown in Figure 10. Comparisons with the previously experimentally known Ln analogs (Ln = Dy, Tb)[220] suggested that the synthesis of the predicted actinocene complexes was thermodynamically feasible. The computational predictions received experimental confirmation for An = U while the results were still under review. Layfield and co-workers reported the synthesis of the linear S_{10}-symmetric "second-generation" uranocene $[U(Cp^{iPr_5})_2]$.[230] The U−Cp centroid distance was determined from crystallographic studies as 2.504 Å, in good agreement with the computational result of 2.483 Å. The measured UV−vis spectra showed broad and intense absorption, as predicted by TDDFT calculations.

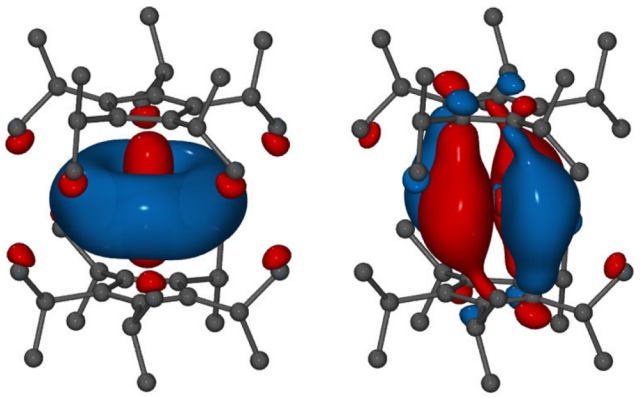

Figure 10. Contour plots of the HOMO (left) and LUMO (right) of $[An(Cp^{iPr_5})_2]$ determined with TPSS,[226] Stuttgart−Cologne scalar relativistic ECPs,[227] and the corresponding basis sets.[228,229] Orbital isovalues of 0.03 were used. Reprinted with permission from ref 225. Copyright 2019 American Chemical Society.

3.9. Damped Response Theory. Assessing light−matter interactions in extended or exotic systems is an active field of development in TURBOMOLE.[53,119,152,176,178,231,232] While root-by-root linear-response methods have been crucial for many applications, they are not suitable for spectrally dense systems or core excitation due to the high number of excited states (roots). Damped response theory,[233,234] or the equivalent complex polarization propagator approach,[235] provides a convenient framework to formulate resonance convergent response functions, circumventing these problems. It provides a convenient route to directly compute a variety of absorptive and dispersive effects in both UV−vis and X-ray frequency regions, which is particularly advantageous for large systems, and in frequency regions with high densities of states, as it does not require to solve eigenvalue equations for all contributing states and individual transitions matrix elements between them.[236] It also allows to compute nonlinear transition properties in the vicinity of additional resonances, *e.g.*, the resonant inelastic X-ray scattering (RIXS) transition amplitudes,[237] as well as properties at imaginary frequencies, like the C_6 dispersion coefficient.[232,238−240]

A number of implementations of damped response theory have been presented in the past two decades for time-dependent density functional theory and a variety of wavefunction methods.[80,113,232,235−238,241−254] TURBOMOLE is, to the best of our knowledge, the only program to date that offers damped linear response functions at the RI-CC2 level of theory[232,253] (available since release V7.7).

3.9.1. Damped Response for Multiscale Modeling. DFT-based damped response implementations in TURBOMOLE cover IR spectroscopy, VCD, and Raman spectroscopy, as well as absorption and electronic circular dichroism (ECD) in the visible and ultraviolet spectral range. Furthermore, this approach has recently been extended to the modern framework of the *GW*-BSE method, being especially useful for core excitations.[113,255]

At a given complex frequency $\omega_{ex} = \omega + i\gamma$, where ω and γ are the real and imaginary parts of the external field, respectively, the coupled perturbed equation[254,256]

$$\left[\begin{pmatrix} \mathbf{A} & \mathbf{B} \\ \mathbf{B}^* & \mathbf{A}^* \end{pmatrix} - \omega_{ex}\begin{pmatrix} \mathbf{1} & \mathbf{0} \\ \mathbf{0} & -\mathbf{1} \end{pmatrix}\right]\begin{pmatrix} \mathbf{x} \\ \mathbf{y} \end{pmatrix} = \begin{pmatrix} \mathbf{p}^{\nu} \\ \mathbf{p}^{\nu,*} \end{pmatrix} \quad (2)$$

is first solved. **A** and **B** are defined as

https://doi.org/10.1021/acs.jctc.3c00347
J. Chem. Theory Comput. 2023, 19, 6859−6890

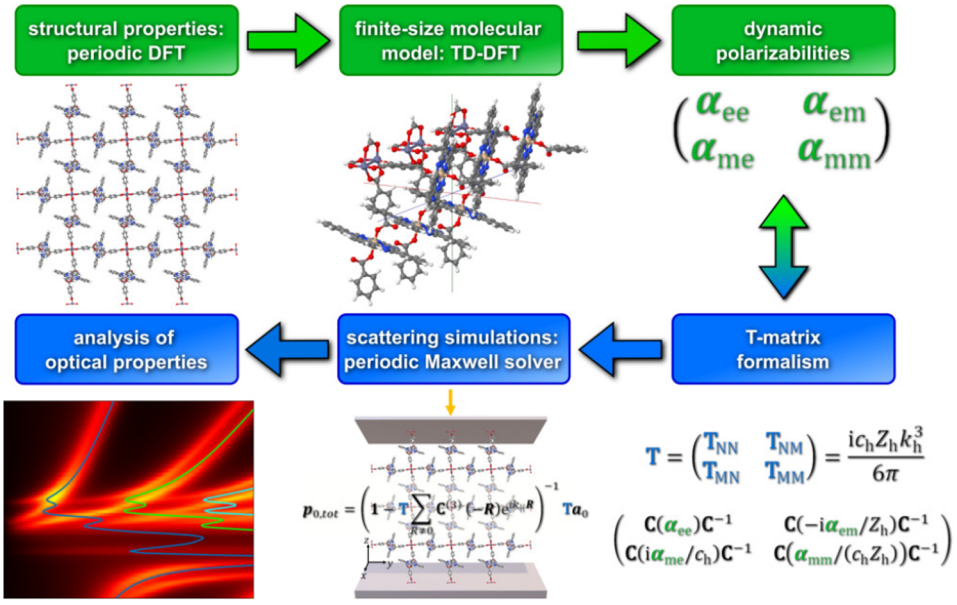

Figure 11. Scheme for T-matrix-based multiscale modeling of light−matter interactions using damped response polarizabilities as outlined in ref 254. Reprinted with permission from ref 254 under a CC BY-NC-ND license. Copyright 2022 the Authors.

$$A_{ai,bj} = (\varepsilon_a - \varepsilon_i) + v_{ai,jb} + f_{ai,jb} - K_{ij,ab}$$

$$B_{ai,bj} = v_{ai,bj} + f_{ai,jb} - K_{aj,bi}$$

ε_p marks orbital or quasiparticle energies, $v_{pq,rs}$ is a Coulomb integral, $f_{pq,rs}$ is the exchange-correlation kernel, if present, and $K_{pq,rs}$ is a exchange integral. The precise kinds of $f_{pq,rs}$ and $K_{pq,rs}$ depend on the chosen method.[254] $\mathbf{p}^{\nu}$ describes the external perturbation, *e.g.*, an electric or magnetic field.[254,256] The polarizability can then be calculated as

$$\alpha^{\nu\nu'}(\omega_{ex}) = \langle \mathbf{x}^{\nu}(\omega_{ex}), \mathbf{y}^{\nu}(\omega_{ex}) | \mathbf{p}^{\nu'}, \mathbf{p}^{\nu',*} \rangle \tag{3}$$

Damped polarizabilities and the related magnetizabilities have further emerged as the quantum-chemical cornerstone of the transition matrix (T-matrix) based approach for multiscale modeling of light−matter interactions.[254,257,258] This way, the functionalization of molecular structures within optical devices is possible. In that regard, optical cavities filled with molecular materials or metasurfaces of cylinders consisting of molecular materials can be designed. These devices exhibit tailored optical properties for a variety of applications, such as enhancing the circular dichroism of a chiral molecule. Through the multiscale approach depicted in Figure 11, the properties of a molecular unit and the macroscopic sample can be distinguished and combined to achieve a specific effect. Combining TURBOMOLE and, for example, the multilayered periodic general Mie method (mpGMM),[259] simulations and predictions of the light−matter interactions of layer-structured materials ranging from a few to hundreds of nanometers are now routinely possible.[254,260] To target molecular materials of arbitrary shape, the T-matrix approach was furthermore coupled with state-of-the-art homogenization techniques.[261] Combining classical electrodynamics and quantum mechanics has proven to be a worthwhile approach in the field of light−matter interactions, and TURBOMOLE will remain at the forefront of these developments.

3.9.2. Damped Response Theory for One-Photon Absorption and CD Spectra with RI-CC2. For RI-CC2, the equations for the damped response[237,262] of the cluster amplitudes are recast in a form that only involves effective matrices in the space of single excitations, avoiding the storage of parameters for the double excitation space.

$$\begin{bmatrix} \mathbf{A}_{SS}^{eff} - \omega\mathbf{1}_{SS} & i\boldsymbol{\Gamma}_{SS}^{eff} - i\gamma\mathbf{1}_{SS} \\ i\boldsymbol{\Gamma}_{SS}^{eff} - i\gamma\mathbf{1}_{SS} & \mathbf{A}_{SS}^{eff} - \omega\mathbf{1}_{SS} \end{bmatrix} \begin{bmatrix} t^x_{Re,S} \\ it^x_{Im,S} \end{bmatrix} = - \begin{bmatrix} \xi^{x,eff}_{Re,S} \\ i\xi^{x,eff}_{Im,S} \end{bmatrix} \tag{4}$$

Subscripts Re and Im represent real and imaginary components, respectively. The effective matrices in the equations above are

$$\mathbf{A}_{SS}^{eff}(\omega, \gamma) = \mathbf{A}_{SS} - \mathbf{A}_{SD}\frac{\Delta}{\Delta^2 + \gamma^2}\mathbf{A}_{DS} \tag{5}$$

$$\boldsymbol{\Gamma}_{SS}^{eff}(\omega, \gamma) = -\mathbf{A}_{SD}\frac{\gamma}{\Delta^2 + \gamma^2}\mathbf{A}_{DS} \tag{6}$$

where $\mathbf{A}_{SS}$, $\mathbf{A}_{SD}$, and $\mathbf{A}_{DS}$ are, respectively, the singles−singles, singles-doubles, and doubles-singles blocks of the CC2 Jacobi matrix. $\Delta^{ij}_{ab} = \varepsilon_a - \varepsilon_i + \varepsilon_b - \varepsilon_j - \omega$ are frequency-shifted orbital energy differences, and ω and γ are again the real and imaginary parts of the frequency of the external field, respectively. The effective right-hand sides are

$$\xi^{x,eff}_{Re,S} = \xi^{x}_{Re,S} - \mathbf{A}_{SD}\frac{1}{\Delta^2 + \gamma^2}(\Delta\xi^{x}_{Re,D} - \gamma\xi^{x}_{Im,D}) \tag{7}$$

$$\xi^{x,eff}_{Im,S} = \xi^{x}_{Im,S} - \mathbf{A}_{SD}\frac{1}{\Delta^2 + \gamma^2}(\Delta\xi^{x}_{Im,D} + \gamma\xi^{x}_{Re,D}) \tag{8}$$

where ξ^{x}_{S} and ξ^{x}_{D} are the single and doubles parts of the right-hand sides in the nonpartitioned form, respectively.[232,253] The partitioned formulation that avoids the need to store double excitation amplitudes and four-index integrals allows applications to system sizes otherwise not accessible at the CC2 level.

As an illustrative application, we computed the UV−vis absorption spectrum and electronic circular dichroism spectrum of a donor−acceptor cyclophane[263] shown in Figure 12. The absorption spectrum was obtained from calculations of

https://doi.org/10.1021/acs.jctc.3c00347
J. Chem. Theory Comput. 2023, 19, 6859−6890

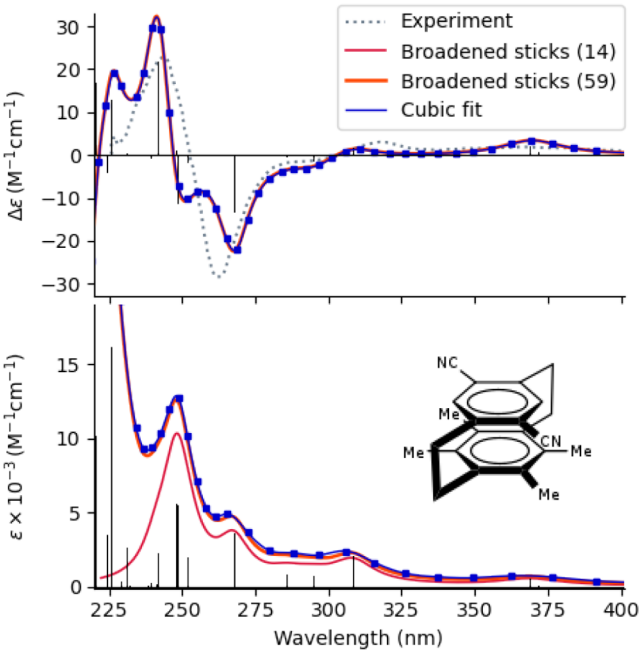

Figure 12. ECD (upper panel) and absorption spectra (lower panel) of ($4S_p$)-4,7-dicyano-12,13,15,16-tetramethyl[2.2]-paracyclophane computed at the CC2/aug-cc-pVDZ level. The MP2-optimized structure and the experimental CD spectrum have been taken from ref 263. Results from damped response theory are plotted as blue squares; the blue line is a cubic spline fit to these computed points. Stick spectra are the results from state-wise calculations, and the red and orange lines are obtained by convoluting these computed stick spectra with a Lorentzian broadening with a half-width-at-half-maximum of ≈1000 cm^{-1} including, respectively, the lowest 14 and 59 states.

the imaginary damped dipole polarizability and the ECD spectrum from the imaginary part of the optical rotation tensor in the velocity gauge. The asymmetric form[253] of the damped linear response function was used in the calculations (the symmetric form is also available).

Cyclophanes are well-studied examples of strained aromatic organic compounds (hydrocarbons) that exhibit planar chirality. The UV−vis spectrum is a typical example where the traditional state-wise approach converges only slowly with the number of states, as seen by the large difference between the results for 14 and 59 states that have been included for comparison. The problem does not appear in the damped response calculations.

Ongoing work is concerned with extending the implementation to induced and nonlinear spectra like MCD and RIXS.[253]

3.10. Nonadiabatic Molecular Dynamics Simulation for Spectroscopic Observables. Many photophysical and photochemical processes involve multiple electronic excited states coupled by radiative and nonradiative transitions. Efficient simulations of these processes by nonadiabatic molecular dynamics (NAMD) have recently become possible with transition dipole moments[30] and nonadiabatic couplings between excited states[32,264] computed within quadratic response TDDFT. The TURBOMOLE implementation of the multistate fewest-switches surface hopping (FSSH) algorithm enables simulations of molecular systems with 50−100 atoms and simulation times of >10 ps.[265,266] In addition, time-resolved fluorescence (TRF) and transient absorption (TA)[34] spectra can be simulated for comparison with experimental results.

The simultaneous treatment of multiple electronic excited states enables the examination of Kasha's rule.[267] According to Kasha's rule, singlet excited states energetically located above S_1 undergo ultrafast decay to the S_1 state and thus are not directly involved in fluorescence or photoactivated reactions. However, exceptions to Kasha's rule are well-known in molecules in the gas phase, such as azulene and pyrene.[268]

In our recent study, we used the NAMD implementation in TURBOMOLE to investigate the dynamics of several polycyclic aromatic hydrocarbons including pyrene, azulene, and bicyclo[6.2.0]decapentaene (BCDP, an isomer of azulene) at the PBE0/def2-SVP[269,270] level. Azulene was found to exhibit non-Kasha behavior due to emission from the S_2 state, in agreement with experiment.[271] BCDP obeys Kasha's rule and emits only from S_1. Previous studies assigned the high-energy shoulder in the pyrene fluorescence spectrum to non-Kasha emission as a result of the reverse $S_1 \rightarrow S_2$ internal conversion.[268,272−275] Multistate NAMD simulations describe the non-Kasha behavior as a combination of $S_1 \rightarrow S_2$ transitions and the change in the diabatic character of the S_1 state from dark (L_b) to bright (L_a) at points of near degeneracy between the S_1 and S_2 states. The high-energy shoulder in the fluorescence spectrum of pyrene can be understood as

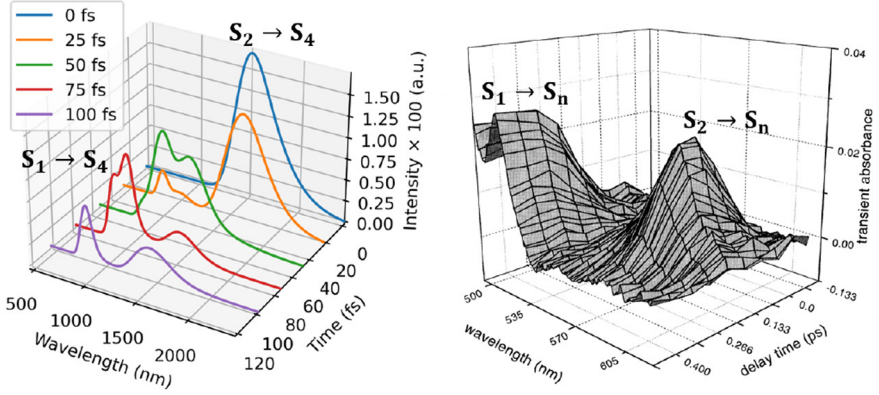

Figure 13. Computed (left) and experimental (right) TA spectra of pyrene in the gas phase. Band origins of S_1 and S_2 were shifted by −0.42 and −0.02 eV, respectively. Experimental spectra reprinted from ref 278. Copyright 1999 Hindawi Publishing Corporation. Distributed under a CC-BY license.

https://doi.org/10.1021/acs.jctc.3c00347
J. Chem. Theory Comput. 2023, 19, 6859−6890

originating from excited states with diabatic bright (L_a) character. The S_2 lifetime in pyrene was computed by an exponential fit of the decay of the state population as 63 fs, in agreement with the experiment value of 85 fs in methanol.[276] The S_1 lifetime of azulene was computed to be 2.2 ps in comparison to the experimental result of 1.4 ps in cyclohexane.[277] The computed lifetime of the S_1 state of BCDP was found to be 0.8 ps.

The NAMD trajectories were also used to obtain the TA spectrum of pyrene as an ensemble average of the Gaussian-broadened excited-state absorption and emission spectra (Figure 13). The experimental TA spectrum of pyrene shows an intense band at 580 nm and the growth of a steady state signal at around 450 nm corresponding to $S_2 \rightarrow S_n$ transient absorption that decays rapidly and a $S_1 \rightarrow S_n$ transition ($n > 4$), respectively.[276,278] NAMD simulations predict $S_2 \rightarrow S_4$ and $S_1 \rightarrow S_4$ bands at 1500 and 800 nm, respectively. The time evolution of the S_1 and S_2 states is in good agreement with experiment, while the absorption maxima ($\lambda(S_2 \rightarrow S_4) = 1500$ nm and $\lambda(S_1 \rightarrow S_4) = 800$ nm) are red-shifted due to truncation of the electronic excitation space.

3.11. Generating Function Methods for Vibrationally Resolved Electronic Spectroscopy. The vibrational structure of electronic spectra gives detailed information about molecular structure[279] and excited-state phenomena such as internal conversion and intersystem crossing.[280,281] In the case of conformationally flexible molecules, molecular dynamics sampling often allows the shape of electronic spectra to be accounted for.[282−287] However, this approach fails for rigid molecules with high vibrational frequencies.[288] In this case, special care must be taken to include the quantum nature of nuclear vibrations. Efficient theoretical simulation of molecular vibrationally resolved electronic (*i.e.*, vibronic) spectra has been advanced by switching from the time-independent approach,[289] which requires a tedious sum-overstates evaluation of Franck−Condon overlaps, to the time-dependent formalism (generating function approach), where the spectrum is given by the Fourier transform of an appropriate time-correlation function.[288,290−292] The `radless` module[288,293,294] makes use of the generating function method to compute vibrationally resolved absorption and emission spectra, as well as photoelectron ionization spectra. Spectra can be computed within the global harmonic approximation, which only requires equilibrium geometries for initial and final structures as well as vibrational spectra of both structures. The method accounts for the full Duschinsky rotation,[295] taking into account differences in initial and final state structures and vibrational modes. Due to its efficiency, the method can be applied to large molecules, such as polyaromatic hydrocarbons.[123,124,293,296,297] An extension of the module further allows the computation of emission and absorption spectra arising from singly occupied vibrationally excited initial states, allowing the simulation of single vibronic level (SVL) fluorescence[293] and vibrationally promoted electronic resonance (VIPER) spectra.[298]

In addition, the newly implemented semiclassical thawed Gaussian approximation (TGA)[291,299] offers an efficient way of evaluating the time-correlation function without resorting to the global harmonic approximation. The relation between vibronic spectroscopy and semiclassical dynamics stems from the wavepacket autocorrelation picture of the dipole time correlation function, first popularized by Heller.[290] In TGA, an initial Gaussian wave function is evolved under an effective local harmonic potential constructed at each step about the center of the wavepacket. As a result, its Gaussian form is conserved; the center of the wavepacket follows a classical trajectory, while its width is adjusted according to the instantaneous Hessian of the potential energy surface (PES). Whereas in the original *ab initio* TGA[300−303] the Hessian of the potential energy is updated over time, in the single-Hessian version,[304−306] implemented in TURBOMOLE as part of the `radless` module,[294] the Hessian is kept constant throughout the dynamics. Therefore, the overall additional cost compared to the conventional harmonic approximation is that of a single *ab initio* trajectory in the final electronic state, which is simulated using the `frog` module. Since the trajectory experiences the true anharmonic PES, the method can account for anharmonicity at least approximately, although it cannot describe more subtle quantum dynamics, such as wavepacket splitting or tunneling. The TGA approach has proven to be especially useful in systems with a large displacement between the ground- and excited-state minima and in systems with a double-well-shaped PES along a low-frequency mode in the final electronic state. In such molecules, the harmonic approach typically fails because the global harmonic PES constructed around one of the wells is not adequate. Moreover, in contrast to the global harmonic methods, the TGA results often depend weakly on the choice of the Hessian, as illustrated in Figure 14. Overall, the implementation in TURBOMOLE combines these advantages of TGA with accurate and efficient excited-state electronic structures, such as ADC(2) and CC2 methods.

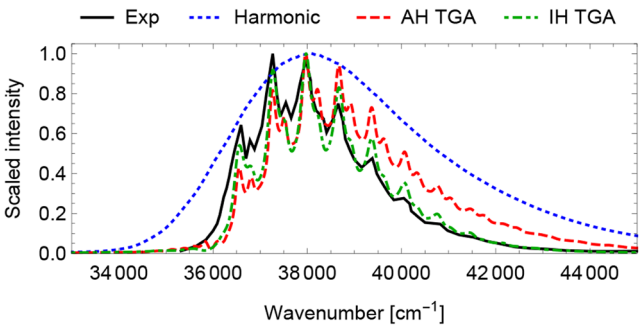

Figure 14. Experimental absorption spectrum of 1,2,4,5-tetrafluorobenzene (black) compared with the spectra simulated using the (adiabatic Hessian, AH) global harmonic method ("Harmonic", blue dotted line) and single-Hessian TGA with either the adiabatic Hessian (AH, red dashed line, evaluated in the excited electronic state at its corresponding optimized geometry) or the initial Hessian (IH, green dash-dotted line, ground-state Hessian computed at the ground-state optimized geometry). All electronic structure calculations, including geometry optimization, energies, and forces for the *ab initio* dynamics and Hessians, were performed at the CC2/def2-TZVP level. Adapted with permission from ref 294. Copyright 2022 American Chemical Society.

3.12. Molecular Properties from Self-Consistent GKS-spRPA. The generalized Kohn−Sham semicanonical projected random phase approximation (GKS-spRPA) provides a route for obtaining one-particle energies at the RPA level of theory.[16] These one-particle energies provide accurate estimates of ionization potentials (IPs) and electron affinities due to a correct description of orbital correlation and relaxation effects. Its computational cost was reduced from $O(N^6)$ to $O(N^4)$

https://doi.org/10.1021/acs.jctc.3c00347
J. Chem. Theory Comput. 2023, 19, 6859−6890

using well-known analytic continuation (AC) techniques.[307−309]

3.12.1. Applications to Nonvalence Anionic States and X-ray Emission Spectroscopy. The AC version of GKS-spRPA retains a high accuracy across energy scales from valence to core-ionization energies. The versatility of the AC GKS-spRPA was shown by its application to problems involving very weakly bound anionic states and very strongly bound core-hole ionization energies.

Nonvalence anionic states of molecules are weakly bound states where the excess electron occupies a diffuse orbital. The excess electron is bound by a combination of long-range electrostatic and correlation effects. When electrostatics are sufficient to bind an excess electron, the anionic states are referred to as nonvalence electrostatic-bound (NVEB), and when correlation effects are necessary the states are referred to as nonvalence correlation-bound (NVCB). Using a model water tetramer cluster, the GKS-spRPA approach was shown to provide electron affinities (EAs) from the lowest unoccupied molecular orbital (LUMO) energies that were within 10 meV of those provided by the EOM-CCSD(T)a* approach, see Figure 15. The high accuracy of the GKS-spRPA approach is

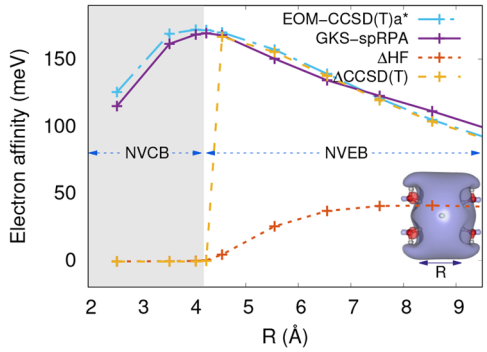

Figure 15. EAs of a water tetramer cluster for different dimer separations (R) computed using GKS-spRPA, Δ*HF*, ΔCCSD(T), and EOM-CCSD(T)a* methods. The inset shows the arrangement of the tetramer with a 70% isosurface of the LUMO at R = 4.047 Å. aug-cc-pVDZ basis sets were used for O and H atoms, and a 7*s*7*p* set of basis functions located at the center of the cluster was used. The shaded (unshaded) area of the plot corresponds to NVCB (NVEB) anionic states. Reprinted with permission from ref 309. Copyright 2021 American Chemical Society.

due to the correct description of long-range correlation effects. The AC approach introduces errors of less than 5 meV for nonvalence states.

The AC GKS-spRPA method can also be used for simulating nonresonant X-ray emission (XE) spectra using just the information from the one-particle eigenspectrum.[310] XE energies, ΔE, computed by taking the difference between core and valence IPs and the oscillator strengths, $f_{osc.}$, are evaluated within a frozen orbital approximation

$$f_{osc.} = \frac{2}{3} \sum_{\alpha=x,y,z} \Delta E |\langle \phi_c | \mu_\alpha | \phi_v \rangle|^2 \quad (9)$$

where ϕ_c and ϕ_v are the core orbital and valence GKS-spRPA orbitals involved in the XE process, respectively. The AC GKS-spRPA approach was used in conjunction with the scalar-relativistic (SR) X2C approach and uncontracted basis sets to estimate highly accurate XE spectra for molecules containing second- and third-period elements, for example, see Figure 16. Using uncontracted basis sets, the XE energies were found to

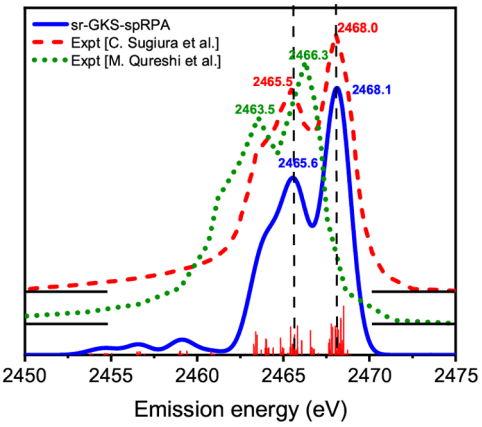

Figure 16. XE spectra of S_8 from experiments[311,312] and the SR-GKS-spRPA method.[310] The computed spectrum (in blue) was obtained by Gaussian broadening of the vertical transitions (red lines) using a width parameter of 1 eV. The vertical dashed lines denote the two intense peak positions for SR-GKS-spRPA. Reprinted and adapted with permission from ref 310. Copyright 2022 American Chemical Society.

have MAEs of 0.7 eV for both second and third period-based XE. The X2C-based AC GKS-spRPA approach thus enables the simulation of nonresonant X-ray emission within a simple one-particle picture while avoiding the use of empirical shifts or core-hole reference states. The latter is an appealing aspect, since issues related to variational instability, which are present in core−hole reference based methods, are avoided.

3.12.2. Orbital Ordering in Quinacridone. The accuracy of GKS-spRPA[16] for ionization potentials (IPs) compared to nonselfconsistent RPA[23] is due to partial satisfaction of functional self-consistency, which requires that the Kohn−Sham (KS) density equal the interacting density defined as the functional derivative of the ground-state energy with respect to the external potential.[16,317] A comparison of the GKS-spRPA orbitals and orbital energies to experimental photoelectron spectra of quinacridone illustrates this point, see Figure 17. Within both the KS and the GKS approach, the HOMO energy equals the first IP and subsequent lower-lying orbital energies approximate higher principal IPs.[318,319] However, this is often not true for semilocal density functional approximations. PBE[313] predicts a HOMO(−1), HOMO(−2), and HOMO(−3) ordering inconsistent with the results of optimally tuned range-separated hybrid functional (OT-RSH) calculations, yielding an accurate description of experimental photoelectron spectra and G_0W_0 IPs.[320,321] The canonical GKS-spRPA orbital ordering qualitatively agrees with the one OT-RSH one down to HOMO(−3), see Figure 17. Furthermore, the negative GKS-spRPA HOMO energy of 7.07 eV is close to the experimental IP of 7.23 eV,[322] whereas the negative PBE HOMO energy of 4.92 eV is significantly too small.

3.13. Subquadratic-Scaling PNO-CCSD(T) and PNO-CCSD(T)-F12 Methods. Since 2010, TURBOMOLE has supported accurate wave function methods for computing the ground-state energies of molecular configurations, and up to CCSD(T) and BCCD(T) are available, together with their explicitly correlated counterparts CCSD(T)(F12*) and

https://doi.org/10.1021/acs.jctc.3c00347
J. Chem. Theory Comput. 2023, 19, 6859−6890

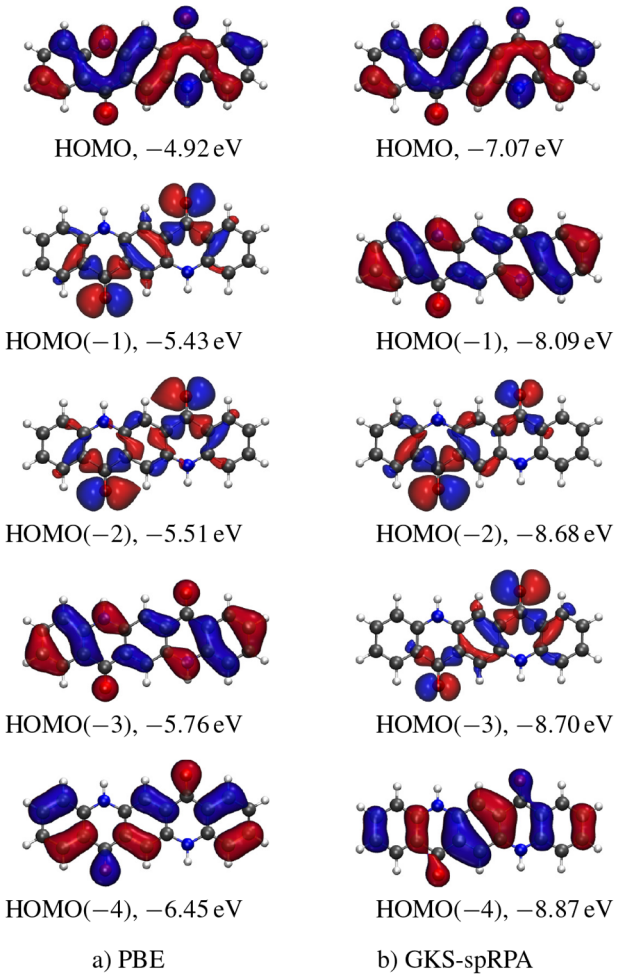

Figure 17. Plots of the five highest occupied orbitals at isovalues of ±0.02 shown for (a) PBE and (b) GKS-spRPA (with the PBE potential). The structure of quinacridone was optimized with PBE-D3[313−315] and cc-pVTZ basis sets.[316] Reproduced from ref 317 with the permission of AIP Publishing.

BCCD(T)(F12*).[68,69] When combined with a sufficiently large basis set, these methods deliver ground-state energy differences for reaction or interaction energies and potential energy surfaces to an accuracy that enables a quantative comparison with experimental results. The characteristics of the TURBOMOLE implementation are low memory and disk requirements and shared-memory parallelization, which make calculations on systems with ∼20 atoms routinely possible on modern machines.

To evaluate energies for larger molecules, the steep $O(N^7)$ scaling of the costs with system size must be overcome. Local approximations based on the short-ranged nature of electron correlation in molecules provide a route to near-linear scaling of costs with the system size. The PNO approach uses an approximate MP2 pair density to construct the set of local virtual orbitals for each pair that is best suited to describing the correlation of that pair. This, in combination with screening and local density fitting approximations, among others, reduces the scaling from $O(N^7)$ to $O(N)$ in the asymptotic limit. For ground-state energies, PNO-MP2, PNO-CCSD, and PNO-CCSD(T) explicitly correlated variants PNO-MP2-F12, PNO-CCSD(F12*), and PNO-CCSD(T)(F12*) have been available since V7.6.[70−73]

The efficiency of the implementation is greatly improved if the PNOs are expanded in projected atomic orbitals (PAOs) rather than directly in terms of atomic orbitals (AOs). This is known as domain-based local PNO theory (DLPNO). In TURBOMOLE, the PAO domains for each pair are determined also using the approximate MP2 density rather than by analyzing the MO coefficients and are consequently much more compact. The resulting domains are called principle domains.[323] Very recently, the principle domain approach has been extended to F12 theory, where principle domains and PNOs are required for every subspace in the F12 strong orthogonality projector.[324] In contrast to implementations in other software packages, we do not use the simplified "A" approximation[95] for the MP2-F12 contributions. This has the benefit that the energies converging smoothly to both the canonical limit and the basis set limit can be extrapolated using PNO extrapolation techniques.[325]

To illustrate the characteristics of the TURBOMOLE implementation and what is now possible, we report timings of PNO-CCSD(T) and PNO-CCSD(T)(F12*) calculations on a sequence of alkane chains and rock salt crystal fragments in Figure 18. The default tight (10^{-7}) PNO truncation threshold was used in all cases. The def2-TZVPP basis and def2-TZVP were used for C_nH_{2n+2} and Na_nCl_n, respectively, and calculations were run on a 48 core Intel processor with 200 Gb of memory. For the linear systems, the observed scaling is subquadratic, with $C_{128}H_{256}$ taking 15 h to complete. For the globular systems, the observed scaling is subcubic, with $Na_{50}Cl_{50}$ taking 45 h to complete. The F12 calculations are 2−3× more costly than non-F12 calculations but provide energies

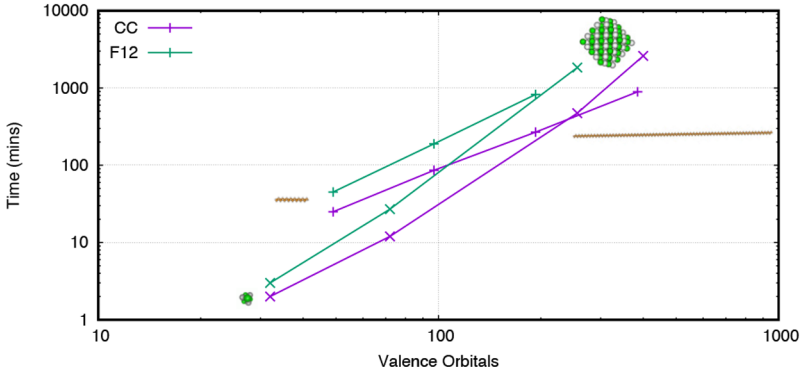

Figure 18. Wall-clock timings of PNO-CCSD(T) and PNO-CCSD(T)(F12*) calculations for alkane chains (+) and NaCl clusters (cross).

https://doi.org/10.1021/acs.jctc.3c00347
J. Chem. Theory Comput. 2023, 19, 6859−6890

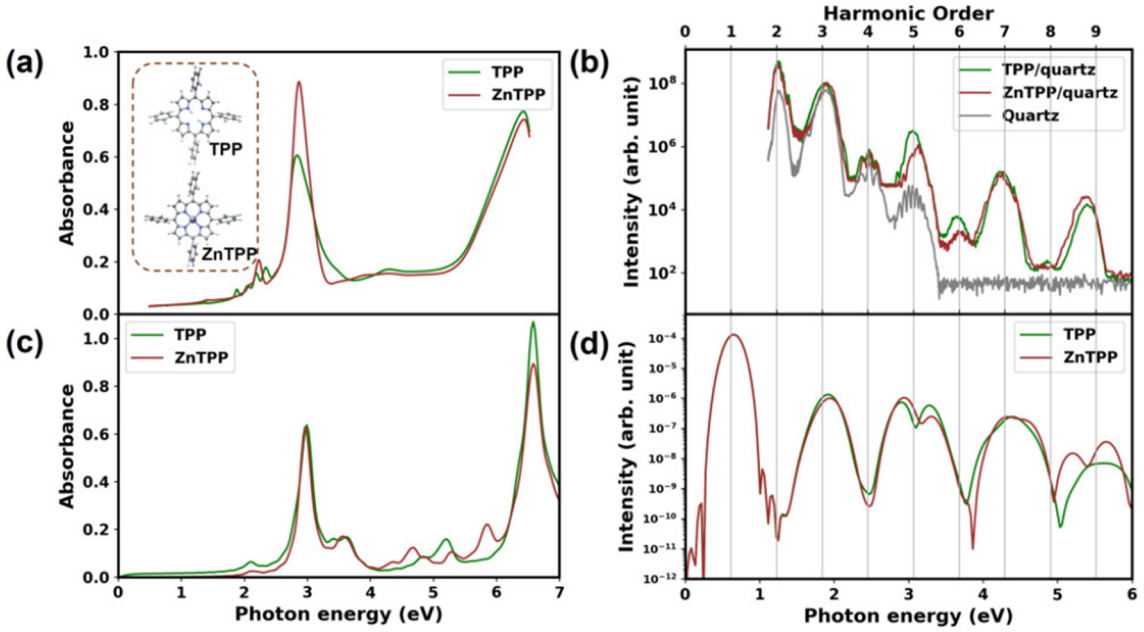

Figure 19. (a) Experimental linear absorption spectra and (b) HHG spectra of 100 nm thick TPP and ZnTPP samples. (c) Calculated linear absorption spectra and (d) HHG spectra of TPP and ZnTPP molecules.[326]

close to the basis set limit without requiring basis sets with a large number of AOs per atom.

3.14. Real-Time TDDFT for Molecules. While linear-response TDDFT can be used to study excitations under weak fields, a better understanding of nonlinear excited state dynamics at the femto- and sub-femtosecond time scales requires using RT-TDDFT.

RT-TDDFT for molecular systems has been implemented[89] within the `riper` module[55−58,327,328] using the Magnus propagator[329] and the predictor-corrector scheme[330] for time integration. The implementation utilizes density fitting and continuous fast multipole method (DF-CFMM) techniques[56] to speed up the KS matrix evaluation and scales almost quadratically with system size. Previously, the implementation was used to simulate absorption spectra over a wide range of frequencies by perturbing the molecules with weak electric fields.[89] Recently, the code has been extended to simulate high harmonic generation (HHG) spectra under intense laser pulses and was utilized to complement and analyze the pulse-induced electron dynamics in the organic semiconductor molecules tetraphenylporphyrin (TPP) and zinc-tetraphenylporphyrin (ZnTPP).[326] Figure 19 shows the good agreement of the experimental absorption and HHG spectra with the calculated ones. The difference in the first few harmonics is due to the fact that the experimental spectra contain contributions from the quartz substrate. Overall, the HHG and absorption spectra of both the porphyrins are quite similar due to the very similar electronic structure. Our simulations combined with experiments showed that $\pi \rightarrow \pi^*$ excitation plays a major role in the harmonic generation process in porphyrins. It was also discovered that resonant excitation leads to an early onset of nonperturbative behavior for the fifth harmonic, and similar effects are expected in Brunel harmonic generation with other organic materials.[326]

3.15. Developments of the DFT-Based Embedding Implementations. *3.15.1. Frozen Density Embedding Implementation.* Environment effects on molecular systems beyond static Coulomb potentials can be treated in TURBOMOLE with the conductor-like screening model (COSMO), polarizable embedding (PE), or frozen density embedding (FDE). Developments on COSMO and PE in TURBOMOLE have been presented in the previous review.[92] In contrast to the latter approaches, FDE is an atomistic QM/QM embedding model, which compared to QM/MM schemes uses a purely quantum-mechanical description of the total system and does not require any system-specific parametrizations prior to a calculation.

The implementation of FDE in TURBOMOLE was until recently restricted to just two subsystems, limiting its applicability. It has now been extended to handle arbitrarily many subsystems and to an FDE variant free of intermediates evaluated on the supermolecular orbital basis. For the embedding potentials, the newly implemented approach uses only electron densities and electrostatic potentials of the subsystems, which are computed on an integration grid generated for the total system. It is available for HF and DFT within the `dscf` and `ridft` programs. In combination with the `ricc2` program, it can be used to compute ground-state energies with MP2 and CC2 within the perturbation to the energy (PTE) or post-SCF reaction field coupling approaches. Excitation energies can be calculated within the frozen solvent approximations either with or without the kernel contributions. An important feature of the new implementation is the possibility to include pseudopotentials to improve the embedding potential. This allows for a more accurate description of the Pauli repulsion,[83] which is particularly important for electronically excited states to prevent unphysical charge spill-out. Besides all of the new features in FDE, it should also be mentioned that the current implementation is still limited to closed-shell subsystems.

To demonstrate its capabilities, we computed the first eight excitation energies of acetone at the CC2/aug-cc-pVDZ level embedded in 237 water molecules within the frozen solvent approximation. The active subsystem also includes two water molecules beside acetone and was treated with the HF method during the freeze and thaw (FaT) cycles, while the remaining

https://doi.org/10.1021/acs.jctc.3c00347
J. Chem. Theory Comput. 2023, 19, 6859−6890

water molecules were treated as separate subsystems using DFT with the PBE exchange correlation functional[313] and a gridsize of 3.[9,331] For the embedding potential, the PBE exchange correlation and the LC94 kinetic energy functional[332] with a gridsize of 3 were used. A comparison of the spectrum of solvated acetone with that of isolated acetone is shown in Figure 20.

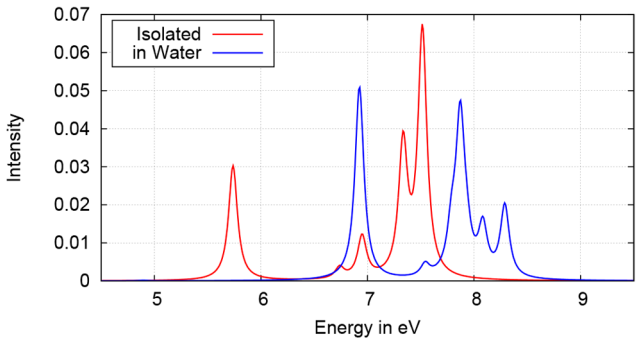

Figure 20. Computed spectra of acetone isolated (red) and surrounded by 237 water molecules (blue).

Recently, another update scheme of the subsystem densities was implemented, where the densities of all subsystems are updated simultaneously at the end of a FaT cycle instead of successive updates immediately after each subsystem calculation. Thus, the updated densities of each subsystem only contribute to the embedding potentials in the next FaT cycle, offering the advantage that interim results no longer depend on the enumeration of the subsystems; this allows the subsystem calculations to be performed simultaneously to improve efficiency in parallel runs. In Table 3, the wall times for both

Table 3. Wall Times for an Acetone Molecule in a Water Cluster for the Two Different Update Schemes[a]

update scheme	successive	simultaneous
$T(40)$, min	122.8	71.4
$T(1)$, min	369.6	586.2
speedup	3.0	8.2
n_{FaT}	6	10

[a] $T(X)$ represents the computational wall time obtained using X CPU cores. n_{FaT} gives the number of FaT iterations where it is necessary to reach convergence.

update schemes are compared for an reduced example of the above system containing only 78 water molecules. The timings show that this kind of parallelization leads to a decrease of the wall time in the case of many small subsystems where it is inefficient to parallelize single subsystem calculations over many CPU cores.

Future developments on the implementation of the FDE method aim to increase the applicability to systems containing large subsystems by combining it with PNO-based methods[333] and to reduce further the computation time of the Coulomb contribution to the embedding potential.

3.15.2. FDE and Projection-Based Embedding for Molecules and Solids. The FDE implementation described above is suitable for molecular and weakly interacting subsystems, as it employs embedding potentials based on approximate kinetic energy density functionals (KEDFs).[334] Recently, a DFT-based embedding scheme that treats both molecular and periodic systems on equal footing has been implemented within the `riper` module.[82] This implementation supports both FDE and projection-based embedding[335] (PbE) via a level-shift projection operator[336] (LSPO). PbE along with FaT cycles can be used to perform exact DFT-in-DFT embedding for molecules and solids and reproduce the exact total DFT energies, even for strongly interacting subsystems. Similar to the implementation in section 3.15.1, the embedding scheme is also coupled with correlated wave function (CW) methods and additionally with RT-TDDFT, enabling CW-in-DFT and RT-TDDFT-in-DFT calculations, respectively, on a cluster embedded in a molecular/periodic environment. However, here the CW-in-DFT calculations are performed only by adding the DFT-based embedding potential as a static term to the HF core potential of the active subsystem and obtaining the converged HF reference orbitals for post-SCF calculations. RT-TDDFT-in-DFT, on the other hand, does support updating a portion of the embedding potential during the time evolution in select cases.

As an illustrative application of the work, Figure 21 and Table 4 show that the solvatochromic shift in the first

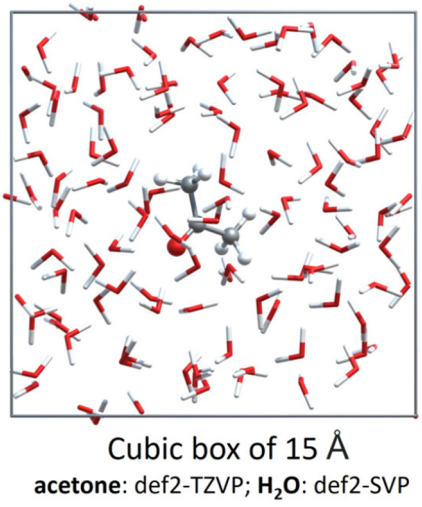

Figure 21. Acetone + H_2O in a cubic box of 15 Å containing 113 water molecules visualized using CrysX-3D Viewer.[337]

excitation energy, calculated using the CC2-in-DFT method (molecule-in-periodic) for an acetone molecule (active) solvated with 113 water molecules (periodic environment) in a cubic box with 3D periodicity, is in remarkable agreement with the shifts calculated using standard CC2[46] for acetone +

Table 4. Solvatochromic Shift ΔE of Acetone (Ac) S_1 Excitation in Water Calculated via CC2 on Ac + $(H_2O)_n$ Clusters and CC2-in-DFT (Periodic)[a]

	CC2			CC2-in-DFT (periodic)
	Ac + $(H_2O)_{20}$	Ac + $(H_2O)_{35}$	Ac + $(H_2O)_{48}$	Ac in 3D H_2O
ΔE, eV	0.19	0.19	0.21	0.20
N_{bf}	640	1000	1312	2872
T, h	0.88	8.36	37.33	4.10

[a] T denotes the wall time of the CC2 solvatochromic shift calculations.

https://doi.org/10.1021/acs.jctc.3c00347
J. Chem. Theory Comput. 2023, 19, 6859−6890

$(H_2O)_{20}$, acetone + $(H_2O)_{35}$, and acetone + $(H_2O)_{48}$ clusters at only a fraction of the computational cost. While beneficial, it is also important to acknowledge the limitations of the implementation as well, such as being restricted to only two closed-shell subsystems and using only LDA/GGA functionals for the embedding potential.

3.16. Periodic Hartree−Fock Exchange. In ref 328, we have presented a robust implementation of the periodic Hartree−Fock exchange in TURBOMOLE's `riper` module.[56,57] Without precautions, exchange matrix elements may be divergent, arising from an artificial periodicity of the density matrix. This periodicity of the density matrix is introduced in practical calculations by the discretization of wavevectors. The finite *k*-mesh determines in turn the size of the Born−von Kármán supercell. We have demonstrated[328] that a minimum image convention[338] removes the divergence for discrete *k*-meshes. While calculations with periodic HF exchange may be unstable for small supercells, stable SCF calculations and convergence of total energies are typically achieved for sufficiently large sizes of the supercells. The size of the supercell or *k*-mesh that is required for a reliable energy depends on the locality of the density matrix and hence both the electronic structure of the studied material and the chosen basis set. For selected insulators and semiconductors, we have demonstrated that HF total energies converge exponentially with the number of *k*-points,[328] see Figure 22.

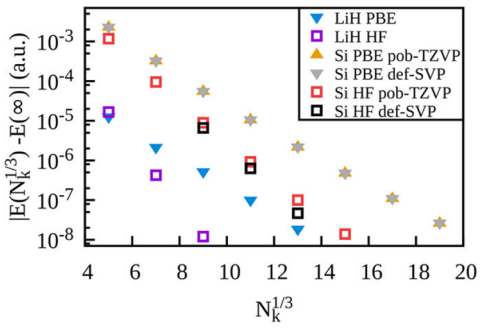

Figure 22. Self-consistent total energy differences $|E(N_k^{1/3}) - E(\infty)|$ per primitive cell for the PBE and HF methods. LiH is calculated in the rocksalt structure with a lattice constant of 4.084 Å[339] and is described with the basis set from ref 340. For Si, we use the diamond structure with a lattice constant of 5.430 Å[341] and the pob-TZVP[342] and def-SVP[343] basis sets. $E(\infty)$ is approximated by the energy obtained with a 31 × 31 × 31 *k*-mesh, since $|E(25) - E(31)| < 4 \times 10^{-10}$ a.u. for LiH and Si. Reprinted with permission from ref 328. Copyright 2018 American Chemical Society.

Through our implementation of periodic exchange, conventional Hartree−Fock calculations can be carried out with TURBOMOLE for periodic systems of any dimension. In addition, DFT calculations with hybrid functionals can now be performed routinely for semiconductors and insulators, and we showed successful applications of PBE0[313,344] and HSE06[345] hybrid and range-separated hybrid functionals.[328] As the next important step, analytical gradients shall be added for structure optimization. Furthermore, the Hartree−Fock exchange infrastructure that is available may be used in the development of new electronic structure methods for periodic systems that require exchange.

4. SELECT FEATURES UNDER DEVELOPMENT

4.1. Nuclear Electronic Orbital Method. Proton-coupled electron transfer (PCET) reactions are an important class of reactions that cannot be adequately described within the Born−Oppenheimer approximation.[346] A remedy to this problem is the nuclear electronic orbital (NEO) methods, which treat not only electrons but also the protons of selected hydrogen atoms quantum mechanically.[347,348] This is of particular importance for reactions that include proton transfer, such as, for example, acid−base reactions. The corresponding effects become especially important when the proton transfer is coupled to the electronic structure, such as in photoacids and photobases. In an initial proof-of-principle implementation, nuclear electronic orbitals were made available for the Hartree−Fock method (NEO-HF) and second-order Møller−Plesset perturbation theory (NEO-MP2) in a development version of TURBOMOLE. Furthermore, for the NEO-HF method, analytical gradients have since been implemented to allow for structure and basis set optimization.

Figure 23a shows the nuclear orbitals of the *trans*-Zundel isomer $H_9O_4^+$.[349] The nuclear orbital energies, as calculated by

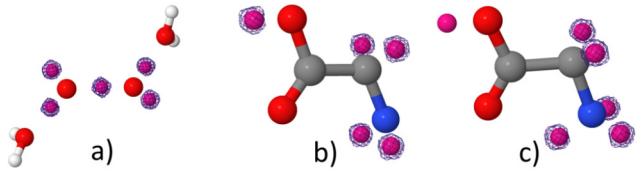

Figure 23. Nuclear orbitals as isosurfaces of the total densities with a cutoff of 0.0001 calculated with NEO-HF in the dscf program using the def2-TZVP basis for electrons and DZSPDN[348] for protons. White, classical proton; pink, center for basis set of a quantum proton; red, oxygen; and blue, nitrogen. (a) *trans*-Zundel isomer of $H_9O_4^+$, (b) neutral glycine, and (c) zwitterionic glycine.

the NEO-HF method, give an estimate of the binding energies of the protons. While the four outer ones have energies from −450 to −436 kcal/mol, the central one is the least stable with an energy of −417 kcal/mol. If the outer two water molecules are removed, the energies change to between −400.5 and −399.6 kcal/mol for the four outer protons and −371 kcal/mol for the central one. This hints at the ionic cluster being stabilized by the outer water molecules.

The protons of the neutral glycine molecule in Figure 23b have orbital energies between −633 and −546 kcal/mol, with the least stable one being the one at the carboxyl group. The zwitterionic glycine structure in Figure 23c has been optimized as a positively charged system with six classical protons. A NEO-HF calculation with five protons resulted in proton orbital energies between −663 and −558 kcal/mol. This demonstrates that protonation and deprotonation at certain sites can be elegantly investigated by the *ab initio* occupation of nuclear orbitals at the respective sites instead of placing classical nuclei according to intuition.

Implementing these methods in TURBOMOLE allows for the use of highly efficient schemes that already exist for purely electronic methods. The NEO methods can also use various existing programs to analyze the results. In future developments, NEO−DFT[350] will be implemented for molecular and periodic[351] systems.

https://doi.org/10.1021/acs.jctc.3c00347
J. Chem. Theory Comput. 2023, 19, 6859−6890

4.2. Hartree−Fock-Based Adiabatic Connection Models. MP2[352] is one of the most used approaches for wavefunction-based correlation energies, as well as being used in the double-hybrid (DH) DFT.[353,354] Nevertheless, the MP2 method shows several limitations, *e.g.*, it overestimates the correlation energy in large systems[355] and diverges for systems with a vanishing gap.[356] For this reason, several regularized and/or scaled MP2 methods have been developed.[356−358]

Another more recent path in this direction is the Møller−Plesset or Hartree−Fock adiabatic connection (HFAC) method.[359] In the HFAC approach, the correlation energy E_c is given as a nonlinear function of E_{MP2}, E_x^{HF} (the HF exchange energy), and two semilocal functionals of the HF density ($W_c = W_c[\rho^{HF}]$ and $W_c' = W_c'[\rho^{HF}]$). The latter are derived from the strong-correlation regime,[360,361] and we have

$$E_c = F(E_{MP2}, E_x^{HF}, W_c, W_c') \tag{10}$$

The HFAC method *de facto* includes an infinite-order resummation of the MP correlation series thanks to the interpolation with the strong-correlation limit, as in the more conventional AC based on DFT.[362] The nonlinear function F can be approximated by modeling the HFAC curve at various coupling strengths[359] using known exact asymptotic conditions.[361,363] Consequently, F satisfies two important limits:

$$E_c \to \begin{cases} E_{MP2} & \text{for } E_{MP2} \to 0 \quad \text{(a)} \\ G(E_x^{HF}, W_c, W_c') & \text{for } E_{MP2} \to -\infty \quad \text{(b)} \end{cases} \tag{11}$$

where G is a nonlinear function whose form depends on the choice of F. For well-behaving approximations of F, the condition in eq 11b yields a finite energy whenever $E_{MP2} \to -\infty$, thus removing one main limitation of MP2 and DH functionals for systems with a vanishing gap. The condition (eq 11a) is an exact condition,[359] which is violated in all the regularized MP2 methods.[356,357] Thus, the HFAC method allows us to overcome the main drawbacks of the MP2 approach within a well-defined theoretical framework at the small extra cost of a post-HF semilocal DFT calculation.

Some working approximations of F have been proposed (*e.g.*, ISI,[362,364] RevISI,[365] and MPACF1[363]), and they have been implemented in TURBOMOLE together with the currently available DFT approximations for W_c and W_c'.[360,366] Note that eq 10 is not size-consistent for systems composed of different species of fragments (as F is a nonlinear function). However, a size-consistent correction (SCC)[367] can be readily computed with TURBOMOLE at no additional costs, allowing the calculation of dissociation curves.

Two examples of applications where MP2 and DH functionals fail whereas the HFAC implementation can be readily used are displayed in Figure 24.

Figure 24a shows the dissociation curve for the coronene dimer, a prototype for a wide class of problems that are hardly tractable with high-level correlated wave function methods but are poorly described by MP2 because of the lack of high-order correlation contributions.[355] In constrast, HFACM methods are very close to the available reference data at the equilibrium geometry. The MPACF1 functional has been tuned on dispersion complexes and on average exhibits an error 2−5× smaller than MP2.[363]

Figure 24b shows the H_2 dissociation in a restricted formalism, a prototype of a strongly correlated system.[129−131,357,364] All methods work well close to the equilibrium geometry. However, for a larger separation where the energy-gap closes, MP2 and DH functionals rapidly diverge. HFAC methods, however, remain well behaved, yielding a finite interaction energy, see eq 11b. The exact result is not reproduced, as the available HFAC functionals are approximated and do not take into account the recent theory developments.[361] Further development and testing are thus required, and the HFAC implementation in TURBOMOLE represents an efficient platform to this end.

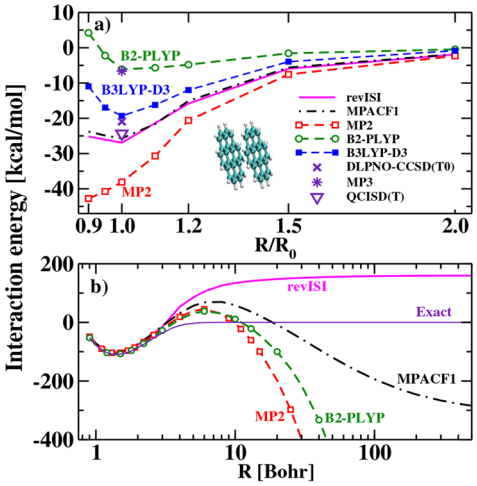

Figure 24. Dissociation energy curves for (a) a coronene dimer and (b) H_2, as computed with different methods. For the coronene dimer, reference data are taken from the literature,[368,369] and the equilibrium distance is R_0 = 3.458 Å. All calculations were performed with the *hfacm* script. The coronene dimer results are based on a complete basis set extrapolation from cc-pVQZ results. H_2 calculations employed the aug-cc-pVQZ basis set. The strong-correlation functional used in the HFAC results is the hPC model.[366]

4.3. Approximate TDDFT Approaches. Time-dependent density functional theory is still the most-used approach for the calculation of excitation energies of molecular and extended systems, thanks to its favorable accuracy/computational-cost ratio. Nevertheless, the computational cost of first-principles TDDFT calculations limits routine calculations to systems with a few hundreds of atoms, depending on the choice of the exchange-correlation (XC) functional. Different methods and algorithms have been developed in order to increase the TDDFT efficiency,[370−373] most prominently the RI-*J* technique.[374−377] Another efficient, though approximated, path is to perform a semiempirical tight-binding linear-response (TBLR) approximation,[378−380] using first-principles KS orbitals and eigenvalues. TBLR methods speed up the TDDFT calculation by about two orders of magnitude. TBLR is accompanied by a loss in accuracy of about 0.1−0.2 eV, which is comparable to the overall TDDFT accuracy.[381,382] More recently, it has been shown that, for semilocal XC functionals, the TBLR approaches can be considered as an approximation of the RI-TDDFT scheme with only one s-type Gaussian basis function per atom in the RI auxiliary basis set (TDDFT-as)[383] and with the three index RI integrals replaced with a Löwdin approximation.[378−380] Instead, in the TDDFT-as method, the latter approximation is not employed and, moreover, the calculation of the semilocal XC kernel contribution on the grid is not required,[383] as it can be modeled/approximated by the same exponent α of the s-type Gaussian auxiliary basis

https://doi.org/10.1021/acs.jctc.3c00347
J. Chem. Theory Comput. 2023, 19, 6859−6890

function. However, the exponent α needs to be optimized for each atom type separately.

Here, we shortly report on results for two computationally expensive cases using the PBE[313] functional. First, a 120 atom silver nanoparticle, Ag_{120}, with T_d symmetry calculated using the def-SVP[41] basis set. Second, a fullerene with C_1 symmetry calculated using the def2-TZVP[270] basis set. Both systems contain only a single type of atom. We optimized α by minimizing the root-mean square (RMS) averaged excitation energy error E_{avg}, avoiding state flipping,[383] and considering 400 t_2 (600 a) excited states for the silver nanoparticle (fullerene). The optimization yields $\alpha_{Ag} = 0.036$ with $E_{avg} = 5$ meV and $\alpha_C = 0.18$ with $E_{avg} = 12$ meV for Ag_{120} and C_{60}, respectively, as reported in Table 5. The amazing accuracy is also retained when the maximum error on all excitation energies E_{max}, including many optically dark states in C_{60}, is considered. This is demonstrated in Table 5 and Figure 25, where we report the absorption spectra of the two systems considered. The TDDFT-as absorption spectra in Figure 25, reported on a log scale to also highlight states with low oscillator strengths, can be hardly distinguished from the reference TDDFT results in a wide energy range for both systems investigated. Compared to TBLR approaches,[383] the accuracy of TDDFT-as is therefore increased by an order of magnitude, showing that it is a highly competitive approach.

Table 5. Optimized Exponent of the s-Type Auxiliary Basis Function, RMS-Averaged (E_{avg}) and Maximum (E_{max}) Errors on Excitation Energies, and Computational Cost (on a Single-Core Intel Xeon Gold 6132) for the First Davidson Step for the RI-J and XC Part for the Two Systems Considered[a]

	Ag_{120}	C_{60}
α	0.036	0.18
E_{avg}, meV	5	12
E_{max}, meV	11	39
TDDFT RI-J, s	5719	7148
TDDFT-as RI-J, s	116	104
TDDFT XC, s	22363	29845
TDDFT-as XC, s	0	0

[a]In the TDDFT(-as) calculations, the 1s core orbital and the 4s4p orbitals were kept frozen in C_{60} and Ag_{120}, respectively.

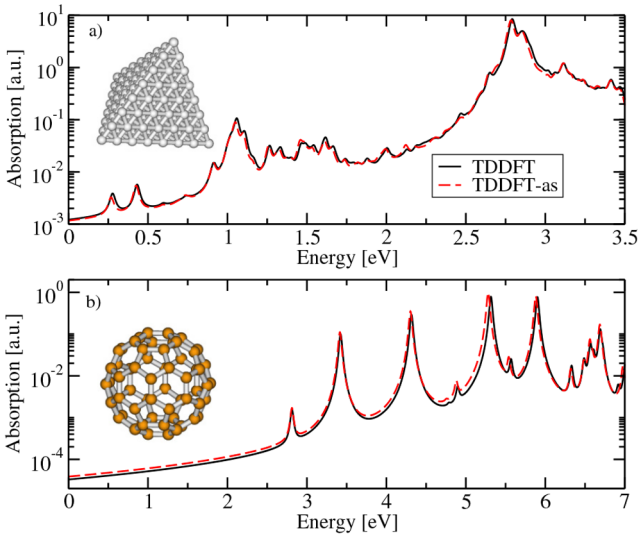

Figure 25. TDDFT and TDDFT-as absorption spectra (in log scale) for (a) Ag_{120} and (b) fullerene determined using the PBE XC functional and a Lorentzian broadening of 20 meV.

The computational speed up of the TDDFT-as method is shown in Table 5. The XC part is completely neglected, and the RI-Coulomb part is reduced by a factor of 50−70 due to the strongly reduced dimension of the auxiliary basis set.

More recently, TDDFT-as was extended to hybrid functionals and defined across the periodic table, forming the TDDFT-ris model.[384] Using the PBE0 hybrid functional[344] on a test set comprising small-to-large organic molecules, TDDFT-ris has an average error of $E_{avg} = 60$ meV[384] compared to an average error of $E_{avg} = 240$ meV for sTDDFT.[378,379] Thus, the TDDFT-as and TDDFT-ris methods, both fully available in the next release, are efficient and accurate approximations of standard TDDFT, providing a significantly less empirical alternative to TBLR approaches. Thanks to the flexible and efficient implementation, accurate simulations of the absorption spectra of large nanoparticles and organic molecules are available at a fraction of the computational cost of standard TDDFT.

4.4. Multiscale Modeling Extensions for the Nonlinear Optical Response of Molecular Materials. Further ongoing work concerning multiscale modeling of optical molecular materials is envisaged in the direction of integrating the automatic construction of T-matrices, as used in the multiscale approach in section 3.9.1. These T-matrices or effective material parameters derived thereof are often used in scattering codes and finite-element method-based programs. Examples for such codes are the multilayered periodic general Mie method code (mpGMM), JCMsuite, and COMSOL Multiphysics, which describe light−matter interactions of complex optical devices made form novel materials. In the foreseeable future, the current developments and implementations will be converted into a fully fledged workflow for optical material simulations. This will make the *ab initio*-based T-matrix approach available to a broader scientific community interested in a bottom-up approach of simulating complex artificial molecular materials and photonic devices. Future work will be dedicated to nonlinear optical properties, as this topic is currently seeing increasing interest in the scientific community. The change in the molecular dipole moment $\Delta\mu_i$ (polarization) upon exposure to the oscillating external electric field E_i at the excitation frequencies is often expressed as a power series of the incident field E.

$$\Delta\mu_i = \sum_j \alpha_{ij}E_j + \frac{1}{2}\sum_{j,k}\beta_{ijk}E_jE_k + \frac{1}{6}\sum_{j,k,l}\gamma_{ijkl}E_jE_kE_l + \ldots \quad (12)$$

In eq 12, α_{ij} denotes the polarizability, β_{ijk} denotes the first hyperpolarizability, γ_{ijkl} denotes the second hyperpolarizability and so on. Currently, optical multiscale studies are limited to linear response, taking into account α_{ij}.[254,261] To take into account nonlinear effects, *i.e.*, β_{ijk} and/or γ_{ijkl}, the additionally arising quadratic (and/or cubic) response terms of eq 12 need to be taken into account. While TURBOMOLE already allows calculation of the first hyperpolarizabilities β_{ijk} for real frequencies, ongoing work is dedicated to expanding this toward general complex frequencies. Ultimately, this will allow not only studies of the nonlinear light−matter interactions on

https://doi.org/10.1021/acs.jctc.3c00347
J. Chem. Theory Comput. 2023, 19, 6859−6890

the individual molecular level but also the construction of "hyper-T-matrices". The latter can be used to investigate for example second-harmonic generation (SHG) efficiencies, macroscopic second-order susceptibilities, and two-photon absorption of photonic devices made from molecular materials.

4.5. Relativistic Effects and Magnetic Properties of Periodic Systems. As is evident from the many sections in this Review focusing on molecules, TURBOMOLE was initially developed to study finite molecular systems. However, the code infrastructure was extended to support calculations with periodic boundary conditions almost 15 years ago,[55] and developments for molecular systems can be transferred to the periodic code. Recently, a two-component DFT framework was implemented for ground-state calculations, supporting energies and various plotting options for bands and the electron density on a grid.[385] The reason to use such a framework for periodic systems is twofold. First, it allows for the inclusion of spin−orbit coupling in a variational ansatz for relativistic effects. Second, the 2c formalism is necessary to study magnetic properties and arbitrary spin alignments, *i.e.*, ferromagnetic, antiferromagnetic, and noncollinear spin textures.

A pilot application to the band gaps of AgI is shown in Table 6. Here, relativistic effects substantially affect the band energies. That is, the nonrelativistic approach shows a large deviation toward the four-component (4c) ansatz directly based on the Dirac equation. In contrast, the scalar 1c approach yields substantial improvement. The spin−orbit 2c approach, employing ECPs, further improves upon these results and is in good agreement with the four-component reference. This shows that the 2c framework serves as an excellent approximation with drastically reduced computational demands. Here, a Kramers-restricted (time-reversal symmetric) approach is available for closed-shell systems, whereas a Kramers-unrestricted approach (breakdown of time-reversal symmetry) is used for open-shell systems. For the latter, a noncollinear treatment of the electron spin is applied.

Table 6. Energy Band Gaps (in eV) of Three-Dimensional AgI (Lattice Constant 6.169 Å, Rocksalt Structure[386]) Obtained for Various *k*-Points with the PBE Functional[a]

method	L−L	Γ−Γ	X−X	L−X
NR	3.89	3.42	3.71	1.48
1c ECP	3.49	2.16	2.98	0.65
2c ECP	3.25	1.82	2.69	0.41
4c DKS	3.25	1.88	2.74	0.49

[a]Nonrelativistic calculations (NR) are performed with the TZVPalls2/TZVPall basis set,[387] whereas the ECP-based 1c and 2c calculations use the dhf-SVP(-2c) bases.[388] Results taken from ref 385. Four-component Dirac−Kohn−Sham (DKS) reference values are taken from ref 389, employing the uncontracted Dyall-VDZ basis.[390,391].

Current endeavors cover the extension of the 2c formalism to energy gradients[56] and the stress tensor,[59] as well as the inclusion of the current density,[151] see section 3.2. This will allow us to perform structure optimizations and sophisticated studies with τ-dependent functionals, as the current density is of crucial importance for materials such as Weyl semimetals[392] and magnetic Hopfions.[393] Another strong point of the 1c implementation for periodic systems is the availability of HF exchange, which can be applied at a reasonable cost as localized basis functions are used.[328] This allows for the use of generally all available global and range-separated hybrid functionals in a stable and convergent framework. Extension of this feature to the 2c framework will allow for a more precise description of band gaps and other properties. For example, for magnetic properties it was shown that the amount of HF exchange incorporated is crucial.[119] Therefore, a robust implementation of 2c HF exchange in the periodic framework will be useful in determining related quantities also for materials in the solid state and nanostructures.

5. OUTLOOK

The quality of a code strongly correlates with the health and functioning of its developers' community.[394] TURBOMOLE developers are organized in small units pursuing their own scientific agendas, as illustrated by this Review. While this is a typical and, to a degree, necessary *modus operandi* for large scientific coding projects, the need to secure original authorship and demonstrate scientific independence often conflicts with sharing plans and code, taking collective responsibility, and avoiding "technical debt". As a result, TURBOMOLE has historically not been particularly easy to use, contribute to, or interface with other codes. TURBOMOLE GmbH was founded precisely to address these issues and has provided a framework to advance common goals and improve code quality. Nevertheless, incentives to collaborate and adopt sustainable coding practices remain few and far between. The future of the TURBOMOLE project will vitally depend on whether the conditions set by the environment, *i.e.*, academic institutions, funding agencies, reviewers, the developers, and not least the users, foster a thriving and collaborative community, which incentivizes continued investment in the code base.

AUTHOR INFORMATION

Corresponding Authors

Filipp Furche − *Department of Chemistry, University of California, Irvine, Irvine, California 92697-2025, United States*; orcid.org/0000-0001-8520-3971; Email: filipp.furche@uci.edu

Christof Hättig − *Lehrstuhl für Theoretische Chemie, Ruhr-Universität Bochum, 44801 Bochum, Germany*; orcid.org/0000-0002-5752-2710; Email: christof.haettig@rub.de

Marek Sierka − *Otto-Schott-Institut für Materialforschung, Friedrich-Schiller-Universität Jena, 07743 Jena, Germany*; orcid.org/0000-0001-8153-3682; Email: marek.sierka@uni-jena.de

David P. Tew − *Physical and Theoretical Chemistry Laboratory, University of Oxford, Oxford OX1 3QZ, United Kingdom*; orcid.org/0000-0002-3220-4177; Email: david.tew@chem.ox.ac.uk

Florian Weigend − *Fachbereich Chemie, Philipps-Universität Marburg, 35032 Marburg, Germany*; orcid.org/0000-0001-5060-1689; Email: florian.weigend@chemie.uni-marburg.de

Authors

Yannick J. Franzke − *Fachbereich Chemie, Philipps-Universität Marburg, 35032 Marburg, Germany*; orcid.org/0000-0002-8344-113X

https://doi.org/10.1021/acs.jctc.3c00347
J. Chem. Theory Comput. 2023, 19, 6859−6890

Christof Holzer − *Institute of Theoretical Solid State Physics, Karlsruhe Institute of Technology (KIT), 76131 Karlsruhe, Germany;* orcid.org/0000-0001-8234-260X
Josefine H. Andersen − *DTU Chemistry, Department of Chemistry, Technical University of Denmark, DK-2800 Kongens Lyngby, Denmark*
Tomislav Begušić − *Division of Chemistry and Chemical Engineering, California Institute of Technology, Pasadena, California 91125, United States;* orcid.org/0000-0002-7942-4134
Florian Bruder − *Fachbereich Chemie, Philipps-Universität Marburg, 35032 Marburg, Germany*
Sonia Coriani − *DTU Chemistry, Department of Chemistry, Technical University of Denmark, DK-2800 Kongens Lyngby, Denmark;* orcid.org/0000-0002-4487-897X
Fabio Della Sala − *Institute for Microelectronics and Microsystems (CNR-IMM), 73100 Lecce, Italy; Center for Biomolecular Nanotechnologies @UNILE, Istituto Italiano di Tecnologia, 73010 Arnesano, Italy;* orcid.org/0000-0003-0940-8830
Eduardo Fabiano − *Institute for Microelectronics and Microsystems (CNR-IMM), 73100 Lecce, Italy; Center for Biomolecular Nanotechnologies @UNILE, Istituto Italiano di Tecnologia, 73010 Arnesano, Italy;* orcid.org/0000-0002-3990-669X
Daniil A. Fedotov − *DTU Chemistry, Department of Chemistry, Technical University of Denmark, DK-2800 Kongens Lyngby, Denmark; Institute of Chemistry, The Hebrew University of Jerusalem, Jerusalem 91904, Israel*
Susanne Fürst − *Institut für Chemie, Theoretische Chemie/Quantenchemie, Sekr. C7, Technische Universität Berlin, 10623 Berlin, Germany*
Sebastian Gillhuber − *Institute of Inorganic Chemistry, Karlsruhe Institute of Technology (KIT), 76131 Karlsruhe, Germany;* orcid.org/0000-0002-2135-0208
Robin Grotjahn − *Department of Chemistry, University of California, Irvine, Irvine, California 92697-2025, United States;* orcid.org/0000-0002-7160-2581
Martin Kaupp − *Institut für Chemie, Theoretische Chemie/Quantenchemie, Sekr. C7, Technische Universität Berlin, 10623 Berlin, Germany;* orcid.org/0000-0003-1582-2819
Max Kehry − *Institute of Physical Chemistry, Karlsruhe Institute of Technology (KIT), 76131 Karlsruhe, Germany;* orcid.org/0000-0002-2093-7808
Marjan Krstić − *Institute of Theoretical Solid State Physics, Karlsruhe Institute of Technology (KIT), 76131 Karlsruhe, Germany*
Fabian Mack − *Institute of Physical Chemistry, Karlsruhe Institute of Technology (KIT), 76131 Karlsruhe, Germany;* orcid.org/0000-0002-9284-327X
Sourav Majumdar − *Department of Chemistry, University of California, Irvine, Irvine, California 92697-2025, United States*
Brian D. Nguyen − *Department of Chemistry, University of California, Irvine, Irvine, California 92697-2025, United States;* orcid.org/0000-0001-7713-1912
Shane M. Parker − *Department of Chemistry, Case Western Reserve University, Cleveland, Ohio 44106, United States;* orcid.org/0000-0002-1110-3393
Fabian Pauly − *Institute of Physics, University of Augsburg, 86159 Augsburg, Germany;* orcid.org/0000-0001-8017-2379
Ansgar Pausch − *Institute of Physical Chemistry, Karlsruhe Institute of Technology (KIT), 76131 Karlsruhe, Germany;* orcid.org/0000-0003-1895-2037
Eva Perlt − *Otto-Schott-Institut für Materialforschung, Friedrich-Schiller-Universität Jena, 07743 Jena, Germany*
Gabriel S. Phun − *Department of Chemistry, University of California, Irvine, Irvine, California 92697-2025, United States;* orcid.org/0000-0002-1242-2759
Ahmadreza Rajabi − *Department of Chemistry, University of California, Irvine, Irvine, California 92697-2025, United States;* orcid.org/0000-0002-2188-762X
Dmitrij Rappoport − *Department of Chemistry, University of California, Irvine, Irvine, California 92697-2025, United States;* orcid.org/0000-0002-5024-7998
Bibek Samal − *Department of Chemical Sciences, Tata Institute of Fundamental Research, Mumbai 400005, India;* orcid.org/0000-0002-3510-3830
Tim Schrader − *Otto-Schott-Institut für Materialforschung, Friedrich-Schiller-Universität Jena, 07743 Jena, Germany;* orcid.org/0000-0002-5323-5589
Manas Sharma − *Otto-Schott-Institut für Materialforschung, Friedrich-Schiller-Universität Jena, 07743 Jena, Germany;* orcid.org/0000-0002-5346-6280
Enrico Tapavicza − *Department of Chemistry and Biochemistry, California State University, Long Beach, California 90840-9507, United States;* orcid.org/0000-0002-0640-0297
Robert S. Treß − *Lehrstuhl für Theoretische Chemie, Ruhr-Universität Bochum, 44801 Bochum, Germany*
Vamsee Voora − *Department of Chemical Sciences, Tata Institute of Fundamental Research, Mumbai 400005, India;* orcid.org/0000-0002-4887-0609
Artur Wodyński − *Institut für Chemie, Theoretische Chemie/Quantenchemie, Sekr. C7, Technische Universität Berlin, 10623 Berlin, Germany*
Jason M. Yu − *Department of Chemistry, University of California, Irvine, Irvine, California 92697-2025, United States;* orcid.org/0000-0002-2270-6798
Benedikt Zerulla − *Institute of Nanotechnology, Karlsruhe Institute of Technology (KIT), 76344 Eggenstein-Leopoldshafen, Germany;* orcid.org/0000-0002-8173-3761

Complete contact information is available at: https://pubs.acs.org/10.1021/acs.jctc.3c00347

Author Contributions

[‡]Y. J. Franzke and C. Holzer contributed equally to this work. Y. J. Franzke contributed to the conception and implementation of one-component current density ansätze for pNMR shifts, NMR couplings, EPR, and magnetizabilities as well as the two-component generalization for spin−orbit coupling (SCF, NMR, EPR, TDDFT). Further, Y. J. Franzke contributed to the conception and execution of research on relativistic EPR and NMR properties detailed in sections 3.4, 3.5, 3.6, and 3.7. This includes the implementation of integrals as well as the X2C/DLU-X2C response and picture-change routines. He designed the implementation of all relativistic EPR and (paramagnetic) NMR methods. Furthermore, the 2c damped response and static 2c CPKS framework were designed and implemented together with C. Holzer and M. Kehry. Y. J. Franzke contributed to the two-component DFT approach for periodic systems. He co-organized the collabo-

https://doi.org/10.1021/acs.jctc.3c00347
J. Chem. Theory Comput. 2023, 19, 6859−6890

ration for this paper and wrote and revised parts of the manuscript. C. Holzer contributed to the conception and implementation of the current density framework for one-component and two-component ansätze (finite magnetic field, SCF, NMR, EPR, and TDDFT). Additionally, C. Holzer implemented the initial graphics processing (GPU) unit support in the modules listed in Table 1. C. Holzer further contributed to the conception and implementation of the (2c) *GW*-BSE method in general and the related solvers. Furthermore, the 2c damped response and static 2c CPKS framework were designed and implemented together with Y. J. Franzke and M. Kehry. Additionally, the implementation and interfacing for the T-matrix based multiscale modeling of optical properties was codesigned by C. Holzer. He co-organized the collaboration for this paper and wrote and revised parts of the manuscript. Y. J. Franzke and C. Holzer have rewritten the local hybrid code from 2020−2022, i.e., increased efficiency, the just in time (JIT) framework, corrected memory handling, and so on. They implemented the general two-component version (Kramers-unrestricted LMFs and calibration function, XC kernel, and CDFT). T. Begušić and E. Tapavicza implemented the TGA method for vibronic spectra. F. Bruder added spin−orbit perturbation theory for EPR and pNMR using the X2C routines developed above. He wrote and revised parts of the manuscript. F. Della Sala implemented the HFACM approach and developed the TDDFT-as/TDDFT-ris methods. E. Fabiano developed and implemented the HFACM approach. S. Fürst carried out the implementation, optimization, and evaluation of range-separated local hybrid functionals, including the new ωLH22t functional. S. Gillhuber implemented the non-relativistic EPR and pNMR extension. Y. J. Franzke added the scalar X2C part. S. Gillhuber contributed to the research of section 3.7. He wrote and revised parts of the manuscript. R. Grotjahn performed investigations on the importance of the current-density correction in TDDFT and implemented the excited-state gradients and quadratic response properties for current-dependent MGGAs. Furthermore, R. Grotjahn contributed to the development of the ωLH22t functional. M. Kaupp supervised the work of S. Fürst and A. Wodyński as well as part of the work of R. Grotjahn and supported work on local hybrid functionals, including range-separated local hybrids, strong-correlation corrections, and aspects pertaining to current dependence. M. Kehry was involved in the design and programming steps of the underlying (2c) damped response modules for *GW*-BSE and 2c TDDFT. He wrote and revised parts of the manuscript. J. H. Andersen and D. A. Fedotov contributed to the development of the damped-response RI-CC2 functionalities. J. H. Andersen and C. Hättig carried out the illustrative damped RI-CC2 calculation here reported. C. Hättig and S. Coriani conceived, conceptualized, and supervised the damped-response RI-CC2 project and wrote the text in section 3.9.2. M. Krstić and B. Zerulla devised the multiscale modeling approach and designed and programmed the interface to external Maxwell-solver based programs. They wrote and revised parts of the manuscript. F. Mack contributed to the implementation of the NMR coupling constants (nonrelativistic and 2c) at the DFT and *GW*-BSE levels. S. Majumdar contributed to the research discussed in section 3.10 and was involved in conceptualization, execution, and writing. G. S. Phun contributed to writing section 3.10. A. Rajabi and D. Rappoport were involved in both the conceptualization and execution of the research discussed in section 3.8. S. M. Parker developed and supervised the TDDFT-ris method. F. Pauly and his group contributed to method development on periodic Hartree−Fock exchange and relativistic effects in periodic systems and the corresponding sections of this review. He wrote and revised parts of the manuscript. A. Pausch supported Y. J. Franzke and C. Holzer in the implementation of the two-component CDFT framework. A. Pausch and C. Holzer developed the methods for finite magnetic fields. He wrote and revised parts of the manuscript. E. Perlt performed implementations of the NEO methods and contributed to writing of section 4.1. T. Schrader performed NEO calculations and wrote section 4.1. M. Sharma, under the supervision of M. Sierka, contributed to the RT-TDDFT code and extended it to perform HHG simulations and also wrote the corresponding section 3.14. Additionally, M. Sharma implemented the molecular and periodic DFT-based embedding coupled with RT-TDDFT and wave function methods and wrote section 3.15.2. B. Samal and B. D. Nguyen contributed to writing section 3.12. V. K. Voora developed the AC version of the GKS-spRPA method and contributed to the writing of section 3.12. A. Wodyński carried out the implementation, optimization, and evaluation of strong-correlation-corrected local hybrid functionals. J. M. Yu contributed to the conception and execution of the research detailed in section 3.4. R. Treß developed the frozen density embedding implementation and carried out the calculation reported in section 3.15.1, and C. Hättig supervised the project. F. Furche conceived, oversaw, and participated in the development of the material in sections 3.8 and 3.10 and parts of the material in sections 3.2, 3.12, 3.4, and 4.1. He also initiated and organized the collaboration for this paper and wrote and revised parts of the manuscript. M. Sierka supervised the work of M. Sharma described in sections 3.14 and 3.15.2, as well as conceived, oversaw, and participated in the development of the RT-TDDFT code (section 3.14). He co-organized the collaboration for this paper and wrote and revised parts of the manuscript. F. Weigend supervised the work of F. Bruder, S. Gillhuber, and F. Mack and supported the EPR, pNMR shift, NMR coupling, and ring current studies. He co-organized the collaboration for this paper and wrote and revised parts of the manuscript.

Notes

The authors declare the following competing financial interest(s): Principal Investigator Filipp Furche has an equity interest in TURBOMOLE GmbH. The terms of this arrangement have been reviewed and approved by the University of California, Irvine, in accordance with its conflict of interest policies. Christof Hattig and David P. Tew have an equity interest in TURBOMOLE GmbH. Marek Sierka and Florian Weigend have an equity interest in TURBOMOLE GmbH and serve as its chief executive officers.

■ ACKNOWLEDGMENTS

All past and present developers' contributions to the TURBOMOLE project are gratefully acknowledged. A list of TURBOMOLE contributors is available on the TURBOMOLE website.[91] Y. J. Franzke was supported by fellowships from Fonds der Chemischen Industrie (FCI, German Chemical Industry Fonds), Deutscher Akademischer Austauschdienst (DAAD, German Academic Exchange Service), and TURBOMOLE GmbH. C. Holzer and M. Krstić gratefully acknowledge funding by Volkswagen Stiftung. T. Begušić and

https://doi.org/10.1021/acs.jctc.3c00347
J. Chem. Theory Comput. 2023, 19, 6859−6890

E. Tapavicza acknowledge scientific support from J. Vaníček in the development and application of the TGA method. F. Della Sala acknowledges the financial support from ICSC−Centro Nazionale di Ricerca in High Performance Computing, Big Data and Quantum Computing, funded by European Union−NextGenerationEU−PNRR. D. A. Fedotov and S. Coriani acknowledge support from the European Unions Horizon 2020 research and innovation program under the Marie Skłodowska-Curie European Training Network COSINE (grant agreement no. 765739). J. H. Andersen and S. Coriani acknowledge financial support from the Independent Research Fund Denmark-DFF-FNU RP2 (grant no. 7014-00258B). S. Gillhuber is supported by a fellowship from Fonds der Chemischen Industrie (FCI no. 110160). R. Grotjahn acknowledges support via a Walter-Benjamin postdoctoral fellowship funded by the Deutsche Forschungsgemeinschaft (DFG, German Research Foundation), no. 501114520. C. Hättig acknowledges support by the Deutsche Forschungsgemeneinschaft (DFG) via project Ha 2588/10-1. The Kaupp group has been supported by the Deutsche Forschungsgemeinschaft (DFG) via projects KA1187/14-1 and KA1187/14-2. M. Kehry acknowledges financial support by the DFG through the Transregional CRC 88 "Cooperative Effects in Homo- and Heterometallic Complexes" (project C1). F. Mack acknowledges support from TURBOMOLE GmbH and from the DFG through the CRC 1176 (Project Q5). The material in section 3.8 and parts of the material in section 3.12 is based upon work supported by the US National Science Foundation under CHE-2102568. The material in section 3.2 and in section 3.10 is based upon work supported by the US Department of Energy, Office of Basic Energy Sciences, under award number DE-SC0018352. A. Pausch was supported by a fellowship from Fonds der Chemischen Industrie and Studienstiftung des deutschen Volkes (German Academic Scholarship Foundation). E. Perlt and T. Schrader acknowledge support from the Carl Zeiss Foundation within the CZS Breakthroughs Program. M. Sierka and M. Sharma gratefully acknowledge financial support from Deutsche Forschungsgemeinschaft (DFG, German Research Foundation) within the CRC 1375 NOA, project A4, and from the Carl Zeiss Foundation within the CZS Breakthroughs Program. B. Samal and V. K. Voora were supported by the Department of Atomic Energy, Government of India, under project no. RTI2001. F. Weigend acknowledges support from the DFG through the Collaborative Research Centre (CRC) 1573 (Project Q). J.M. Yu acknowledges support from the US National Science Foundation under Grant DGE-1839285. B. Zerulla acknowledges support by the KIT through the "Virtual Materials Design" (VIRTMAT) project.

REFERENCES

(1) Ahlrichs, R.; Bär, M.; Häser, M.; Horn, H.; Kölmel, C. Electronic structure calculations on workstation computers: The program system TURBOMOLE. *Chem. Phys. Lett.* **1989**, *162*, 165−169.

(2) Häser, M.; Ahlrichs, R. Improvements on the direct SCF method. *J. Comput. Chem.* **1989**, *10*, 104−111.

(3) Häser, M.; Ahlrichs, R.; Baron, H. P.; Weis, P.; Horn, H. Direct computation of second-order SCF properties of large molecules on workstation computers with an application to large carbon clusters. *Theor. Chim. Acta* **1992**, *83*, 455−470.

(4) Haase, F.; Ahlrichs, R. Semidirect MP2 gradient evaluation on workstation computers: The MPGRAD program. *J. Comput. Chem.* **1993**, *14*, 907−912.

(5) Brode, S.; Horn, H.; Ehrig, M.; Moldrup, D.; Rice, J. E.; Ahlrichs, R. Parallel Direct SCF and Gradient Program For Workstation Clusters. *J. Comput. Chem.* **1993**, *14*, 1142−1148.

(6) Kollwitz, M.; Gauss, J. A direct implementation of the GIAO-MBPT(2) method for calculating NMR chemical shifts. Application to the naphthalenium and anthracenium ions. *Chem. Phys. Lett.* **1996**, *260*, 639−646.

(7) Kollwitz, M.; Häser, M.; Gauss, J. Non-Abelian point group symmetry in direct second-order many-body perturbation theory calculations of NMR chemical shifts. *J. Chem. Phys.* **1998**, *108*, 8295−8301.

(8) Weiss, H.; Ahlrichs, R.; Häser, M. A direct algorithm for self-consistent-field linear-response theory and application to C_{60}-excitation-energies, oscillator-strengths, and frequency-dependent polarizabilities. *J. Chem. Phys.* **1993**, *99*, 1262−1270.

(9) Treutler, O.; Ahlrichs, R. Efficient molecular numerical integration schemes. *J. Chem. Phys.* **1995**, *102*, 346−354.

(10) Bauernschmitt, R.; Ahlrichs, R. Treatment of electronic excitations within the adiabatic approximation of time dependent density functional theory. *Chem. Phys. Lett.* **1996**, *256*, 454−464.

(11) Furche, F.; Perdew, J. P. The performance of semi-local and hybrid density functionals in 3*d* transition metal chemistry. *J. Chem. Phys.* **2006**, *124*, 044103. also published in *Virtual J. Biol. Phys. Res.* **2006**, *11*.

(12) Furche, F. Molecular tests of the random phase approximation to the exchange-correlation energy functional. *Phys. Rev. B* **2001**, *64*, 195120.

(13) Bates, J. E.; Furche, F. Communication: Random phase approximation renormalized many-body perturbation theory. *J. Chem. Phys.* **2013**, *139*, 171103.

(14) Chen, G. P.; Voora, V. K.; Agee, M. M.; Balasubramani, S. G.; Furche, F. Random-phase approximation methods. *Annu. Rev. Phys. Chem.* **2017**, *68*, 421−445.

(15) Chen, G. P.; Agee, M. M.; Furche, F. Performance and scope of perturbative corrections to random-phase approximation energies. *J. Chem. Theory Comput.* **2018**, *14*, 5701−5714.

(16) Voora, V. K.; Balasubramani, S. G.; Furche, F. Variational generalized Kohn-Sham approach combining the random-phase-approximation and Green's-function methods. *Phys. Rev. A* **2019**, *99*, 012518.

(17) Bates, J. E.; Furche, F. Harnessing the meta-generalized gradient approximation for time-dependent density functional theory. *J. Chem. Phys.* **2012**, *137*, 164105.

(18) Plessow, P.; Weigend, F. Seminumerical calculation of the Hartree-Fock exchange matrix: Application to two-component procedures and efficient evaluation of local hybrid density functionals. *J. Comput. Chem.* **2012**, *33*, 810−816.

(19) Maier, T. M.; Bahmann, H.; Kaupp, M. Efficient Seminumerical Implementation of Global and Local Hybrid Functionals for Time-Dependent Density Functional Theory. *J. Chem. Theory Comput.* **2015**, *11*, 4226−4237.

(20) Furche, F.; Ahlrichs, R.; Wachsmann, C.; Weber, E.; Sobanski, A.; Vögtle, F.; Grimme, S. Circular dichroism of helicenes investigated by time-dependent density functional theory. *J. Am. Chem. Soc.* **2000**, *122*, 1717−1724.

(21) Furche, F.; Rappoport, D. Density functional methods for excited states: equilibrium structure and electronic spectra In *Computational Photochemistry*; Olivucci, M., Ed.; Computational and Theoretical Chemistry, Vol. *16*; Elsevier: Amsterdam, The Netherlands, 2005; pp 93−128.

(22) Kattannek, M. *Entwicklung und Implementierung optimierter Algorithmen für molekulare Hartree-Fock- und Dichtefunktional-Rechnungen*. Ph.D. Thesis, Universität Karlsruhe (TH), Karlsruhe, Germany, 2006.

(23) Eshuis, H.; Yarkony, J.; Furche, F. Fast computation of molecular random phase approximation correlation energies using resolution of the identity and imaginary frequency integration. *J. Chem. Phys.* **2010**, *132*, 234114.

https://doi.org/10.1021/acs.jctc.3c00347
J. Chem. Theory Comput. 2023, 19, 6859−6890

(24) Furche, F.; Krull, B. T.; Nguyen, B. D.; Kwon, J. Accelerating molecular property calculations with nonorthonormal Krylov space methods. *J. Chem. Phys.* **2016**, *144*, 174105.
(25) Deglmann, P.; Furche, F.; Ahlrichs, R. An efficient implementation of second analytical derivatives for density functional methods. *Chem. Phys. Lett.* **2002**, *362*, 511−518.
(26) Grimme, S.; Furche, F.; Ahlrichs, R. An improved method for density functional calculations of the frequency-dependent optical rotation. *Chem. Phys. Lett.* **2002**, *361*, 321−328.
(27) Deglmann, P.; May, K.; Furche, F.; Ahlrichs, R. Nuclear second analytical derivative calculations using auxiliary basis set expansions. *Chem. Phys. Lett.* **2004**, *384*, 103−107.
(28) Rappoport, D.; Furche, F. Analytical time-dependent density functional derivative methods within the RI-J approximation, an approach to excited states of large molecules. *J. Chem. Phys.* **2005**, *122*, 064105.
(29) Rappoport, D.; Furche, F. Lagrangian approach to molecular vibrational Raman intensities using time-dependent hybrid density functional theory. *J. Chem. Phys.* **2007**, *126*, 201104.
(30) Send, R.; Furche, F. First-order nonadiabatic couplings from time-dependent hybrid density functional response theory: Consistent formalism, implementation, and performance. *J. Chem. Phys.* **2010**, *132*, 044107.
(31) Burow, A. M.; Bates, J. E.; Furche, F.; Eshuis, H. Analytical first-order molecular properties and forces within the adiabatic connection random phase approximation. *J. Chem. Theory Comput.* **2014**, *10*, 180−194.
(32) Ou, Q.; Bellchambers, G. D.; Furche, F.; Subotnik, J. E. First-order derivative couplings between excited states from adiabatic TDDFT response theory. *J. Chem. Phys.* **2015**, *142*, 064114.
(33) Klawohn, S.; Bahmann, H.; Kaupp, M. Implementation of Molecular Gradients for Local Hybrid Density Functionals Using Seminumerical Integration Techniques. *J. Chem. Theory Comput.* **2016**, *12*, 4254−4262.
(34) Parker, S. M.; Rappoport, D.; Furche, F. Quadratic Response Properties from TDDFT: Trials and Tribulations. *J. Chem. Theory Comput.* **2018**, *14*, 807−819.
(35) Grotjahn, R.; Furche, F.; Kaupp, M. Development and Implementation of Excited-State Gradients for Local Hybrid Functionals. *J. Chem. Theory Comput.* **2019**, *15*, 5508−5522.
(36) Franzke, Y. J.; Weigend, F. NMR Shielding Tensors and Chemical Shifts in Scalar-Relativistic Local Exact Two-Component Theory. *J. Chem. Theory Comput.* **2019**, *15*, 1028−1043.
(37) Wodyński, A.; Kaupp, M. Density Functional Calculations of EPR g- and Hyperfine-Coupling Tensors Using the Exact Two-Component (X2C) Transformation and Efficient Approximations to the Two-Electron Spin-Orbit Terms. *J. Phys. Chem. A* **2019**, *123*, 5660−5672.
(38) Franzke, Y. J.; Yu, J. M. Hyperfine Coupling Constants in Local Exact Two-Component Theory. *J. Chem. Theory Comput.* **2022**, *18*, 323−343.
(39) Franzke, Y. J.; Yu, J. M. Quasi-Relativistic Calculation of EPR *g* Tensors with Derivatives of the Decoupling Transformation, Gauge-Including Atomic Orbitals, and Magnetic Balance. *J. Chem. Theory Comput.* **2022**, *18*, 2246−2266.
(40) Eichkorn, K.; Treutler, O.; Öhm, H.; Häser, M.; Ahlrichs, R. Auxiliary Basis Sets to Approximate Coulomb Potentials. *Chem. Phys. Lett.* **1995**, *240*, 283−290.
(41) Eichkorn, K.; Weigend, F.; Treutler, O.; Ahlrichs, R. Auxiliary basis sets for main row atoms and transition metals and their use to approximate Coulomb potentials. *Theor. Chem. Acc.* **1997**, *97*, 119−124.
(42) Weigend, F. A fully direct RI-HF algorithm: Implementation, optimized auxiliary basis sets, demonstration of accuracy and efficiency. *Phys. Chem. Chem. Phys.* **2002**, *4*, 4285−4291.
(43) Weigend, F. Hartree−Fock exchange fitting basis sets for H to Rn. *J. Comput. Chem.* **2008**, *29*, 167−175.
(44) Weigend, F.; Häser, M.; Patzelt, H.; Ahlrichs, R. RI-MP2: optimized auxiliary basis sets and demonstration of efficiency. *Chem. Phys. Lett.* **1998**, *294*, 143−152.
(45) Weigend, F.; Häser, M. RI-MP2: first derivatives and global consistency. *Theor. Chem. Acc.* **1997**, *97*, 331−340.
(46) Hättig, C.; Weigend, F. CC2 excitation energy calculations on large molecules using the resolution of the identity approximation. *J. Chem. Phys.* **2000**, *113*, 5154−5161.
(47) Sierka, M.; Hogekamp, A.; Ahlrichs, R. Fast evaluation of the Coulomb potential for electron densities using multipole accelerated resolution of identity approximation. *J. Chem. Phys.* **2003**, *118*, 9136−9148.
(48) Armbruster, M. K.; Weigend, F.; van Wüllen, C.; Klopper, W. Self-consistent treatment of spin-orbit interactions with efficient Hartree-Fock and density functional methods. *Phys. Chem. Chem. Phys.* **2008**, *10*, 1748−1756.
(49) Baldes, A.; Weigend, F. Efficient two-component self-consistent field procedures and gradients: implementation in TURBOMOLE and application to Au_{20}^{-}. *Mol. Phys.* **2013**, *111*, 2617−2624.
(50) Kühn, M. Correlation Energies from the Two-Component Random Phase Approximation. *J. Chem. Theory Comput.* **2014**, *10*, 623−633.
(51) Krause, K.; Klopper, W. Implementation of the Bethe-Salpeter equation in the TURBOMOLE program. *J. Comput. Chem.* **2017**, *38*, 383−388.
(52) Gui, X.; Holzer, C.; Klopper, W. Accuracy Assessment of GW Starting Points for Calculating Molecular Excitation Energies Using the Bethe-Salpeter Formalism. *J. Chem. Theory Comput.* **2018**, *14*, 2127−2136.
(53) Holzer, C.; Klopper, W. Ionized, electron-attached, and excited states of molecular systems with spin−orbit coupling: Two-component GW and Bethe−Salpeter implementations. *J. Chem. Phys.* **2019**, *150*, 204116.
(54) Kühn, M.; Weigend, F. Two-component hybrid time-dependent density functional theory within the Tamm-Dancoff approximation. *J. Chem. Phys.* **2015**, *142*, 034116.
(55) Burow, A. M.; Sierka, M.; Mohamed, F. Resolution of identity approximation for the Coulomb term in molecular and periodic systems. *J. Chem. Phys.* **2009**, *131*, 214101−1−214101−6.
(56) Łazarski, R.; Burow, A. M.; Sierka, M. Density functional theory for molecular and periodic systems using density fitting and continuous fast multipole methods. *J. Chem. Theory Comput.* **2015**, *11*, 3029−3041.
(57) Łazarski, R.; Burow, A. M.; Grajciar, L.; Sierka, M. Density functional theory for molecular and periodic systems using density fitting and continuous fast multipole method: Analytical gradients. *J. Comput. Chem.* **2016**, *37*, 2518−2526.
(58) Grajciar, L. Low-memory Iterative Density Fitting. *J. Comput. Chem.* **2015**, *36*, 1521−1535.
(59) Becker, M.; Sierka, M. Density functional theory for molecular and periodic systems using density fitting and continuous fast multipole method: Stress tensor. *J. Comput. Chem.* **2019**, *40*, 2563−2570.
(60) Mack, F.; Schattenberg, C. J.; Kaupp, M.; Weigend, F. Nuclear Spin−Spin Couplings: Efficient Evaluation of Exact Exchange and Extension to Local Hybrid Functionals. *J. Phys. Chem. A* **2020**, *124*, 8529−8539.
(61) Franzke, Y. J.; Holzer, C.; Mack, F. NMR Coupling Constants Based on the Bethe−Salpeter Equation in the *GW* Approximation. *J. Chem. Theory Comput.* **2022**, *18*, 1030−1045.
(62) Reiter, K.; Mack, F.; Weigend, F. Calculation of Magnetic Shielding Constants with meta-GGA Functionals Employing the Multipole-Accelerated Resolution of the Identity: Implementation and Assessment of Accuracy and Efficiency. *J. Chem. Theory Comput.* **2018**, *14*, 191−197.
(63) Gillhuber, S.; Franzke, Y. J.; Weigend, F. Paramagnetic NMR Shielding Tensors and Ring Currents: Efficient Implementation and Application to Heavy Element Compounds. *J. Phys. Chem. A* **2021**, *125*, 9707−9723.

https://doi.org/10.1021/acs.jctc.3c00347
J. Chem. Theory Comput. 2023, 19, 6859−6890

(64) Friese, D. H.; Hättig, C.; Ruud, K. Calculation of two-photon absorption strengths with the approximate coupled cluster singles and doubles model CC2 using the resolution-of-identity approximation. *Phys. Chem. Chem. Phys.* **2012**, *14*, 1175−1184.
(65) Friese, D. H.; Hättig, C.; Rizzo, A. Origin-independent two-photon circular dichroism calculations in coupled cluster theory. *Phys. Chem. Chem. Phys.* **2016**, *18*, 13683−13692.
(66) Winter, N. O. C.; Hättig, C. Scaled opposite-spin CC2 for ground and excited states with fourth order scaling computational costs. *J. Chem. Phys.* **2011**, *134*, 184101.
(67) Winter, N. O. C.; Hättig, C. Quartic scaling analytical gradients of scaled opposite-spin CC2. *Chem. Phys.* **2012**, *401*, 217−227.
(68) Hättig, C.; Tew, D. P.; Köhn, A. Communications: Accurate and efficient approximations to explicitly correlated coupled-cluster singles and doubles, CCSD-F12. *J. Chem. Phys.* **2010**, *132*, 231102.
(69) Tew, D. P. Explicitly correlated coupled-cluster theory with Brueckner orbitals. *J. Chem. Phys.* **2016**, *145*, 074103.
(70) Schmitz, G.; Hättig, C.; Tew, D. P. Explicitly Correlated PNO-MP2 and PNO-CCSD and their Application to the S66 Set and Large Molecular Systems. *Phys. Chem. Chem. Phys.* **2014**, *16*, 22167−22178.
(71) Schmitz, G.; Hättig, C. Perturbative triples correction for local pair natural orbital based explicitly correlated CCSD(F12*) using Laplace transformation techniques. *J. Chem. Phys.* **2016**, *145*, 234107.
(72) Frank, M. S.; Schmitz, G.; Hättig, C. The PNO−MP2 gradient and its application to molecular geometry optimizations. *Mol. Phys.* **2017**, *115*, 343−356.
(73) Schmitz, G.; Hättig, C. Accuracy of Explicitly Correlated Local PNO-CCSD(T). *J. Chem. Theory Comput.* **2017**, *13*, 2623−2633.
(74) Laricchia, S.; Fabiano, E.; Della Sala, F. Frozen density embedding with hybrid functionals. *J. Chem. Phys.* **2010**, *133*, 164111.
(75) Bachorz, R. A.; Bischoff, F. A.; Glöß, A.; Hättig, C.; Höfener, S.; Klopper, W.; Tew, D. P. The MP2-F12 method in the TURBOMOLE program package. *J. Comput. Chem.* **2011**, *32*, 2492−2513.
(76) Schwabe, T.; Sneskov, K.; Haugaard Olsen, J. M.; Kongsted, J.; Christiansen, O.; Hättig, C. PERI-CC2: A Polarizable Embedded RI-CC2 Method. *J. Chem. Theory Comput.* **2012**, *8*, 3274−3283.
(77) Höfener, S. Coupled-cluster frozen-density embedding using resolution of the identity methods. *J. Comput. Chem.* **2014**, *35*, 1716−1724.
(78) Klamt, A.; Diedenhofen, M. Calculation of Solvation Free Energies with DCOSMO-RS. *J. Phys. Chem. A* **2015**, *119*, 5439−5445.
(79) Hršak, D.; Marefat Khah, A.; Christiansen, O.; Hättig, C. Polarizable Embedded RI-CC2 Method for Two-Photon Absorption Calculations. *J. Chem. Theory Comput.* **2015**, *11*, 3669−3678.
(80) Reinholdt, P.; Nørby, M. S.; Kongsted, J. Modeling of Magnetic Circular Dichroism and UV/Vis Absorption Spectra Using Fluctuating Charges or Polarizable Embedding within a Resonant-Convergent Response Theory Formalism. *J. Chem. Theory Comput.* **2018**, *14*, 6391−6404.
(81) Marefat Khah, A.; Karbalaei Khani, S.; Hättig, C. Analytic Excited State Gradients for the QM/MM Polarizable Embedded Second-Order Algebraic Diagrammatic Construction for the Polarization Propagator PE-ADC(2). *J. Chem. Theory Comput.* **2018**, *14*, 4640−4650.
(82) Sharma, M.; Sierka, M. Efficient Implementation of Density Functional Theory Based Embedding for Molecular and Periodic Systems Using Gaussian Basis Functions. *J. Chem. Theory Comput.* **2022**, *18*, 6892−6904.
(83) Treß, R. S.; Hättig, C.; Höfener, S. Employing Pseudopotentials to Tackle Excited-State Electron Spill-Out in Frozen Density Embedding Calculations. *J. Chem. Theory Comput.* **2022**, *18*, 1737−1747.
(84) Peng, D.; Middendorf, N.; Weigend, F.; Reiher, M. An efficient implementation of two-component relativistic exact-decoupling methods for large molecules. *J. Chem. Phys.* **2013**, *138*, 184105.
(85) Franzke, Y. J.; Middendorf, N.; Weigend, F. Efficient implementation of one- and two-component analytical energy gradients in exact two-component theory. *J. Chem. Phys.* **2018**, *148*, 104110.
(86) Franzke, Y. J.; Mack, F.; Weigend, F. NMR Indirect Spin-Spin Coupling Constants in a Modern Quasirelativistic Density Functional Framework. *J. Chem. Theory Comput.* **2021**, *17*, 3974−3994.
(87) van Setten, M. J.; Weigend, F.; Evers, F. The GW-Method for Quantum Chemistry Applications: Theory and Implementation. *J. Chem. Theory Comput.* **2013**, *9*, 232−246.
(88) Kaplan, F.; Harding, M. E.; Seiler, C.; Weigend, F.; Evers, F.; van Setten, M. J. Quasi-Particle Self-Consistent GW for Molecules. *J. Chem. Theory Comput.* **2016**, *12*, 2528−2541.
(89) Müller, C.; Sharma, M.; Sierka, M. Real-time time-dependent density functional theory using density fitting and the continuous fast multipole method. *J. Comput. Chem.* **2020**, *41*, 2573−2582.
(90) Tapavicza, E.; Bellchambers, G.; Vincent, J. C.; Furche, F. *Ab initio* non-adiabatic dynamics. *Phys. Chem. Chem. Phys.* **2013**, *15*, 18336−18348.
(91) *TURBOMOLE*. https://www.turbomole.org (accessed 2022-12-01).
(92) Balasubramani, S. G.; Chen, G. P.; Coriani, S.; Diedenhofen, M.; Frank, M. S.; Franzke, Y. J.; Furche, F.; Grotjahn, R.; Harding, M. E.; Hättig, C.; Hellweg, A.; Helmich-Paris, B.; Holzer, C.; Huniar, U.; Kaupp, M.; Marefat Khah, A.; Karbalaei Khani, S.; Müller, T.; Mack, F.; Nguyen, B. D.; Parker, S. M.; Perlt, E.; Rappoport, D.; Reiter, K.; Roy, S.; Rückert, M.; Schmitz, G.; Sierka, M.; Tapavicza, E.; Tew, D. P.; van Wüllen, C.; Voora, V. K.; Weigend, F.; Wodyński, A.; Yu, J. M. TURBOMOLE: Modular program suite for *ab initio* quantum-chemical and condensed-matter simulations. *J. Chem. Phys.* **2020**, *152*, 184107.
(93) Furche, F.; Ahlrichs, R.; Hättig, C.; Klopper, W.; Sierka, M.; Weigend, F. Turbomole. *WIREs Comput. Mol. Sci.* **2014**, *4*, 91−100.
(94) van Wüllen, C. Shared-memory parallelization of the TURBOMOLE programs AOFORCE, ESCF, and EGRAD: How to quickly parallelize legacy code. *J. Comput. Chem.* **2011**, *32*, 1195−1201.
(95) Bachorz, R. A.; Bischoff, F. A.; Glöß, A.; Hättig, C.; Höfener, S.; Klopper, W.; Tew, D. P. The MP2-F12 Method in the TURBOMOLE Program Package. *J. Comput. Chem.* **2011**, *32*, 2492−2513.
(96) Almaraz, E. P.; Furche, F. Initial OpenMP version of aoforce and escf, released with TURBOMOLE V6.3; TURBOMOLE GmbH: Karlsruhe, Germany, 2011.
(97) Holzer, C.; Franzke, Y. J. OpenMP version of ridft, rdgrad, and egrad with contributions to mpshift, dscf, and grad; improved OpenMP version of aoforce and escf, released with TURBOMOLE V7.4 and further improved in TURBOMOLE V7.5; TURBOMOLE GmbH: Karlsruhe, Germany, 2020.
(98) Hättig, C.; Hellweg, A.; Köhn, A. Distributed memory parallel implementation of energies and gradients for second-order Møller-Plesset perturbation theory with the resolution-of-the-identity approximation. *Phys. Chem. Chem. Phys.* **2006**, *8*, 1159−1169.
(99) Müller, T. Global Array toolkit based distributed shared memory version of ridft and rdgrad, released with TURBOMOLE V6.0; TURBOMOLE GmbH: Karlsruhe, Germany, 2011.
(100) Müller, T. Parallel DFT in Turbomole, Linear Algebra. In *High Performance Computing in Chemistry*; Grotendorst, J., Ed.; NIC Series, Vol. *25*; John von Neumann Institute for Computing: Jülich, Germany, 2005; pp 83−107.
(101) Müller, T. MPI based version of ridft and rdgrad with native distributed shared memory support, released with TURBOMOLE V7.2; TURBOMOLE GmbH: Karlsruhe, Germany, 2017.
(102) van Wüllen, C. Hybrid OpenMP/MPI parallelization of dscf, grad, and aoforce, released with TURBOMOLE V7.2; TURBOMOLE GmbH: Karlsruhe, Germany, 2017.
(103) Plessow, P. Reaction Path Optimization without NEB Springs or Interpolation Algorithms. *J. Chem. Theory Comput.* **2013**, *9*, 1305−1310.
(104) Reiter, K.; Kühn, M.; Weigend, F. Vibrational circular dichroism spectra for large molecules and molecules with heavy elements. *J. Chem. Phys.* **2017**, *146*, 054102.

https://doi.org/10.1021/acs.jctc.3c00347
J. Chem. Theory Comput. 2023, 19, 6859−6890

(105) Sierka, M.; Döbler, J.; Sauer, J.; Santambrogio, G.; Brümmer, M.; Wöste, L.; Janssens, E.; Meijer, G.; Asmis, K. Unexpected Structures of Aluminum Oxide Clusters in the Gas Phase. *Angew. Chem., Int. Ed.* **2007**, *46*, 3372−3375.
(106) Steffen, C.; Thomas, K.; Huniar, U.; Hellweg, A.; Rubner, O.; Schroer, A. TmoleX − A graphical user interface for TURBOMOLE. *J. Comput. Chem.* **2010**, *31*, 2967−2970.
(107) *OpenMP*. https://www.openmp.org (accessed 2022-12-05).
(108) MPI Forum. https://www.mpi-forum.org (accessed 2022-12-05).
(109) Holzer, C. An improved seminumerical Coulomb and exchange algorithm for properties and excited states in modern density functional theory. *J. Chem. Phys.* **2020**, *153*, 184115.
(110) Maier, T. M.; Arbuznikov, A. V.; Kaupp, M. Local hybrid functionals: Theory, implementation, and performance of an emerging new tool in quantum chemistry and beyond. *WIREs Comput. Mol. Sci.* **2019**, *9*, e1378.
(111) Janesko, B. G. Replacing hybrid density functional theory: motivation and recent advances. *Chem. Soc. Rev.* **2021**, *50*, 8470−8495.
(112) Bahmann, H.; Kaupp, M. Efficient Self-Consistent Implementation of Local Hybrid Functionals. *J. Chem. Theory Comput.* **2015**, *11*, 1540−1548.
(113) Kehry, M.; Franzke, Y. J.; Holzer, C.; Klopper, W. Quasirelativistic two-component core excitations and polarisabilities from a damped-response formulation of the Bethe-Salpeter equation. *Mol. Phys.* **2020**, *118*, e1755064.
(114) Grotjahn, R.; Lauter, G. J.; Haasler, M.; Kaupp, M. Evaluation of Local Hybrid Functionals for Electric Properties: Dipole Moments and Static and Dynamic Polarizabilities. *J. Phys. Chem. A* **2020**, *124*, 8346−8358.
(115) Schattenberg, C. J.; Reiter, K.; Weigend, F.; Kaupp, M. An Efficient Coupled-Perturbed Kohn-Sham Implementation of NMR Chemical Shift Computations with Local Hybrid Functionals and Gauge-Including Atomic Orbitals. *J. Chem. Theory Comput.* **2020**, *16*, 931−943.
(116) Wodyński, A.; Kaupp, M. Noncollinear Relativistic Two-Component X2C Calculations of Hyperfine Couplings Using Local Hybrid Functionals. Importance of the High-Density Coordinate Scaling Limit. *J. Chem. Theory Comput.* **2020**, *16*, 314−325.
(117) Holzer, C.; Franzke, Y. J. A Local Hybrid Exchange Functional Approximation from First Principles. *J. Chem. Phys.* **2022**, *157*, 034108.
(118) Franzke, Y. J.; Holzer, C. Impact of the current density on paramagnetic NMR properties. *J. Chem. Phys.* **2022**, *157*, 031102.
(119) Holzer, C.; Franzke, Y. J.; Kehry, M. Assessing the Accuracy of Local Hybrid Density Functional Approximations for Molecular Response Properties. *J. Chem. Theory Comput.* **2021**, *17*, 2928−2947.
(120) Haasler, M.; Maier, T. M.; Grotjahn, R.; Gückel, S.; Arbuznikov, A. V.; Kaupp, M. A Local Hybrid Functional with Wide Applicability and Good Balance between (De)Localization and Left−Right Correlation. *J. Chem. Theory Comput.* **2020**, *16*, 5645−5657.
(121) Harrison, D. P.; Grotjahn, R.; Naher, M.; Ghazvini, S. M. B. H.; Mazzucato, D. M.; Korb, M.; Moggach, S. A.; Lambert, C.; Kaupp, M.; Low, P. J. Quantum Interference in Mixed-Valence Complexes: Tuning Electronic Coupling Through Substituent Effects. *Angew. Chem., Int. Ed.* **2022**, *61*, e202211000.
(122) Gückel, S.; Safari, P.; Bagher Hosseini Ghazvini, S. M.; Hall, M. R.; Gluyas, J. B. G.; Kaupp, M.; Low, P. J. Iron Versus Ruthenium: Evidence for the Distinct Differences in the Electronic Structures of Hexa-1,3,5-triyn-1,6-diyl-bridged Complexes $[Cp^*(dppe)\{M\}\{\mu\text{-}(C{\equiv}C)_3\}\{M(dppe)Cp^*\}]^+$ (M = Fe, Ru). *Organometallics* **2021**, *40*, 346−357.
(123) Grotjahn, R.; Kaupp, M. Reliable TDDFT Protocol Based on a Local Hybrid Functional for the Prediction of Vibronic Phosphorescence Spectra Applied to Tris(2,2′-bipyridine)-Metal Complexes. *J. Phys. Chem. A* **2021**, *125*, 7099−7110.
(124) Grotjahn, R.; Kaupp, M. Validation of Local Hybrid Functionals for Excited States: Structures, Fluorescence, Phosphorescence, and Vibronic Spectra. *J. Chem. Theory Comput.* **2020**, *16*, 5821−5834.
(125) Grotjahn, R.; Kaupp, M. Assessment of hybrid functionals for singlet and triplet excitations: Why do some local hybrid functionals perform so well for triplet excitation energies? *J. Chem. Phys.* **2021**, *155*, 124108.
(126) Grotjahn, R.; Kaupp, M. A Look at Real-World Transition-Metal Thermochemistry and Kinetics with Local Hybrid Functionals. *Isr. J. Chem.* **2022**, e202200021.
(127) Schattenberg, C. J.; Kaupp, M. Extended Benchmark Set of Main-Group Nuclear Shielding Constants and NMR Chemical Shifts and Its Use to Evaluate Modern DFT Methods. *J. Chem. Theory Comput.* **2021**, *17*, 7602−7621.
(128) Schattenberg, C. J.; Lehmann, M.; Bühl, M.; Kaupp, M. Systematic Evaluation of Modern Density Functional Methods for the Computation of NMR Shifts of 3d Transition-Metal Nuclei. *J. Chem. Theory Comput.* **2022**, *18*, 273−292.
(129) Mori-Sánchez, P.; Cohen, A. J. The derivative discontinuity of the exchange−correlation functional. *Phys. Chem. Chem. Phys.* **2014**, *16*, 14378−14387.
(130) Janesko, B. G.; Proynov, E.; Kong, J.; Scalmani, G.; Frisch, M. J. Practical Density Functionals beyond the Overdelocalization−Underbinding Zero-Sum Game. *J. Phys. Chem. Lett.* **2017**, *8*, 4314−4318.
(131) Mori-Sánchez, P.; Cohen, A. J.; Yang, W. Discontinuous Nature of the Exchange-Correlation Functional in Strongly Correlated Systems. *Phys. Rev. Lett.* **2009**, *102*, 066403.
(132) Becke, A. D. Density functionals for static, dynamical, and strong correlation. *J. Chem. Phys.* **2013**, *138*, 074109.
(133) Kong, J.; Proynov, E. Density Functional Model for Nondynamic and Strong Correlation. *J. Chem. Theory Comput.* **2016**, *12*, 133−143.
(134) Wodyński, A.; Arbuznikov, A. V.; Kaupp, M. Local hybrid functionals augmented by a strong-correlation model. *J. Chem. Phys.* **2021**, *155*, 144101.
(135) Wodyński, A.; Kaupp, M. Local Hybrid Functional Applicable to Weakly and Strongly Correlated Systems. *J. Chem. Theory Comput.* **2022**, *18*, 6111−6123.
(136) Haunschild, R.; Scuseria, G. E. Range-separated local hybrids. *J. Chem. Phys.* **2010**, *132*, 224106.
(137) Janesko, B. G.; Krukau, A. V.; Scuseria, G. E. Self-consistent generalized Kohn-Sham local hybrid functionals of screened exchange: Combining local and range-separated hybridization. *J. Chem. Phys.* **2008**, *129*, 124110.
(138) Klawohn, S.; Bahmann, H. Self-Consistent Implementation of Hybrid Functionals with Local Range Separation. *J. Chem. Theory Comput.* **2020**, *16*, 953−963.
(139) Fürst, S.; Haasler, M.; Grotjahn, R.; Kaupp, M. Full Implementation, Optimization, and Evaluation of a Range-Separated Local Hybrid Functional with Wide Accuracy for Ground and Excited States. *J. Chem. Theory Comput.* **2023**, *19*, 488−502.
(140) Fürst, S.; Kaupp, M. Accurate Ionization Potentials, Electron Affinities, and Band Gaps from the ωLH22t Range-Separated Local Hybrid Functional: No Tuning Required. *J. Chem. Theory Comput.* **2023**, *19* (11), 3146−3158.
(141) Dobson, J. F. Alternative expressions for the Fermi hole curvature. *J. Chem. Phys.* **1993**, *98*, 8870−8872.
(142) Becke, A. D. Current density in exchange-correlation functionals: Application to atomic states. *J. Chem. Phys.* **2002**, *117*, 6935−6938.
(143) Tao, J. Explicit inclusion of paramagnetic current density in the exchange-correlation functionals of current-density functional theory. *Phys. Rev. B* **2005**, *71*, 205107.
(144) Bates, J. E.; Heiche, M. C.; Liang, J.; Furche, F. Erratum: "Harnessing the meta-generalized gradient approximation for time-dependent density functional theory" [J. Chem. Phys. 137, 164105 (2012)]. *J. Chem. Phys.* **2022**, *156*, 159902.

https://doi.org/10.1021/acs.jctc.3c00347
J. Chem. Theory Comput. 2023, 19, 6859−6890

(145) Grotjahn, R.; Furche, F.; Kaupp, M. Importance of imposing gauge invariance in time-dependent density functional theory calculations with meta-generalized gradient approximations. *J. Chem. Phys.* **2022**, *157*, 111102.
(146) Sciortino, G.; Lihi, N.; Czine, T.; Maréchal, J.-D.; Lledós, A.; Garribba, E. Accurate prediction of vertical electronic transitions of Ni(II) coordination compounds via time dependent density functional theory. *Int. J. Quantum Chem.* **2018**, *118*, e25655.
(147) Grotjahn, R.; Furche, F. Gauge-Invariant Excited-State Linear and Quadratic Response Properties within the Meta-Generalized Gradient Approximation. *J. Chem. Theory Comput.* **2023**, DOI: 10.1021/acs.jctc.3c00259.
(148) Schattenberg, C. J.; Kaupp, M. Effect of the current dependence of tau-dependent exchange-correlation functionals on nuclear shielding calculations. *J. Chem. Theory Comput.* **2021**, *17*, 1469−1479.
(149) Bruder, F.; Franzke, Y. J.; Weigend, F. Paramagnetic NMR Shielding Tensors Based on Scalar Exact Two-Component and Spin-Orbit Perturbation Theory. *J. Phys. Chem. A* **2022**, *126*, 5050−5069.
(150) Maximoff, S. N.; Scuseria, G. E. Nuclear magnetic resonance shielding tensors calculated with kinetic energy density-dependent exchange-correlation functionals. *Chem. Phys. Lett.* **2004**, *390*, 408−412.
(151) Holzer, C.; Franzke, Y. J.; Pausch, A. Current density functional framework for spin−orbit coupling. *J. Chem. Phys.* **2022**, *157*, 204102.
(152) Pausch, A.; Holzer, C. Linear Response of Current-Dependent Density Functional Approximations in Magnetic Fields. J. Phys. *Chem. Lett.* **2022**, *13*, 4335−4341.
(153) Helgaker, T.; Jaszuński, M.; Ruud, K. Ab initio methods for the calculation of NMR shielding and indirect spin-spin coupling constants. *Chem. Rev.* **1999**, *99*, 293−352.
(154) Vaara, J. Theory and computation of nuclear magnetic resonance parameters. *Phys. Chem. Chem. Phys.* **2007**, *9*, 5399−5148.
(155) Kjærgaard, T.; Coriani, S.; Ruud, K. Ab initio calculation of magnetic circular dichroism. *WIREs Comput. Mol. Sci.* **2012**, *2*, 443−455.
(156) Tellgren, E. I.; Soncini, A.; Helgaker, T. Nonperturbative ab initio calculations in strong magnetic fields using London orbitals. *J. Chem. Phys.* **2008**, *129*, 154114.
(157) Stopkowicz, S.; Gauss, J.; Lange, K. K.; Tellgren, E. I.; Helgaker, T. Coupled-cluster theory for atoms and molecules in strong magnetic fields. *J. Chem. Phys.* **2015**, *143*, 074110.
(158) Irons, T. J. P.; Zemen, J.; Teale, A. M. Efficient Calculation of Molecular Integrals over London Atomic Orbitals. *J. Chem. Theory Comput.* **2017**, *13*, 3636−3649.
(159) Sun, S.; Williams-Young, D. B.; Stetina, T. F.; Li, X. Generalized Hartree-Fock with Nonperturbative Treatment of Strong Magnetic Fields: Application to Molecular Spin Phase Transitions. *J. Chem. Theory Comput.* **2019**, *15*, 348−356.
(160) Pausch, A.; Gebele, M.; Klopper, W. Molecular point groups and symmetry in external magnetic fields. *J. Chem. Phys.* **2021**, *155*, 201101.
(161) David, G.; Irons, T. J. P.; Fouda, A. E. A.; Furness, J. W.; Teale, A. M. Self-Consistent Field Methods for Excited States in Strong Magnetic Fields: a Comparison between Energy- and Variance-Based Approaches. *J. Chem. Theory Comput.* **2021**, *17*, 5492−5508.
(162) Stetina, T. F.; Sun, S.; Williams-Young, D. B.; Li, X. Modeling Magneto-Photoabsorption Using Time-Dependent Complex Generalized Hartree-Fock. *ChemPhotoChem.* **2019**, *3*, 739−746.
(163) Monzel, L.; Pausch, A.; Peters, L. D. M.; Tellgren, E. I.; Helgaker, T.; Klopper, W. Molecular Dynamics of Linear Molecules in Strong Magnetic Fields. *J. Chem. Phys.* **2022**, *157*, 054106.
(164) Ferrario, L.; de Martino, D.; Gänsicke, B. T. Magnetic white dwarfs. *Space Sci. Rev.* **2015**, *191*, 111−169.
(165) Mereghetti, S.; Pons, J. A.; Melatos, A. Magnetars: properties, origin and evolution. *Space Sci. Rev.* **2015**, *191*, 315−338.
(166) Liebert, J.; Ferrario, L.; Wickramasinghe, D. T.; Smith, P. S. Enigmas from the Sloan Digital Sky Survey DR7 Kleinman White Dwarf Catalog. *Astrophys. J.* **2015**, *804*, 93.
(167) Ferrario, L.; Wickramasinghe, D.; Kawka, A. Magnetic fields in isolated and interacting white dwarfs. *Adv. Space Res.* **2020**, *66*, 1025−1056.
(168) Stopkowicz, S. Perspective: Coupled cluster theory for atoms and molecules in strong magnetic fields. *Int. J. Quantum Chem.* **2018**, *118*, e25391.
(169) Hall, P. B.; Maxwell, A. J. C2 in Peculiar DQ White Dwarfs. *Astrophys. J.* **2008**, *678*, 1292.
(170) Kowalski, P. M. The origin of peculiar molecular bands in cool DQ white dwarfs. *Astron. Astrophys.* **2010**, *519*, L8.
(171) Berdyugina, S. V.; Berdyugin, A. V.; Piirola, V. Molecular Magnetic Dichroism in Spectra of White Dwarfs. *Phys. Rev. Lett.* **2007**, *99*, 091101.
(172) Vornanen, T.; Berdyugina, S. V.; Berdyugin, A. V.; Piirola, V. GJ 841B—The Second DQ White Dwarf With Polarized CH Molecular Bands. *Astrophys. J.* **2010**, *720*, L52−L55.
(173) Lange, K. K.; Tellgren, E. I.; Hoffmann, M.; Helgaker, T. A paramagnetic bonding mechanism for diatomics in strong magnetic fields. *Science* **2012**, *337*, 327−331.
(174) Tellgren, E. I.; Fliegl, H. Non-perturbative treatment of molecules in linear magnetic fields: Calculation of anapole susceptibilities. *J. Chem. Phys.* **2013**, *139*, 164118.
(175) Pausch, A.; Klopper, W. Efficient evaluation of three-centre two-electron integrals over London orbitals. *Mol. Phys.* **2020**, *118*, e1736675.
(176) Pausch, A.; Holzer, C.; Klopper, W. Efficient Calculation of Magnetic Circular Dichroism Spectra Using Spin-Noncollinear Linear-Response Time-Dependent Density Functional Theory in Finite Magnetic Fields. *J. Chem. Theory Comput.* **2022**, *18*, 3747−3758.
(177) Holzer, C.; Teale, A. M.; Hampe, F.; Stopkowicz, S.; Helgaker, T.; Klopper, W. GW quasiparticle energies of atoms in strong magnetic fields. *J. Chem. Phys.* **2019**, *150*, 214112.
(178) Holzer, C.; Pausch, A.; Klopper, W. The GW/BSE Method in Magnetic Fields. *Front. Chem.* **2021**, *9*, No. 746162.
(179) Holzer, C. Practical Post-Kohn−Sham Methods for Time-Reversal Symmetry Breaking References. *J. Chem. Theory Comput.* **2023**, *9* (11), 3131−3145.
(180) Kobayashi, N.; Nakai, K. Applications of magnetic circular dichroism spectroscopy to porphyrins and phthalocyanines. *Chem. Commun.* **2007**, 4077−4092.
(181) Kundu, K.; White, J. R. K.; Moehring, S. A.; Yu, J. M.; Ziller, J. W.; Furche, F.; Evans, W. J.; Hill, S. A 9.2-GHz clock transition in a Lu(II) molecular spin qubit arising from a 3,467-MHz hyperfine interaction. *Nat. Chem.* **2022**, *14*, 392−397.
(182) Ishikawa, N.; Sugita, M.; Wernsdorfer, W. Quantum Tunneling of Magnetization in Lanthanide Single-Molecule Magnets: Bis(phthalocyaninato)terbium and Bis(phthalocyaninato)dysprosium Anions. *Angew. Chem., Int. Ed.* **2005**, *44*, 2931−2935.
(183) Franzke, Y. J. Reducing Exact Two-Component Theory for NMR Couplings to a One-Component Approach: Efficiency and Accuracy. *J. Chem. Theory Comput.* **2023**, *19*, 2010−2028.
(184) Mitchell, T. N.; Kowall, B. Karplus-type dihedral angle dependence for the coupling constants $^{3}J(^{119}Sn–C–C–^{119}Sn)$ and $^{3}J(^{119}Sn–C–C–^{29}Si)$. *Magn. Reson. Chem.* **1995**, *33*, 325−328.
(185) Krätschmer, F.; Sun, X.; Gillhuber, S.; Kucher, H.; Franzke, Y. J.; Weigend, F.; Roesky, P. Fully tin coated coinage metal ions: A pincer type bis-stannylene ligand for exclusive tetrahedral complexation. *Chem. Eur. J.* **2023**, *29*, e202203583.
(186) Peters, B.; Stuhrmann, G.; Mack, F.; Weigend, F.; Dehnen, S. Highly Soluble Supertetrahedra upon Selective Partial Butylation of Chalcogenido Metalate Clusters in Ionic Liquids. *Angew. Chem., Int. Ed.* **2021**, *60*, 17622−17628.
(187) Balmer, M.; Franzke, Y. J.; Weigend, F.; von Hänisch, C. Low valent group 14 phosphinidenide complexes $[(SIDippP)_2M]$ exhibit

P-M pπ-pπ interaction (M = Ge, Sn, Pb). *Chem. Eur. J.* **2020**, *26*, 192−197.
(188) Huniar, U. *Berechnung der chemischen Verschiebung der NMR mit Methoden der Dichtefunktionaltheorie (DFT)* Diploma Thesis, University of Karlsruhe (TH), Karlsruhe, Germany, 1999.
(189) Novotný, J.; Sojka, M.; Komorovsky, S.; Nečas, M.; Marek, R. Interpreting the Paramagnetic NMR Spectra of Potential Ru(III) Metallodrugs: Synergy between Experiment and Relativistic DFT Calculations. *J. Am. Chem. Soc.* **2016**, *138*, 8432−8445.
(190) Jensen, F. The Basis Set Convergence of Spin−Spin Coupling Constants Calculated by Density Functional Methods. *J. Chem. Theory Comput.* **2006**, *2*, 1360−1369.
(191) Jensen, F. Basis Set Convergence of Nuclear Magnetic Shielding Constants Calculated by Density Functional Methods. *J. Chem. Theory Comput.* **2008**, *4*, 719−727.
(192) Jakobsen, P.; Jensen, F. Probing basis set requirements for calculating hyperfine coupling constants. *J. Chem. Phys.* **2019**, *151*, 174107.
(193) Franzke, Y. J.; Treß, R.; Pazdera, T. M.; Weigend, F. Error-consistent segmented contracted all-electron relativistic basis sets of double- and triple-zeta quality for NMR shielding constants. *Phys. Chem. Chem. Phys.* **2019**, *21*, 16658−16664.
(194) Franzke, Y. J.; Spiske, L.; Pollak, P.; Weigend, F. Segmented Contracted Error-Consistent Basis Sets of Quadruple-ζ Valence Quality for One- and Two-Component Relativistic All-Electron Calculations. *J. Chem. Theory Comput.* **2020**, *16*, 5658−5674.
(195) Sundholm, D.; Fliegl, H.; Berger, R. J. F. Calculations of magnetically induced current densities: Theory and applications. *WIREs Comput. Mol. Sci.* **2016**, *6*, 639−678.
(196) von Ragué Schleyer, P.; Maerker, C.; Dransfeld, A.; Jiao, H.; van Eikema Hommes, N. J. R. Nucleus-independent chemical shifts: A simple and efficient aromaticity probe. *J. Am. Chem. Soc.* **1996**, *118*, 6317−6318.
(197) *GIMIC*, ver. 2.1.4 (merge 4bce2c9). GitHub, 2022. https://github.com/qmcurrents/gimic (accessed 2022-11-23).
(198) Jusélius, J.; Sundholm, D.; Gauss, J. Calculation of current densities using gauge-including atomic orbitals. *J. Chem. Phys.* **2004**, *121*, 3952−3963.
(199) Taubert, S.; Sundholm, D.; Jusélius, J. Calculation of spin-current densities using gauge-including atomic orbitals. *J. Chem. Phys.* **2011**, *134*, 054123.
(200) Sundholm, D.; Dimitrova, M.; Berger, R. J. F. Current density and molecular magnetic properties. *Chem. Commun.* **2021**, *57*, 12362−12378.
(201) Franzke, Y. J.; Sundholm, D.; Weigend, F. Calculations of current densities and aromatic pathways in cyclic porphyrin and isoporphyrin arrays. *Phys. Chem. Chem. Phys.* **2017**, *19*, 12794−12803.
(202) Reiter, K.; Weigend, F.; Wirz, L. N.; Dimitrova, M.; Sundholm, D. Magnetically Induced Current Densities in Toroidal Carbon Nanotubes. *J. Phys. Chem. C* **2019**, *123*, 15354−15365.
(203) Eulenstein, A. R.; Franzke, Y. J.; Bügel, P.; Massa, W.; Weigend, F.; Dehnen, S. Stabilizing a metalloid $\{Zn_{12}\}$ unit within a polymetallide environment in $[K_2Zn_{20}Bi_{16}]^{6-}$. *Nat. Commun.* **2020**, *11*, 5122.
(204) Mahmood, A.; Dimitrova, M.; Wirz, L. N.; Sundholm, D. Magnetically Induced Current Densities in π-Conjugated Porphyrin Nanoballs. *J. Phys. Chem. A* **2022**, *126*, 7864−7873.
(205) Eulenstein, A. R.; Franzke, Y. J.; Lichtenberger, N.; Wilson, R. J.; Deubner, H. L.; Kraus, F.; Clérac, R.; Weigend, F.; Dehnen, S. Substantial π-aromaticity of the anionic heavy-metal cluster $[Th@Bi_{12}]^{4-}$. *Nat. Chem.* **2021**, *13*, 149−155.
(206) Lichtenberger, N.; Wilson, R. J.; Eulenstein, A. R.; Massa, W.; Clérac, R.; Weigend, F.; Dehnen, S. Main Group Metal−Actinide Magnetic Coupling and Structural Response Upon U^{4+} Inclusion Into Bi, Tl/Bi, or Pb/Bi Cages. *J. Am. Chem. Soc.* **2016**, *138*, 9033−9036.
(207) Peerless, B.; Schmidt, A.; Franzke, Y. J.; Dehnen, S. φ-Aromaticity in prismatic $\{Bi_6\}$-based clusters. *Nat. Chem.* **2023**, *15*, 347−356.
(208) *Computational Methods in Lanthanide and Actinide Chemistry*; Dolg, M., Ed.; John Wiley & Sons: Chichester, England, 2015.
(209) Rabuck, A. D.; Scuseria, G. E. Improving self-consistent field convergence by varying occupation numbers. *J. Chem. Phys.* **1999**, *110*, 695−700.
(210) Nava, P.; Sierka, M.; Ahlrichs, R. Density functional study of palladium clusters. *Phys. Chem. Chem. Phys.* **2003**, *5*, 3372−3381.
(211) Saunders, V.; Hillier, I. A "Level−Shifting" method for converging closed shell Hartree−Fock wave functions. *Int. J. Quantum Chem.* **1973**, *7*, 699−705.
(212) Pulay, P. Convergence acceleration of iterative sequences. The case of SCF iteration. *Chem. Phys. Lett.* **1980**, *73*, 393−398.
(213) Chung, A. B.; Rappoport, D.; Ziller, J. W.; Cramer, R. E.; Furche, F.; Evans, W. J. Solid-State End-On to Side-On Isomerization of $(N = N)^{2-}$ in $\{[(R_2N)_3Nd]_2N_2\}^{2-}$ $(R = SiMe_3)$ Connects In Situ $Ln^{III}(NR_2)_3/K$ and Isolated $[Ln^{II}(NR_2)_3]^{1-}$ Dinitrogen Reduction. *J. Am. Chem. Soc.* **2022**, *144*, 17064−17074.
(214) MacDonald, M. R.; Bates, J. E.; Fieser, M. E.; Ziller, J. W.; Furche, F.; Evans, W. J. Expanding rare-earth oxidation state chemistry to molecular complexes of holmium (II) and erbium (II). *J. Am. Chem. Soc.* **2012**, *134*, 8420−8423.
(215) MacDonald, M. R.; Bates, J. E.; Ziller, J. W.; Furche, F.; Evans, W. J. Completing the series of + 2 ions for the lanthanide elements: synthesis of molecular complexes of Pr^{2+}, Gd^{2+}, Tb^{2+}, and Lu^{2+}. *J. Am. Chem. Soc.* **2013**, *135*, 9857−9868.
(216) Fieser, M. E.; MacDonald, M. R.; Krull, B. T.; Bates, J. E.; Ziller, J. W.; Furche, F.; Evans, W. J. Structural, spectroscopic, and theoretical comparison of traditional vs recently discovered Ln^{2+} ions in the $[K(2.2.2\text{-cryptand})][(C_5H_4SiMe_3)_3Ln]$ complexes: the variable nature of Dy^{2+} and Nd^{2+}. *J. Am. Chem. Soc.* **2015**, *137*, 369−382.
(217) Woen, D. H.; Evans, W. J. Expanding the + 2 Oxidation State of the Rare-Earth Metals, Uranium, and Thorium in Molecular Complexes In *Handbook on the Physics and Chemistry of Rare Earths*, Vol. *50*; Bünzli, J.-C. G., Pecharsky, V. K., Eds.; Elsevier: Amsterdam, The Netherlands, 2016; pp 337−394.
(218) Ryan, A. J.; Darago, L. E.; Balasubramani, S. G.; Chen, G. P.; Ziller, J. W.; Furche, F.; Long, J. R.; Evans, W. J. Synthesis, structure, and magnetism of tris(amide)$[Ln\{N(SiMe_3)_2\}_3]^{1-}$ complexes of the non-traditional + 2 lanthanide ions. *Chem.: Eur. J.* **2018**, *24*, 7702−7709.
(219) Moore, W. N.; White, J. R.; Wedal, J. C.; Furche, F.; Evans, W. J. Reduction of Rare-Earth Metal Complexes Induced by γ Irradiation. *Inorg. Chem.* **2022**, *61*, 17713−17718.
(220) Gould, C. A.; McClain, K. R.; Yu, J. M.; Groshens, T. J.; Furche, F.; Harvey, B. G.; Long, J. R. Synthesis and Magnetism of Neutral, Linear Metallocene Complexes of Terbium(II) and Dysprosium(II). *J. Am. Chem. Soc.* **2019**, *141*, 12967−12973.
(221) Rappoport, D. Property-optimized Gaussian basis sets for lanthanides. *J. Chem. Phys.* **2021**, *155*, 124102.
(222) Darago, L. E.; Boshart, M. D.; Nguyen, B. D.; Perlt, E.; Ziller, J. W.; Lukens, W. W.; Furche, F.; Evans, W. J.; Long, J. R. Strong Ferromagnetic Exchange Coupling and Single-Molecule Magnetism in MoS_4^{3-}−Bridged Dilanthanide Complexes. *J. Am. Chem. Soc.* **2021**, *143*, 8465−8475.
(223) Fieser, M. E.; Bates, J. E.; Ziller, J. W.; Furche, F.; Evans, W. J. Dinitrogen reduction via photochemical activation of heteroleptic tris (cyclopentadienyl) rare-earth complexes. *J. Am. Chem. Soc.* **2013**, *135*, 3804−3807.
(224) Fieser, M. E.; Johnson, C. W.; Bates, J. E.; Ziller, J. W.; Furche, F.; Evans, W. J. Dinitrogen reduction, sulfur reduction, and isoprene polymerization via photochemical activation of trivalent bis (cyclopentadienyl) rare-earth-metal allyl complexes. *Organometallics* **2015**, *34*, 4387−4393.
(225) Yu, J. M.; Furche, F. Theoretical Study of Divalent Bis(Pentaisopropylcyclopentadienyl) Actinocenes. *Inorg. Chem.* **2019**, *58*, 16004−16010.
(226) Tao, J.; Perdew, J. P.; Staroverov, V. N.; Scuseria, G. E. Climbing the Density Functional Ladder: Nonempirical Meta−

https://doi.org/10.1021/acs.jctc.3c00347
J. Chem. Theory Comput. 2023, 19, 6859−6890

Generalized Gradient Approximation Designed for Molecules and Solids. *Phys. Rev. Lett.* **2003**, *91*, 146401.
(227) Dolg, M.; Cao, X. Accurate Relativistic Small-Core Pseudopotentials for Actinides. Energy Adjustment for Uranium and First Applications to Uranium Hydride. *J. Phys. Chem. A* **2009**, *113*, 12573−12581.
(228) Cao, X.; Dolg, M.; Stoll, H. Valence basis sets for relativistic energy-consistent small-core actinide pseudopotentials. *J. Chem. Phys.* **2003**, *118*, 487−496.
(229) Cao, X.; Dolg, M. Segmented contraction scheme for small-core actinide pseudopotential basis sets. *J. Mol. Struc. (THEOCHEM)* **2004**, *673*, 203−209.
(230) Guo, F.-S.; Tsoureas, N.; Huang, G.-Z.; Tong, M.-L.; Mansikkamäki, A.; Layfield, R. A. Isolation of a Perfectly Linear Uranium(II) Metallocene. *Angew. Chem., Int. Ed.* **2020**, *59*, 2299−2303.
(231) Holzer, C.; Klopper, W. Communication: A hybrid Bethe-Salpeter/time-dependent density-functional-theory approach for excitation energies. *J. Chem. Phys.* **2018**, *149*, 101101.
(232) Fedotov, D. A.; Coriani, S.; Hättig, C. Damped (linear) response theory within the resolution-of-identity coupled cluster singles and approximate doubles (RI-CC2) method. *J. Chem. Phys.* **2021**, *154*, 124110.
(233) Kristensen, K.; Kauczor, J.; Kjaergaard, T.; Jørgensen, P. Quasienergy formulation of damped response theory. *J. Chem. Phys.* **2009**, *131*, 044112.
(234) Helgaker, T.; Coriani, S.; Jørgensen, P.; Kristensen, K.; Olsen, J.; Ruud, K. Recent Advances in Wave Function-Based Methods of Molecular Property Calculations. *Chem. Rev.* **2012**, *112*, 543−631.
(235) Norman, P. A perspective on nonresonant and resonant electronic response theory for time-dependent molecular properties. *Phys. Chem. Chem. Phys.* **2011**, *13*, 20519−20535.
(236) Kauczor, J.; Norman, P. Efficient Calculations of Molecular Linear Response Properties for Spectral Regions. *J. Chem. Theory Comput.* **2014**, *10*, 2449−2455.
(237) Faber, R.; Coriani, S. Resonant Inelastic X-ray Scattering and Nonesonant X-ray Emission Spectra from Coupled-Cluster (Damped) Response Theory. *J. Chem. Theory Comput.* **2019**, *15*, 520−528.
(238) Hättig, C.; Heß, B. A. Correlated Frequency-dependent Polarizabilities and Dispersion Coefficients in the Time-dependent Second-order Møller-Plesset Approximation. *Chem. Phys. Lett.* **1995**, *233*, 359−370.
(239) Hättig, C.; Heß, B. A. TDMP2 calculation of dynamic multipole polarizabilities and dispersion coefficients for the halogen anions F^-, Cl^-, Br^- and I^-. *J. Chem. Phys.* **1998**, *108*, 3863−3870.
(240) Kauczor, J.; Norman, P.; Saidi, W. A. Non-additivity of polarizabilities and van der Waals C_6 coefficients of fullerenes. *J. Chem. Phys.* **2013**, *138*, 114107.
(241) Norman, P.; Bishop, D. M.; Jensen, H. J. A.; Oddershede, J. Near-resonant absorption in the time-dependent self-consistent field and multiconfigurational self-consistent field approximations. *J. Chem. Phys.* **2001**, *115*, 10323−10334.
(242) Norman, P.; Bishop, D. M.; Jensen, H. J. A.; Oddershede, J. Nonlinear response theory with relaxation: The first-order hyperpolarizability. *J. Chem. Phys.* **2005**, *123*, 194103.
(243) Jensen, L.; Autschbach, J.; Schatz, G. C. Finite lifetime effects on the polarizability within time-dependent density-functional theory. *J. Chem. Phys.* **2005**, *122*, 224115.
(244) Ekström, U.; Norman, P.; Carravetta, V.; Ågren, H. Polarization Propagator for X-Ray Spectra. *Phys. Rev. Lett.* **2006**, *97*, 143001.
(245) Ekström, U.; Norman, P. X-ray absorption spectra from the resonant-convergent first-order polarization propagator approach. *Phys. Rev. A* **2006**, *74*, 042722.
(246) Fahleson, T.; Ågren, H.; Norman, P. A Polarization Propagator for Nonlinear X-ray Spectroscopies. *J. Phys. Chem. Lett.* **2016**, *7*, 1991−1995.
(247) Cukras, J.; Kauczor, J.; Norman, P.; Rizzo, A.; Rikken, G. L. J. A.; Coriani, S. A complex-polarization-propagator protocol for magneto-chiral axial dichroism and birefringence dispersion. *Phys. Chem. Chem. Phys.* **2016**, *18*, 13267−13279.
(248) Coriani, S.; Fransson, T.; Christiansen, O.; Norman, P. Asymmetric-Lanczos-Chain-Driven Implementation of Electronic Resonance Convergent Coupled-Cluster Linear Response Theory. *J. Chem. Theory Comput.* **2012**, *8*, 1616−1628.
(249) Coriani, S.; Christiansen, O.; Fransson, T.; Norman, P. Coupled-cluster response theory for near-edge x-ray-absorption fine structure of atoms and molecules. *Phys. Rev. A* **2012**, *85*, 022507.
(250) Rehn, D. R.; Dreuw, A.; Norman, P. Resonant Inelastic X-ray Scattering Amplitudes and Cross Sections in the Algebraic Diagrammatic Construction/Intermediate State Representation (ADC/ISR) Approach. *J. Chem. Theory Comput.* **2017**, *13*, 5552−5559.
(251) Nørby, M.; Coriani, S.; Kongsted, J. Modeling magnetic circular dichroism within the polarizable embedding approach. *Theor. Chem. Acta.* **2018**, *137*, 49.
(252) Vaara, J.; Rizzo, A.; Kauczor, J.; Norman, P.; Coriani, S. Nuclear spin circular dichroism. *J. Chem. Phys.* **2014**, *140*, 134103.
(253) Andersen, J. H.; Coriani, S.; Hättig, C. Damped quadratic response within the resolution-of-identity coupled cluster singles and approximate doubles (RI-CC2) method. *ChemRxiv* **2023**, DOI: 10.26434/chemrxiv-2023-dgbdz.
(254) Zerulla, B.; Krstić, M.; Beutel, D.; Holzer, C.; Wöll, C.; Rockstuhl, C.; Fernandez-Corbaton, I. A Multi-Scale Approach for Modeling the Optical Response of Molecular Materials Inside Cavities. *Adv. Mater.* **2022**, *34*, 2200350.
(255) Feuerstein, W.; Holzer, C.; Gui, X.; Neumeier, L.; Klopper, W.; Breher, F. Synthesis of New Donor-Substituted Biphenyls: Pre-ligands for Highly Luminescent (ĈĈD) Gold(III) Pincer Complexes. *Eur. J. Chem.* **2020**, *26*, 17156−17164.
(256) Parker, S. M.; Roy, S.; Furche, F. Unphysical divergences in response theory. *J. Chem. Phys.* **2016**, *145*, 134105.
(257) Müller, M. M.; Perdana, N.; Rockstuhl, C.; Holzer, C. Modeling and measuring plasmonic excitations in hollow spherical gold nanoparticles. *J. Chem. Phys.* **2022**, *156*, 094103.
(258) Perdana, N.; Holzer, C.; Rockstuhl, C. Multiscale Modeling of Broadband Perfect Absorbers Based on Gold Metallic Molecules. *ACS Omega* **2022**, *7*, 19337−19346.
(259) Beutel, D.; Groner, A.; Rockstuhl, C.; Fernandez-Corbaton, I. Efficient simulation of biperiodic, layered structures based on the T-matrix method. *J. Opt. Soc. Am. B* **2021**, *38*, 1782−1791.
(260) Zerulla, B.; Li, C.; Beutel, D.; Oßwald, S.; Holzer, C.; Bürck, J.; Bräse, S.; Wöll, C.; Fernandez-Corbaton, I.; Heinke, L.; Rockstuhl, C.; Krstić, M. Exploring Functional Photonic Devices made from a Chiral MetalOrganic Framework Material by a Multiscale Computational Method. *Adv. Funct. Mater.* **2023**, 2301093.
(261) Zerulla, B.; Venkitakrishnan, R.; Beutel, D.; Krstić, M.; Holzer, C.; Rockstuhl, C.; Fernandez-Corbaton, I. A T-Matrix Based Approach to Homogenize Artificial Materials. *Adv. Opt. Mater.* **2023**, *11*, 2201564.
(262) Kauczor, J.; Norman, P.; Christiansen, O.; Coriani, S. Communication: A reduced-space algorithm for the solution of the complex linear response equations used in coupled cluster damped response theory. *J. Chem. Phys.* **2013**, *139*, 211102.
(263) Mori, T.; Inoue, Y.; Grimme, S. Quantum Chemical Study on the Circular Dichroism Spectra and Specific Rotation of Donor-Acceptor Cyclophanes. *J. Phys. Chem. A* **2007**, *111*, 7995−8006.
(264) Li, Z.; Liu, W. First-order nonadiabatic coupling matrix elements between excited states: A Lagrangian formulation at the CIS, RPA, TD-HF, and TD-DFT levels. *J. Chem. Phys.* **2014**, *141*, 014110.
(265) Parker, S. M.; Roy, S.; Furche, F. Multistate hybrid time-dependent density functional theory with surface hopping accurately captures ultrafast thymine photodeactivation. *Phys. Chem. Chem. Phys.* **2019**, *21*, 18999−19010.
(266) Roy, S.; Furche, F.Quinonile Photobasicity is Mediated by Hole Injection. In *Bulletin of the American Physical Society, APS March*

Meeting 2018, Vol. *63*, Los Angeles, CA, March 5−9, 2018; American Physical Society, 2018; Paper V03.00007
(267) Kasha, M. Characterization of electronic transitions in complex molecules. *Discuss. Faraday Soc.* **1950**, *9*, 14−19.
(268) Itoh, T. Fluorescence and Phosphorescence from Higher Excited States of Organic Molecules. *Chem. Rev.* **2012**, *112*, 4541−4568.
(269) Perdew, J. P.; Ernzerhof, M.; Burke, K. Rationale for mixing exact exchange with density functional approximations. *J. Chem. Phys.* **1996**, *105*, 9982−9985.
(270) Weigend, F.; Ahlrichs, R. Balanced basis sets of split valence, triple zeta valence and quadruple zeta valence quality for H to Rn: Design and assessment of accuracy. *Phys. Chem. Chem. Phys.* **2005**, *7*, 3297−3305.
(271) Viswanath, G.; Kasha, M. Confirmation of the anomalous fluorescence of azulene. *J. Chem. Phys.* **1956**, *24*, 574−577.
(272) Geldof, P.; Rettschnick, R.; Hoytink, G. Fluorescence from the second excited singlets of pyrene and 3,4-benzpyrene. *Chem. Phys. Lett.* **1969**, *4*, 59−61.
(273) Baba, H.; Nakajima, A.; Aoi, M.; Chihara, K. Fluorescence from the second excited singlet state and radiationless processes in pyrene vapor. *J. Chem. Phys.* **1971**, *55*, 2433−2438.
(274) Chihara, K.; Baba, H. Effects of foreign gases on dual fluorescences of pyrene vapor. *Bull. Chem. Soc. Jpn.* **1975**, *48*, 3093−3100.
(275) Braun, G.; Borges, I., Jr; Aquino, A. J.; Lischka, H.; Plasser, F.; Do Monte, S. A.; Ventura, E.; Mukherjee, S.; Barbatti, M. Non-Kasha fluorescence of pyrene emerges from a dynamic equilibrium between excited states. *J. Chem. Phys.* **2022**, *157*, 154305.
(276) Borrego-Varillas, R.; Ganzer, L.; Cerullo, G.; Manzoni, C. Ultraviolet transient absorption spectrometer with Sub-20-fs time resolution. *Appl. Sci.* **2018**, *8*, 989.
(277) Foggi, P.; Neuwahl, F. V.; Moroni, L.; Salvi, P. R. Absorption of Azulene: Femtosecond Transient Spectra and Excited State Calculations. *J. Phys. Chem. A* **2003**, *107*, 1689−1696.
(278) Neuwahl, F. V.; Foggi, P. Direct observation of s2-s1 internal conversion in pyrene by femtosecond transient absorption. *Laser Chem.* **1999**, *19*, 375−379.
(279) Hollas, J. M. Determination of molecular conformation from large amplitude vibrations in electronic spectra of organic molecules in a supersonic jet. *Chem. Soc. Rev.* **1993**, *22*, 371−382.
(280) Villa, E.; Amirav, A.; Lim, E. C. Single-vibronic-level and excitation-energy dependence of radiative and nonradiative transitions in jet-cooled S1 pyridine. *J. Phys. Chem.* **1988**, *92*, 5393−5397.
(281) Diau, E. W.-G.; De Feyter, S.; Zewail, A. H. Direct observation of the femtosecond nonradiative dynamics of azulene in a molecular beam: The anomalous behavior in the isolated molecule. *J. Chem. Phys.* **1999**, *110*, 9785.
(282) Cisneros, C.; Thompson, T.; Baluyot, N.; Smith, A. C.; Tapavicza, E. The role of tachysterol in vitamin D photosynthesis - a non-adiabatic molecular dynamics study. *Phys. Chem. Chem. Phys.* **2017**, *19*, 5763−5777.
(283) Tapavicza, E.; Thompson, T.; Redd, K.; Kim, D. Tuning the photoreactivity of Z-hexatriene photoswitches by substituents - a non-adiabatic molecular dynamics study. *Phys. Chem. Chem. Phys.* **2018**, *20*, 24807−24820.
(284) Thompson, T.; Tapavicza, E. First-Principles Prediction of Wavelength-Dependent Product Quantum Yields. *J. Phys. Chem. Lett.* **2018**, *9*, 4758−4764.
(285) Grathwol, C. W.; Wössner, N.; Swyter, S.; Smith, A. C.; Tapavicza, E.; Hofstetter, R. K.; Bodtke, A.; Jung, M.; Link, A. Azologization and repurposing of a hetero-stilbene-based kinase inhibitor: towards the design of photoswitchable sirtuin inhibitors. *Beilstein J. Org. Chem.* **2019**, *15*, 2170−2183.
(286) Sofferman, D. L.; Konar, A.; Mastron, J. N.; Spears, K. G.; Cisneros, C.; Smith, A. C.; Tapavicza, E.; Sension, R. J. Probing the Formation and Conformational Relaxation of Previtamin D_3 and Analogues in Solution and in Lipid Bilayers. *J. Phys. Chem. B* **2021**, *125*, 10085−10096.
(287) Tapavicza, E. Conformationally controlled photochemistry studied by trajectory surface hopping In *Time-Dependent Density Functional Theory*; Zhu, C., Ed.; Jenny Stanford Publishing: Singapore, China, 2022; pp 141−197.
(288) Tapavicza, E.; Furche, F.; Sundholm, D. Importance of vibronic effects in the UV-Vis spectrum of the 7, 7, 8, 8-tetracyanoquinodimethane anion. *J. Chem. Theory Comput.* **2016**, *12*, 5058−5066.
(289) Santoro, F.; Improta, R.; Lami, A.; Bloino, J.; Barone, V. Effective method to compute Franck-Condon integrals for optical spectra of large molecules in solution. *J. Chem. Phys.* **2007**, *126*, 084509.
(290) Heller, E. J. The semiclassical way to molecular spectroscopy. *Acc. Chem. Res.* **1981**, *14*, 368−375.
(291) Heller, E. J. *The semiclassical way to dynamics and spectroscopy*; Princeton University Press: Princeton, NJ, 2018.
(292) Baiardi, A.; Bloino, J.; Barone, V. General time dependent approach to vibronic spectroscopy including Franck-Condon, Herzberg−Teller, and Duschinsky effects. *J. Chem. Theory Comput.* **2013**, *9*, 4097−4115.
(293) Tapavicza, E. Generating Function Approach to Single Vibronic Level Fluorescence Spectra. *J. Phys. Chem. Lett.* **2019**, *10*, 6003−6009.
(294) Begušić, T.; Tapavicza, E.; Vaníček, J. Applicability of the Thawed Gaussian Wavepacket Dynamics to the Calculation of Vibronic Spectra of Molecules with Double-Well Potential Energy Surfaces. *J. Chem. Theory Comput.* **2022**, *18*, 3065−3074.
(295) Duschinsky, F. The importance of the electron spectrum in multi atomic molecules. Concerning the Franck-Condon principle. *Acta Physicochim. URSS* **1937**, *7*, 551−566.
(296) Benkyi, I.; Tapavicza, E.; Fliegl, H.; Sundholm, D. Calculation of vibrationally resolved absorption spectra of acenes and pyrene. *Phys. Chem. Chem. Phys.* **2019**, *21*, 21094−21103.
(297) De Queiroz, T. B.; De Figueroa, E. R.; Coutinho-Neto, M. D.; Maciel, C. D.; Tapavicza, E.; Hashemi, Z.; Leppert, L. First principles theoretical spectroscopy of methylene blue: Between limitations of time-dependent density functional theory approximations and its realistic description in the solvent. *J. Chem. Phys.* **2021**, *154*, 044106.
(298) von Cosel, J.; Cerezo, J.; Kern-Michler, D.; Neumann, C.; van Wilderen, L. J.; Bredenbeck, J.; Santoro, F.; Burghardt, I. Vibrationally resolved electronic spectra including vibrational pre-excitation: Theory and application to VIPER spectroscopy. *J. Chem. Phys.* **2017**, *147*, 164116.
(299) Heller, E. J. Time-dependent approach to semiclassical dynamics. *J. Chem. Phys.* **1975**, *62*, 1544−1555.
(300) Wehrle, M.; Šulc, M.; Vaníček, J. On-the-fly Ab Initio Semiclassical Dynamics: Identifying Degrees of Freedom Essential for Emission Spectra of Oligothiophenes. *J. Chem. Phys.* **2014**, *140*, 244114.
(301) Wehrle, M.; Oberli, S.; Vaníček, J. On-the-fly ab initio semiclassical dynamics of floppy molecules: Absorption and photoelectron spectra of ammonia. *J. Phys. Chem. A* **2015**, *119*, 5685.
(302) Begušić, T.; Patoz, A.; Šulc, M.; Vaníček, J. On-the-fly ab initio three thawed Gaussians approximation: a semiclassical approach to Herzberg-Teller spectra. *Chem. Phys.* **2018**, *515*, 152−163.
(303) Vaníček, J.; Begušić, T. Ab Initio Semiclassical Evaluation of Vibrationally Resolved Electronic Spectra With Thawed Gaussians. In *Molecular Spectroscopy and Quantum Dynamics*; Marquardt, R., Quack, M., Eds.; Elsevier: St. Louis, MO, 2021; pp 199−229.
(304) Begušić, T.; Cordova, M.; Vaníček, J. Single-Hessian thawed Gaussian approximation. *J. Chem. Phys.* **2019**, *150*, 154117.
(305) Prlj, A.; Begušić, T.; Zhang, Z. T.; Fish, G. C.; Wehrle, M.; Zimmermann, T.; Choi, S.; Roulet, J.; Moser, J.-E.; Vaníček, J. Semiclassical Approach to Photophysics Beyond Kasha's Rule and Vibronic Spectroscopy Beyond the Condon Approximation. The Case of Azulene. *J. Chem. Theory Comput.* **2020**, *16*, 2617−2626.
(306) Begušić, T.; Vaníček, J. Efficient semiclassical dynamics for vibronic spectroscopy beyond harmonic, Condon, and zero-temperature approximations. *Chimia* **2021**, *75*, 261.

https://doi.org/10.1021/acs.jctc.3c00347
J. Chem. Theory Comput. 2023, 19, 6859−6890

(307) Vidberg, H. J.; Serene, J. W. Solving the Eliashberg equations by means of N-point Padé approximants. *J. Low Temp. Phys.* **1977**, *29*, 179−192.
(308) Rojas, H. N.; Godby, R. W.; Needs, R. J. Space-Time Method for Ab Initio Calculations of Self-Energies and Dielectric Response Functions of Solids. *Phys. Rev. Lett.* **1995**, *74*, 1827−1830.
(309) Voora, V. K. Molecular Electron Affinities Using the Generalized Kohn-Sham Semicanonical Projected Random Phase Approximation. *J. Phys. Chem. Lett.* **2021**, *12*, 433−439.
(310) Samal, B.; Voora, V. K. Modeling Nonresonant X-ray Emission of Second- and Third-Period Elements without Core-Hole Reference States and Empirical Parameters. *J. Chem. Theory Comput.* **2022**, *18*, 7272−7285.
(311) Sugiura, C. Kβ X-Ray Emission and K X-Ray Absorption Spectra of Sulfur in Sulfate Compounds. *Jpn. J. Appl. Phys.* **1993**, *32*, 3509−3514.
(312) Qureshi, M.; Nowak, S. H.; Vogt, L. I.; Cotelesage, J. J. H.; Dolgova, N. V.; Sharifi, S.; Kroll, T.; Nordlund, D.; Alonso-Mori, R.; Weng, T.-C.; Pickering, I. J.; George, G. N.; Sokaras, D. Sulfur Kβ X-ray emission spectroscopy: comparison with sulfur K-edge X-ray absorption spectroscopy for speciation of organosulfur compounds. *Phys. Chem. Chem. Phys.* **2021**, *23*, 4500−4508.
(313) Perdew, J. P.; Burke, K.; Ernzerhof, M. Generalized Gradient Approximation Made Simple. *Phys. Rev. Lett.* **1996**, *77*, 3865−3868.
(314) Grimme, S.; Antony, J.; Ehrlich, S.; Krieg, H. A consistent and accurate ab initio parametrization of density functional dispersion correction (DFT-D) for the 94 elements H-Pu. *J. Chem. Phys.* **2010**, *132*, 154104.
(315) Grimme, S.; Ehrlich, S.; Goerigk, L. Effect of the damping function in dispersion corrected density functional theory. *J. Comput. Chem.* **2011**, *32*, 1456−1465.
(316) Dunning, T. H. Gaussian basis sets for use in correlated molecular calculations. I. The atoms boron through neon and hydrogen. *J. Chem. Phys.* **1989**, *90*, 1007−1023.
(317) Yu, J. M.; Nguyen, B. D.; Tsai, J.; Hernandez, D. J.; Furche, F. Selfconsistent random phase approximation methods. *J. Chem. Phys.* **2021**, *155*, 040902.
(318) Perdew, J. P.; Yang, W.; Burke, K.; Yang, Z.; Gross, E. K. U.; Scheffler, M.; Scuseria, G. E.; Henderson, T. M.; Zhang, I. Y.; Ruzsinszky, A.; Peng, H.; Sun, J.; Trushin, E.; Görling, A. Understanding band gaps of solids in generalized Kohn−Sham theory. *Proc. Natl. Acad. Sci. U.S.A.* **2017**, *114*, 2801−2806.
(319) Baerends, E. J.; Gritsenko, O. V.; van Meer, R. The Kohn-Sham gap, the fundamental gap and the optical gap: the physical meaning of occupied and virtual Kohn-Sham orbital energies. *Phys. Chem. Chem. Phys.* **2013**, *15*, 16408−16425.
(320) Kronik, L.; Stein, T.; Refaely-Abramson, S.; Baer, R. Excitation Gaps of Finite-Sized Systems from Optimally Tuned Range-Separated Hybrid Functionals. *J. Chem. Theory Comput.* **2012**, *8*, 1515−1531.
(321) Lüftner, D.; Refaely-Abramson, S.; Pachler, M.; Resel, R.; Ramsey, M. G.; Kronik, L.; Puschnig, P. Experimental and theoretical electronic structure of quinacridone. *Phys. Rev. B* **2014**, *90*, 075204.
(322) Slattery, D. K.; Linkous, C. A.; Gruhn, N. E.; Baum, J. Semiempirical MO and voltammetric estimation of ionization potentials of organic pigments. Comparison to gas phase ultraviolet photoelectron spectroscopy. *Dyes Pgm.* **2001**, *49*, 21−27.
(323) Tew, D. P. Principal Domains in Local Correlation Theory. *J. Chem. Theory Comput.* **2019**, *15*, 6597−6606.
(324) Tew, D. P. Principal domains in F12 explicitly correlated theory. In *New Electron Correlation Methods and their Applications, and Use of Atomic Orbitals with Exponential Asymptotes*; Musial, M., Hoggan, P. E., Eds.; Advances in Quantum Chemistry, Vol. *83*; Academic Press, 2021; pp 83−106.
(325) Sorathia, K.; Tew, D. P. Basis set extrapolation in pair natural orbital theories. *J. Chem. Phys.* **2020**, *153*, 174112.
(326) Li, W.; Saleh, A.; Sharma, M.; Hunecke, C.; Sierka, M.; Neuhaus, M.; Hedewig, L.; Bergues, B.; Alharbi, M.; ALQahtani, H.; Azzeer, A. M.; Gräfe, S.; Kling, M. F.; Alharbi, A. F.; Wang, Z. Resonance effects in Brunel harmonic generation in thin film organic semiconductors. *Adv. Opt. Mater.* **2023**, No. 2203070.
(327) Burow, A. M.; Sierka, M. Linear scaling hierarchical integration scheme for the exchange-correlation term in molecular and periodic systems. *J. Chem. Theory Comput.* **2011**, *7*, 3097−3104.
(328) Irmler, A.; Burow, A. M.; Pauly, F. Robust Periodic Fock Exchange with Atom-Centered Gaussian Basis Sets. *J. Chem. Theory Comput.* **2018**, *14*, 4567−4580.
(329) Blanes, S.; Casas, F.; Oteo, J.; Ros, J. The Magnus expansion and some of its applications. *Phys. Rep* **2009**, *470*, 151−238.
(330) Cheng, C.-L.; Evans, J. S.; Van Voorhis, T. Simulating molecular conductance using real-time density functional theory. *Phys. Rev. B* **2006**, *74*, 155112.
(331) Treutler, O. *Entwicklung und Anwendung von Dichtefunktionalmethoden*. Ph.D. Dissertation, University of Karlsruhe (TH), Karlsruhe, Germany, 1995.
(332) Lembarki, A.; Chermette, H. Obtaining a gradient-corrected kinetic-energy functional from the Perdew-Wang exchange functional. *Phys. Rev. A* **1994**, *50*, 5328−5331.
(333) Treß, R. S.; Liu, J.; Hättig, C.; Höfener, S. Pushing the limits: efficient wavefunction methods for excited states in complex systems using frozen-density embedding. *J. Chem. Phys.* **2022**, *157*, 204101.
(334) Wesolowski, T. A.; Warshel, A. Frozen density functional approach for ab initio calculations of solvated molecules. *J. Chem. Phys.* **1993**, *97*, 8050−8053.
(335) Lee, S. J. R.; Welborn, M.; Manby, F. R.; Miller, T. F. I. Projection-Based Wavefunction-in-DFT Embedding. *Acc. Chem. Res.* **2019**, *52*, 1359−1368.
(336) Manby, F. R.; Stella, M.; Goodpaster, J. D.; Miller, T. F. I. A Simple, Exact Density-Functional-Theory Embedding Scheme. *J. Chem. Theory Comput.* **2012**, *8*, 2564−2568.
(337) Sharma, M.; Mishra, D. *CrysX*: crystallographic tools for the Android platform. *J. Appl. Crystallogr.* **2019**, *52*, 1449−1454.
(338) Tymczak, C. J.; Weber, V. T.; Schwegler, E.; Challacombe, M. Linear scaling computation of the Fock matrix. VIII. Periodic boundaries for exact exchange at the Γ point. *J. Chem. Phys.* **2005**, *122*, 124105.
(339) Guidon, M.; Hutter, J.; VandeVondele, J. Robust Periodic Hartree−Fock Exchange for Large-Scale Simulations Using Gaussian Basis Sets. *J. Chem. Theory Comput.* **2009**, *5*, 3010−3021.
(340) Paier, J.; Diaconu, C. V.; Scuseria, G. E.; Guidon, M.; VandeVondele, J.; Hutter, J. Accurate Hartree-Fock energy of extended systems using large Gaussian basis sets. *Phys. Rev. B* **2009**, *80*, 174114.
(341) Paier, J.; Marsman, M.; Hummer, K.; Kresse, G.; Gerber, I. C.; Ángyán, J. G. Screened hybrid density functionals applied to solids. *J. Chem. Phys.* **2006**, *124*, 154709.
(342) Peintinger, M. F.; Oliveira, D. V.; Bredow, T. Consistent Gaussian basis sets of triple-zeta valence with polarization quality for solid-state calculations. *J. Comput. Chem.* **2013**, *34*, 451−459.
(343) Schäfer, A.; Horn, H.; Ahlrichs, R. Fully optimized contracted Gaussian basis sets for atoms Li to Kr. *J. Chem. Phys.* **1992**, *97*, 2571−2577.
(344) Adamo, C.; Barone, V. Toward reliable density functional methods without adjustable parameters: The PBE0 model. *J. Chem. Phys.* **1999**, *110*, 6158−6170.
(345) Krukau, A. V.; Vydrov, O. A.; Izmaylov, A. F.; Scuseria, G. E. Influence of the exchange screening parameter on the performance of screened hybrid functionals. *J. Chem. Phys.* **2006**, *125*, 224106.
(346) Warburton, R. E.; Soudackov, A. V.; Hammes-Schiffer, S. Theoretical Modeling of Electrochemical Proton-Coupled Electron Transfer. *Chem. Rev.* **2022**, *122*, 10599−10650.
(347) Hammes-Schiffer, S. Nuclear−electronic orbital methods: Foundations and prospects. *J. Chem. Phys.* **2021**, *155*, 030901.
(348) Webb, S. P.; Iordanov, T.; Hammes-Schiffer, S. Multiconfigurational nuclear-electronic orbital approach: Incorporation of nuclear quantum effects in electronic structure calculations. *J. Chem. Phys.* **2002**, *117*, 4106−4118.

https://doi.org/10.1021/acs.jctc.3c00347
J. Chem. Theory Comput. 2023, 19, 6859−6890

(349) Zundel, G. Hydration Structure and Intermolecular Interaction in Polyelectrolytes. *Angew. Chem., Int. Ed. Engl.* **1969**, *8*, 499−509.
(350) Sirjoosingh, A.; Pak, M. V.; Hammes-Schiffer, S. Multi-component density functional theory study of the interplay between electron-electron and electron-proton correlation. *J. Chem. Phys.* **2012**, *136*, 174114.
(351) Xu, J.; Zhou, R.; Tao, Z.; Malbon, C.; Blum, V.; Hammes-Schiffer, S.; Kanai, Y. Nuclear−electronic orbital approach to quantization of protons in periodic electronic structure calculations. *J. Chem. Phys.* **2022**, *156*, 224111.
(352) Cremer, D. Møller−Plesset perturbation theory: from small molecule methods to methods for thousands of atoms. *WIREs Comput. Mol. Sci.* **2011**, *1*, 509−530.
(353) Grimme, S. Semiempirical hybrid density functional with perturbative second-order correlation. *J. Chem. Phys.* **2006**, *124*, 034108.
(354) Goerigk, L.; Grimme, S. Double-hybrid density functionals. *WIREs Comput. Mol. Sci.* **2014**, *4*, 576−600.
(355) Nguyen, B. D.; Chen, G. P.; Agee, M. M.; Burow, A. M.; Tang, M. P.; Furche, F. Divergence of Many-Body Perturbation Theory for Noncovalent Interactions of Large Molecules. *J. Chem. Theory Comput.* **2020**, *16*, 2258−2273.
(356) Shee, J.; Loipersberger, M.; Rettig, A.; Lee, J.; Head-Gordon, M. Regularized Second-Order Møller-Plesset Theory: A More Accurate Alternative to Conventional MP2 for Noncovalent Interactions and Transition Metal Thermochemistry for the Same Computational Cost. *J. Phys. Chem. Lett.* **2021**, *12*, 12084−12097.
(357) Cohen, A. J.; Mori-Sánchez, P.; Yang, W. Second-Order Perturbation Theory with Fractional Charges and Fractional Spins. *J. Chem. Theory Comput.* **2009**, *5*, 786−792.
(358) Grimme, S. Improved second-order Møller−Plesset perturbation theory by separate scaling of parallel- and antiparallel-spin pair correlation energies. *J. Chem. Phys.* **2003**, *118*, 9095−9102.
(359) Seidl, M.; Giarrusso, S.; Vuckovic, S.; Fabiano, E.; Gori-Giorgi, P. Communication: Strong-interaction limit of an adiabatic connection in Hartree-Fock theory. *J. Chem. Phys.* **2018**, *149*, 241101.
(360) Seidl, M.; Perdew, J. P.; Kurth, S. Density functionals for the strong-interaction limit. *Phys. Rev. A* **2000**, *62*, 012502.
(361) Daas, T. J.; Kooi, D. P.; Grooteman, A. J. A. F.; Seidl, M.; Gori-Giorgi, P. Gradient Expansions for the Large-Coupling Strength Limit of the Møller-Plesset Adiabatic Connection. *J. Chem. Theory Comput.* **2022**, *18*, 1584−1594.
(362) Seidl, M.; Perdew, J. P.; Kurth, S. Simulation of All-Order Density-Functional Perturbation Theory, Using the Second Order and the Strong-Correlation Limit. *Phys. Rev. Lett.* **2000**, *84*, 5070−5073.
(363) Daas, T. J.; Fabiano, E.; Della Sala, F.; Gori-Giorgi, P.; Vuckovic, S. Noncovalent Interactions from Models for the Møller−Plesset Adiabatic Connection. *J. Phys. Chem. Lett.* **2021**, *12*, 4867−4875.
(364) Fabiano, E.; Gori-Giorgi, P.; Seidl, M.; Della Sala, F. Interaction-Strength Interpolation Method for Main-Group Chemistry: Benchmarking, Limitations, and Perspectives. *J. Chem. Theory Comput.* **2016**, *12*, 4885−4896.
(365) Gori-Giorgi, P.; Vignale, G.; Seidl, M. Electronic Zero-Point Oscillations in the Strong-Interaction Limit of Density Functional Theory. *J. Chem. Theory Comput.* **2009**, *5*, 743−753.
(366) Smiga, S.; Della Sala, F.; Gori-Giorgi, P.; Fabiano, E. Self-Consistent Implementation of Kohn-Sham Adiabatic Connection Models with Improved Treatment of the Strong-Interaction Limit. *J. Chem. Theory Comput.* **2022**, *18*, 5936−5947.
(367) Vuckovic, S.; Gori-Giorgi, P.; Della Sala, F.; Fabiano, E. Restoring Size Consistency of Approximate Functionals Constructed from the Adiabatic Connection. *J. Phys. Chem. Lett.* **2018**, *9*, 3137−3142.
(368) Sedlak, R.; Janowski, T.; Pitoňák, M.; Řezáč, J.; Pulay, P.; Hobza, P. Accuracy of Quantum Chemical Methods for Large Noncovalent Complexes. *J. Chem. Theory Comput.* **2013**, *9*, 3364−3374.
(369) Ballesteros, F.; Dunivan, S.; Lao, K. U. Coupled cluster benchmarks of large noncovalent complexes: The L7 dataset as well as DNA-ellipticine and buckycatcher-fullerene. *J. Chem. Phys.* **2021**, *154*, 154104.
(370) Rocca, D.; Gebauer, R.; Saad, Y.; Baroni, S. Turbo charging time-dependent density-functional theory with Lanczos chains. *J. Chem. Phys.* **2008**, *128*, 154105.
(371) Zuehlsdorff, T. J.; Hine, N. D. M.; Spencer, J. S.; Harrison, N. M.; Riley, D. J.; Haynes, P. D. Linear-scaling time-dependent density-functional theory in the linear response formalism. *J. Chem. Phys.* **2013**, *139*, 064104.
(372) Gao, Y.; Neuhauser, D.; Baer, R.; Rabani, E. Sublinear scaling for time-dependent stochastic density functional theory. *J. Chem. Phys.* **2015**, *142*, 034106.
(373) Baseggio, O.; Fronzoni, G.; Stener, M. A new time dependent density functional algorithm for large systems and plasmons in metal clusters. *J. Chem. Phys.* **2015**, *143*, 024106.
(374) Bauernschmitt, R.; Häser, M.; Treutler, O.; Ahlrichs, R. Calculation of excitation energies within time-dependent density functional theory using auxiliary basis set expansions. *Chem. Phys. Lett.* **1997**, *264*, 573−578.
(375) Heinze, H. H.; Görling, A.; Rösch, N. An efficient method for calculating molecular excitation energies by time-dependent density-functional theory. *J. Chem. Phys.* **2000**, *113*, 2088.
(376) Weigend, F. Accurate Coulomb-fitting basis sets for H to Rn. *Phys. Chem. Chem. Phys.* **2006**, *8*, 1057−1065.
(377) Weigend, F.; Kattannek, M.; Ahlrichs, R. Approximated electron repulsion integrals: Cholesky decomposition versus resolution of the identity methods. *J. Chem. Phys.* **2009**, *130*, 164106.
(378) Grimme, S. A Simplified Tamm-Dancoff Density Functional Approach for the Electronic Excitation Spectra of Very Large Molecules. *J. Chem. Phys.* **2013**, *138*, 244104.
(379) Bannwarth, C.; Grimme, S. A simplified time-dependent density functional theory approach for electronic ultraviolet and circular dichroism spectra of very large molecules. *Comput. Theoret. Chem.* **2014**, *1040−1041*, 45.
(380) Rüger, R.; van Lenthe, E.; Heine, T.; Visscher, L. Tight-binding approximations to time-dependent density functional theory A fast approach for the calculation of electronically excited states. *J. Chem. Phys.* **2016**, *144*, 184103.
(381) Jacquemin, D.; Wathelet, V.; Perpète, E. A.; Adamo, C. Extensive TD-DFT Benchmark: Singlet-Excited States of Organic Molecules. *J. Chem. Theory Comput.* **2009**, *5*, 2420−2435.
(382) Liang, J.; Feng, X.; Hait, D.; Head-Gordon, M. Revisiting the Performance of Time-Dependent Density Functional Theory for Electronic Excitations: Assessment of 43 Popular and Recently Developed Functionals from Rungs One to Four. *J. Chem. Theory Comput.* **2022**, *18*, 3460−3473.
(383) Giannone, G.; Della Sala, F. Minimal Auxiliary Basis Set for Time-Dependent Density Functional Theory and Comparison with Tight-Binding Approximations: Application to Silver Nanoparticles. *J. Chem. Phys.* **2020**, *153*, 084110.
(384) Zhou, Z.; Della Sala, F.; Parker, S. M. Minimal auxiliary basis set approach for the electronic excitation spectra of organic molecules. *J. Phys. Chem. Lett.* **2023**, *14*, 1968−1976.
(385) Franzke, Y. J.; Schosser, W. M.; Pauly, F. Self-consistent and efficient treatment of relativistic effects with periodic density functional methods: Energies, Gradients, and Stress Tensors *arXiv (Physics.Chemical Physics)*, May 20, 2023, 2305.03817, ver. 2. DOI: 10.48550/arXiv.2305.03817.
(386) Zhao, R.; Zhang, Y.; Xiao, Y.; Liu, W. Exact two-component relativistic energy band theory and application. *J. Chem. Phys.* **2016**, *144*, 044105.
(387) Ahlrichs, R.; May, K. Contracted all-electron Gaussian basis sets for atoms Rb to Xe. *Phys. Chem. Chem. Phys.* **2000**, *2*, 943−945.

(388) Weigend, F.; Baldes, A. Segmented contracted basis sets for one- and two-component Dirac-Fock effective core potentials. *J. Chem. Phys.* **2010**, *133*, 174102.
(389) Kadek, M.; Repisky, M.; Ruud, K. All-electron fully relativistic Kohn-Sham theory for solids based on the Dirac-Coulomb Hamiltonian and Gaussian-type functions. *Phys. Rev. B* **2019**, *99*, 205103.
(390) Dyall, K. G. Relativistic Quadruple-Zeta Triple-Zeta and Revised and Double-Zeta Basis Sets for the 4p, 5p, and 6p Elements. *Theor. Chem. Acc.* **2006**, *115*, 441−447.
(391) Dyall, K. G. Relativistic double-zeta, triple-zeta, and quadruple-zeta basis sets for the 4d elements Y-Cd. *Theor. Chem. Acc.* **2007**, *117*, 483−489.
(392) Bodo, F.; Desmarais, J. K.; Erba, A. Spin current density functional theory of Weyl semimetals. *Phys. Rev. B* **2022**, *105*, 125108.
(393) Desmarais, J. K.; Flament, J.-P.; Erba, A. Spin-orbit coupling in periodic systems with broken time-reversal symmetry: Formal and computational aspects. *Phys. Rev. B* **2020**, *101*, 235142.
(394) Lyman, I. Code quality: a concern for businesses, bottom lines, and empathetic programmers. *The Overflow*, October 18, 2021. https://stackoverflow.blog/2021/10/18/code-quality-a-concern-for-businesses-bottom-lines-and-empathetic-programmers/ (accessed 2023-03-20).

https://doi.org/10.1021/acs.jctc.3c00347
J. Chem. Theory Comput. 2023, 19, 6859−6890